DOCTORAL THESIS

Solid-State Linear Transformer Driver with Automatic Feedback Control and Its Application to Pulsed Gas Discharge

Author: **YANG Junxiang**

Supervisor: **Prof.JIANG Weihua**

Asst.TAICHI Sugai

NAGAOKA UNIVERSITY OF TECHNOLOGY

Department of < Extreme Energy-Density Research Institute >

Submitted in partial fulfillment of the requirements

for the degree of

Doctor of Engineering, < Energy and Environment Science>

ABSTRACT

Pulsed power technology began a hundred years ago and was initially applied in the field of defense technology due to its characteristics of short duration and high power output. With the development of solid-state switch technology in recent years, compact, high repetition rate, and flexible switches have been used in the field of pulsed power to achieve miniaturization of pulsed power generators, which greatly promotes the application of pulsed power technology in industry. However, when pulsed power is applied in industry, especially in the generation of plasma by pulsed atmospheric pressure gas discharge, scientists have also discovered a series of new scientific problems, such as large-area and uniform discharge, time-varying impedance, and memory effect. However, the pulse parameters of pulsed power have significant importance in studying these problems. Therefore, the main purpose of this article is to develop a new type of flexible and controllable solid-state pulsed power generator to study and solve the problems of pulsed atmospheric pressure gas discharge.

This article can be divided into several parts:

Chapter 1: We introduced the background and development trends of pulsed power technology, as well as its typical industrial applications such as tumor ablation, industrial waste gas and water treatment. Finally, we discussed the new scientific problems arising from the application of pulsed power technology in industry, such as the problem of large-area uniform discharge, time-varying impedance in pulsed atmospheric pressure gas discharge, and the memory effect in pulsed atmospheric pressure gas discharge.

Chapter 2: We developed a compact solid-state linear transformer drivers (SSLTD) power generator based on the principle of large-scale LTD, and analyzed the advantages of SSLTD over

other traditional pulsed power generators. Combined with some flexible control hardware, we achieved flexible output of SSLTD. Based on this, in order to meet industrial needs, we further proposed the future development trends of SSLTD: automatic feedback control-based SSLTD and bipolar SSLTD.

Chapter 3: In response to the time-varying impedance problem of pulsed power in atmospheric pressure gas discharge mentioned in Chapter 1, we used the SSLTD based on automatic feedback control principle developed in Chapter 2 and implemented control of time-varying impedance in pulse atmospheric pressure gas discharge through appropriate preset programs. As a result, during repetitive operation, our SSLTD can figure out the right output waveform according to a user scenario and can respond to any variation that may occur on the load. The impedance was controlled within a relatively constant range in 100 ns.

Chapter 4: In response to the memory effect problem in unipolar pulsed atmospheric pressure gas discharge raised in Chapter 1, we developed a bipolar SSLTD based on the unipolar SSLTD introduced in Chapter 2. Taking advantage of the output flexibility of the bipolar SSLTD, we have studied the residual charges phenomenon by the coaxial discharge load. The experiment result shows that for two consecutive positive pulses discharge, the current of the second positive pulse is usually lower than that of the first pulse for the same voltage amplitude. However, a middle negative pulse applied between the first and second pulse can increase the current of the second positive pulse. An explanation for this phenomenon has been explored using a 1-D model that considers the effect of residual charge left by the previous pulse discharge. According to the explanation of our 1-D discharge model, this phenomenon may be caused by the residual charge distorting the discharge electric field strength. The findings obtained by this paper will help us understand the fundamental characteristics of pulsed atmospheric pressure gas discharge.

Chapter 5: We summarize the main research content of this article.

Chapter 6: We summarized the achievements obtained during my doctoral period.

Key words: Pulsed power, solid-state linear transformer drivers, automatic feedback control, atmospheric pressure gas discharge, time-varying impedance, memory effect.

Table of Contents

List of Figures

List of Tables

CHAPTER I: INTRODUCTION

1.1 A Reviewed of Pulsed Power Technology

1.1.1 History and Present Status

Pulsed power technology is a new science and technology birthed 100 years ago which is significant for the military fields, owing to its unique characteristics of high power and time domains [1]. Initially, pulsed power technology was used to develop nuclear technology. For example, researchers used pulsed power to create flash X-rays to take photos of nuclear weapons and investigate the inner bomb information [2].

A Marx generator is a typical pulsed power circuit first described by Erwin Otto Marx in 1924, which purpose is to generate a high-voltage pulse from a low-voltage DC supply [3]. In 1939, the former Soviet Union successfully developed a Marx generator that simulated lightning shock waves. In the 1960s, J.C. Martin, British Atomic Energy Research Center, combined the Marx with Blumlein line pulsed power generator to compress the pulse width from microseconds to a few tens of nanoseconds which initiated a new era of pulsed power technology. After that, pulsed power technology developed rapidly and became an independent discipline [4][5].

Table 1-1 shows some large pulsed power devices developed in the world. It is not hard to observe that pulsed power technology developed rapidly after the 1960s [6]. However, it is noticeable from Table 1-1 that some countries have shown less interest in developing large pulsed power devices in the 21st century, as indicated by different colored markers. This is likely due to the global theme of peace, where the development of such devices for military and nuclear applications is no longer as important as it once was.

Table 1-1. International high power pulse device.

Time	Device name	Country	Main parameters
1964	Mini B	U.K.(AWE)	2.2 MV, 50 kA (Low impedance)
1968	Hermes-II	USA (SNL)	10-12MV 0.17MA, 80ns (High impedance)
1968	Gambl-I	USA (NRL)	0.75 MV 0.5 MA, 50 ns (Low impedance)
1970	Gambl-II	USA (NRL)	0.9 MV 1.3 MA, 50 ns (Low impedance)
1974	Thalie	France	10-15MV 0.2MA,70ns (High impedance)

1975	Pithon	USA PI	2MV, 3.5MA,50ns (Low impedance)
1977	Liu-10	Former Soviet Union	14MV,50kA,20ns (IVA)
1978	Blackjack5	USA Maxwell	3MV,3.5MA,50ns (Low impedance)
1978	ИГУР	Former Soviet Union	6MV,80kA,20-150ns (IES)
1978	Reiden-IV	Japan, Osaka University	1.4MV,1.4MA,50ns (Low impedance)
1979	Flash-I	People's Republic of China (P.R.C), China Academy of Engineering Physics (CAEP)	8MV,0.1MA,80ns (High impedance)
1979	ТОНУС-II	Former Soviet Union	1MV,1MA,60ns (Low impedance)
1979	ETA	USA LLNL	4.5MV,10kA,50ns (IVA)

1980	PBFA-I	USA SNL	1.9MV,4.5MA,40ns (36 branches parallel)
1981	AGLAE-II	France	0.7MV,1.7MA,35ns (Low impedance)
1983	Liu-10M	Former Soviet Union	25MV,50kA,20ns (IVA)
1983	DECADE	USA PI	1.5MV,17MA,50ns (Multiple devices parallel)
1984	ATA	USA LLNL	50MV,10kA,70ns (IVA)
1985	PBFA-II	USA SNL	4MV,10MA,40ns (72 branches parallel)
1986	ETIGO-II	Japan, Nagaoka University of Technology	3MV,0.46MA,50ns (Low impedance)
1986	SWARF-II	U.K.AWE	10 MV,100 kA (High impedance)

1989	Liu-30	Former Soviet Union	40MV,0.1MA,20ns
1989	Angara-5-1	Former Soviet Union	3MV,3-5MA,90ns (8 branches parallel)
1989	Hermes-III	USA SNL	20MV,0.8MA,40ns (IVA)
1990	Flash-II	P.R.C., (Northwest Institute of nuclear technology)	0.9MV,0.9MA,70ns (Low impedance)
1990	Эмир	Former Soviet Union	7.5MV,0.2MA, 20-200ns (IES)
1993	LIA-10	P.R.C.,CAEP	12MV,3.5kA,70ns (IVA)
1996	ETIGO-III	Japan, Nagaoka Univ.Tech.	8MV,5kA,30ns (IVA)
1996	PBFA-Z/ZR	USA SNL	2.5MV,20-26MA,40ns (36 branches parallel)

2000	ETIGO-IV	Japan, Nagaoka Univ.Tech.	0.5MV, 13kA, 200ns,1HZ (MPC)
2000	AIRIX	France	16-20MV,3.5MA,60ns (IVA)
2003	ShenLong-I	P.R.C.,CAEP	20MV,3.5kA,70ns (IVA)
2013	PTS-I	P.R.C.,CAEP	3MJ,8-10MA (24 branches parallel)
2004	Mercury	USA NRL	6MV, 0.36MA,50ns (IVA)
2015	ShenLong-II	P.R.C.,CAEP	3MV,>2kA,2MHZ (Induction voltage adder and transmission line delay)

In recent years, there has been a rapid development of compact pulsed power generators, which has led to the increased use of pulsed power technology in various industries. In biomedicine, researchers have found that strong nanosecond electric fields can induce biological effects on certain cells, including cancer cells with appropriate parameter pulses [7]. In waste gas treatment, studies conducted at Kumamoto University suggest that nanosecond pulses can be

utilized for flue gas denitrification [8]. In wastewater treatment, researchers at Nagaoka University of Technology have demonstrated that strong oxidizing substances generated by nanosecond pulse discharge can effectively treat industrial wastewater [9].

1.1.2 Principle of Pulsed Power System

The principle of pulsed power is to accumulate energy over a relatively long period and release it quickly, resulting in an increase in instantaneous power [1]. The amount of energy stored and the discharge time determine the output power, with higher energy storage and shorter discharge time resulting in higher output power. Figure 1-1 provides an example of pulse compression, where 1 kW of power is compressed in 1 second, resulting in a total energy of 1 kJ. This energy is then released within 1 microsecond, generating a peak power of 1 GW at the load.

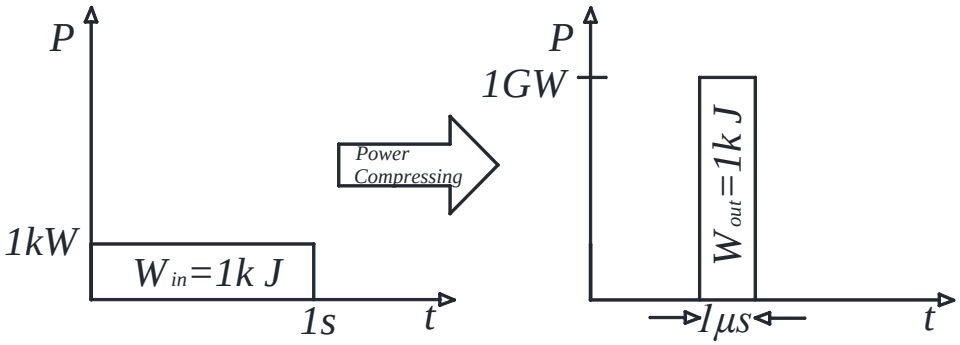

Figure 1-1. Example output of the pulse compression.

The typical pulsed power system shown in Figure 1-2 consists of a primary charging voltage source, an energy storage unit, a pulse-forming network, a switch, and a load. The primary charging voltage source provides power to the entire system and is typically DC power. Energy can be stored in various ways, such as through mechanical, chemical, electrostatic, and magnetic fields, with capacitors and inductors being the primary energy storage units used in pulsed power

systems [1].

Typical equivalent circuits and simulation outputs of Capacitor Energy Storage (CES) and Inductor Energy Storage (IES) using LTSpice are shown in Figure 1-3. Figure 1-3(a1) displays the typical equivalent circuits of CES pulsed power generators. The primary charging voltage for the system is supplied by the DC power source. R_1 acts as the current-limiting resistor, while C_1 stores the energy. S_1 is the switch responsible for operating the discharge of C_1 to the load, while R_2 is the load resistor. When S_1 turns on, the output energy is directly released from the capacitor to the load, as shown by the red line in Figure 1-3(a1). A typical output waveform of the CES circuit is presented in Figure 1-3(a2). For the RC circuit, the voltage on the load can be calculated using Equation (1-1). Additionally, based on Equation (1-2), the output energy on the load can be calculated using Equation (1-3), which is equivalent to the primary energy of the capacitor.

Figure 1-3(b1) illustrates the typical equivalent circuits of IES pulsed power generators. The main difference between CES and IES circuits is the energy storage and release method. The capacitor in the IES circuit is utilized to build up the primary current on the inductor. When S_1 is turned on, the discharge energy from the capacitors is temporarily stored in the inductor before being released to the load, as shown by the red line in Figure 1-3(b1). After S_1 is turned off, the energy from the inductor is released to the load, as depicted by the green line in Figure 1-3(b1). The current on the load can be calculated using Equation (1-4), where I_0 represents the peak current of the inductor. Equations (1-5) and (1-6) can be utilized to calculate the voltage and energy. The typical output waveform of the IES circuit is demonstrated in Figure 1-3(b2). The current waveform is for the inductor, and the voltage waveform is for the load. It is noteworthy that the charge voltage is 100V, while the peak voltage on the load is 1100V, which is significantly higher than the charge voltage. Typically, IES-based pulsed power circuits allow us

to drastically reduce the charging voltage for IES scheme pulsed power generators.

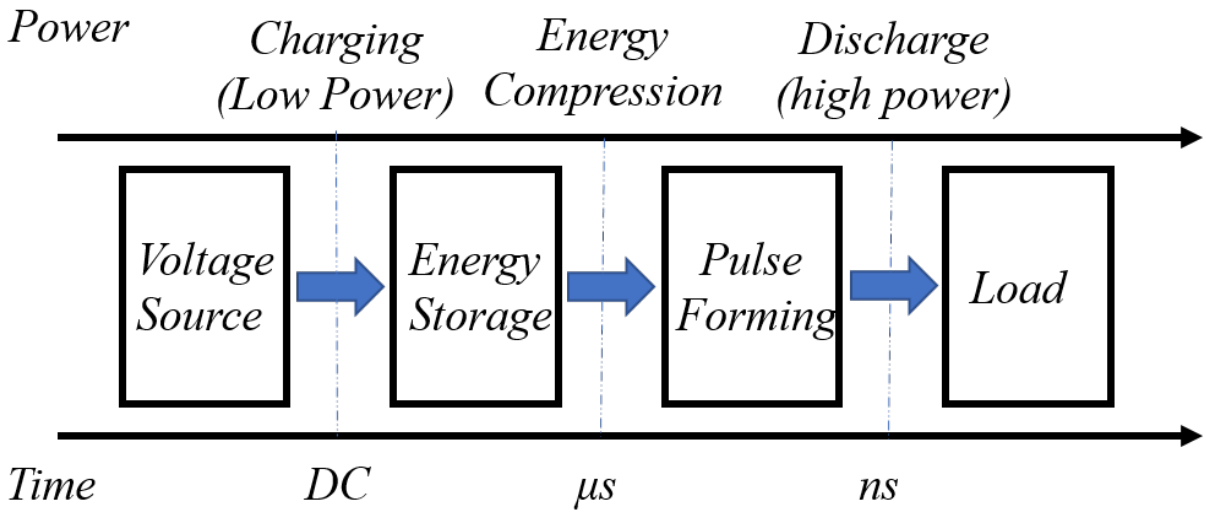

Figure 1-2. System composition of the pulse compression.

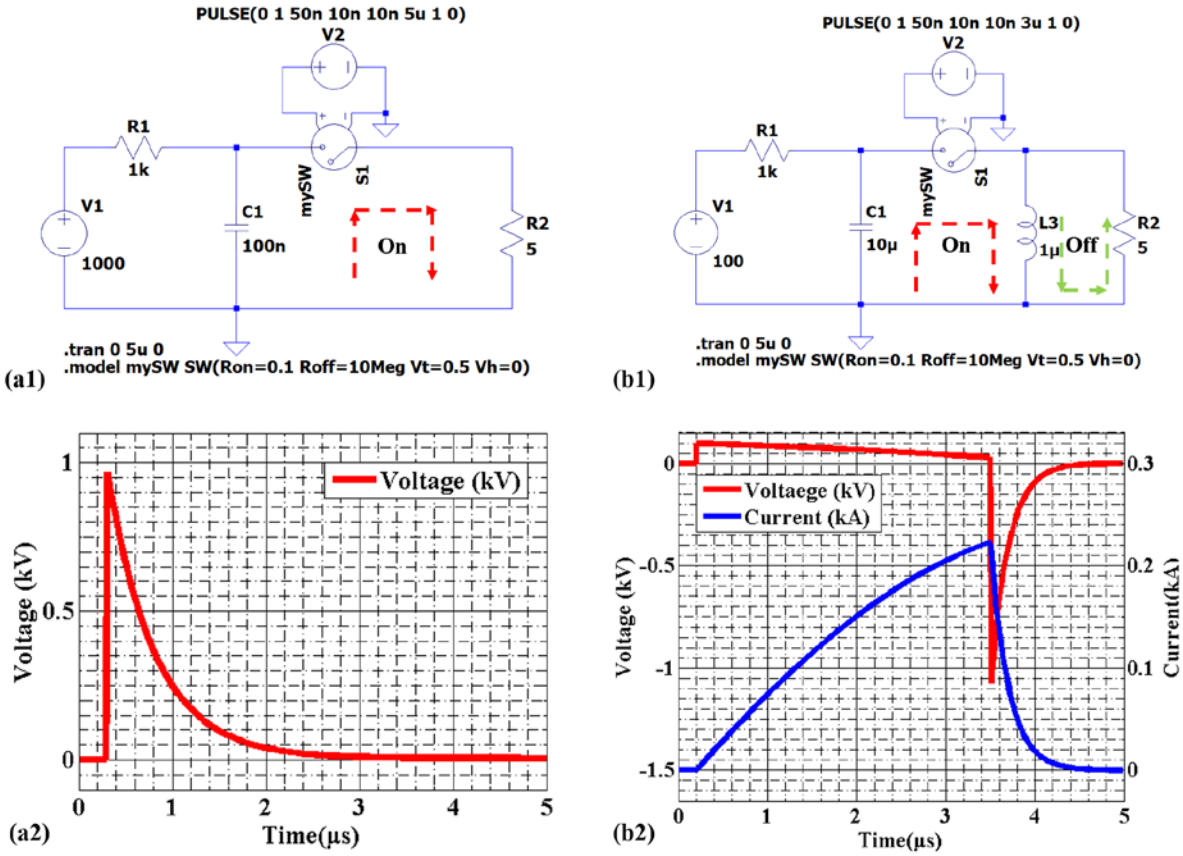

Figure 1-3. Typical capacitive energy storage (CES) and inductive energy storage (IES) circuits and their output waveforms obtained by LTSpice, (a) CES, (b) IES.

$$V(t) = V_0 exp(-\frac{t}{CR_2}) \tag{1-1}$$

$$I(t) = \frac{V_0}{R_2} exp(-\frac{t}{CR_2}) \tag{1-2}$$

$$W = \int_0^\infty V(t) \times I(t) dt = \frac{1}{2} CV_0^2 \tag{1-3}$$

$$I_R(t) = I_0 exp(-\frac{t}{L/R_2}) \tag{1-4}$$

$$V_R(t) = R \times I_R(t) = R_2 \times I_0 exp(-\frac{t}{L/R_2}) \tag{1-5}$$

$$W = \int_0^\infty V_R(t) I_R(t) dt = \frac{1}{2} LI_0^2 \tag{1-6}$$

1.2 Solid-State Pulsed Power Generator

Traditional large pulsed power generators mainly use gas switches, which limit the pulsed power used in the industry. However, as depicted in Figure 1-4, there has been a rapid development in solid-state switches in recent years. Magnetic switches and semiconductor switches have become the most widely used types in the pulsed power field [10]. Table 1-2 shows a performance comparison between gas spark switches and some typical solid-state switches [1]. With the advancement of solid-state switch technology, it is now possible to create compact, high-frequency, and flexible pulsed power generators, which promote the use of compact pulsed power technology in the industry. Pulsed power generators that use solid-state switches have more advantages in industry applications compared to traditional gas spark switch generators. Researchers have developed various pulsed power topology circuits based on the different characteristics of solid-state switches.

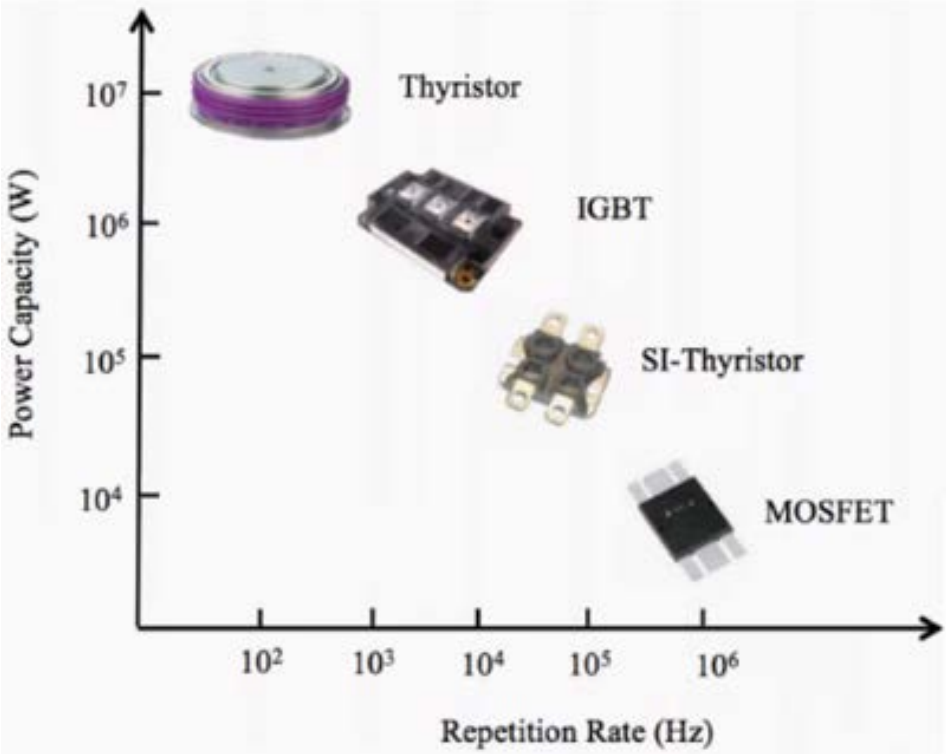

Figure 1-4. Some typical solid-state switches and their parameters.

Table 1-2. Performance comparison of gas spark switch with solid-state switches.

Device	Operating Voltage (kV)	Peak Current (kA)	Repetition Frequency(Hz)	Turn on / Turn off
Gas Spark Switch	~6000	~1000	~10	Depends on discharge breakdown, uncontrollable
Magnetic Switch	~1000	~1000	Depend on the reset time	Saturation operating parameter point
SOS Switch	~1000	~4	~1000	
MOSFET Switch	~4	~3	~100,000	Controlled by gate signal

1.2.1 Magnetic Switch

A magnetic switch is a new switch that is based on a magnetic core [11]. The essence of a magnetic switch is a saturable inductance surrounded by ferromagnetic material. The key point of a magnetic switch is the inductance change significantly before and after the magnetic core is saturated.

Figure 1-5 illustrates an equivalent model of a magnetic core, which consists of a saturable inductance surrounded by ferromagnetic material. In Figure 1-5(a), the model of the magnetic core is presented, while Figure 1-5(b) and (c) show its front view and sectional view, respectively. In Figure 1-5(b), rin, rout, and re represent the inner radius, outer diameter, and average radius of the core, respectively, where $r_e = (r_{out} + r_{in})/2$. The mean path length magnetic of the magnetic core is given by $l_e = 2\pi r_e$. Figure 1-5(c) shows that the cross-sectional area S of the magnetic core can be calculated as the product of the increments △r and △h.

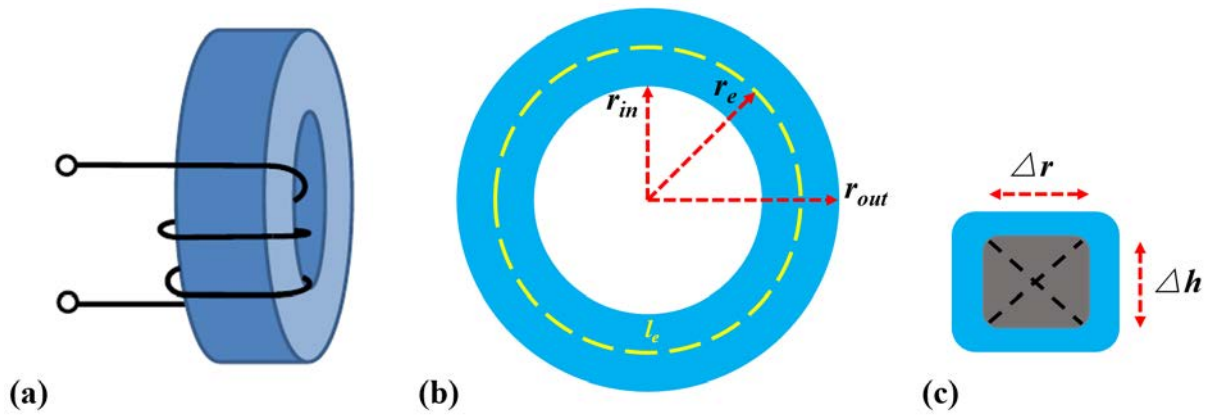

Figure 1-5. Equivalent model of magnetic core, (a) equivalent model, (b) front view, (c) sectional view.

Figure 1-6 shows a typical hysteresis loop of a magnetic core. The hysteresis loop illustrates the behavior of the magnetic core properties under different magnetic fields. Remanence flux density, B_r, is the residual magnetic flux density present in the core after the magnetic field is

removed. H_c, the coercive force, is the magnitude of the magnetic field required to bring B_r back to zero. The point at which further increase in H does not result in an increase in B is known as the saturation point of the core. The dashed lines in Figure 1-6 represent the saturation flux density, B_s, and the magnetizing force, H_s, required to saturate the core. The total flux swing, $\triangle B$, is from B_r to $-B_s$. The permeability of a magnetic material indicates how easily the material can be magnetized.

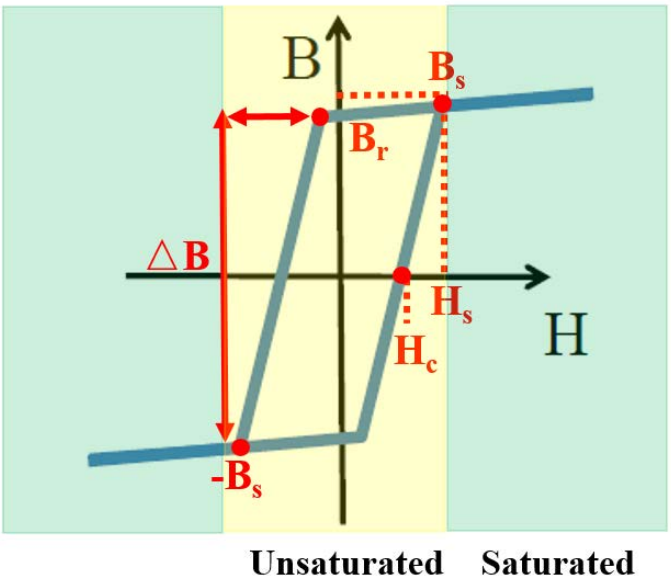

Figure 1-6. Typical hysteresis loop of magnetic core.

Relative permeability of the magnetic core μ_r is defined as the ratio of permeability μ to vacuum permeability μ_0 as shown in Equation (1-7).

$$\mu_r = \frac{\mu}{\mu_0}\frac{B}{H} \tag{1-7}$$

The inductance L of the magnetic core can be calculated by Equation (1-8). S is the cross-sectional area, μ is the permeability, N is the number of coil turns around the core, and l_e is the mean path length magnetic of the magnetic core.

$$L = \frac{\mu_0 \mu_r S N^2}{l_e} \tag{1-8}$$

Equation (1-8) indicated that the inductance of the core is proportional to the permeability. Based on Figure 1-6, it is not hard to understand that the permeability of the magnetic core in the unsaturated state is significantly higher than in the saturated state. Hence, the inductance of the magnetic core in the unsaturated state is significantly higher than in the saturated state. That is $L_{un} \gg L_{sat}$. Also, that is the key point of a magnetic switch.

The principle of the magnetic switch is shown in Figure 1-7. As shown in Figure 1-7(a), the hysteresis point of the magnetic switch is reset to ($-B_s$,$-H_s$) before voltage is applied to it, and there is no voltage applied to the magnetic core. When a high voltage V is applied to the magnetic core, the magnetic flux density B starts moving from $-B_s$ towards B_s, as shown in Figure 1-7(b). The magnetic switch is turned off and held at a voltage V. After the voltage is applied for a time $\triangle t$, the magnetic flux density reaches the saturation flux density B_s. Because the magnetic core remains unsaturated until the magnetic flux density reaches B_s, the inductance of the magnetic core is significantly larger than when the core is saturated. Hence, the magnetic switch remains turned off and held at a voltage V within $\triangle t$, as shown in Figure 1-7(c). Finally, the voltage V is continuously applied to the magnetic core until the core is saturated, causing the inductance of the magnetic switch to drop and the magnetic switch to turn on. As a result, the voltage on the magnetic core drops, and the current increases significantly, as shown in Figure 1-7(d). The relationship between the applied voltage V and the inductance L can be described by Equation (1-9). Based on Equation (1-9), we can establish the relationship between the applied voltage and the parameters of the magnetic core, which are shown in Equation (1-10). V and $\triangle t$ are the applied voltage and time on the magnetic core, respectively. N is the number of turns of the

magnetic core winding. S is the cross-sectional area, and △B is the total flux swing. Equation (1-10) indicates that the switching on or off of the magnetic switch depends heavily on the parameters of the magnetic core. For a magnetic core, the product of the applied voltage and the applied time is determined.

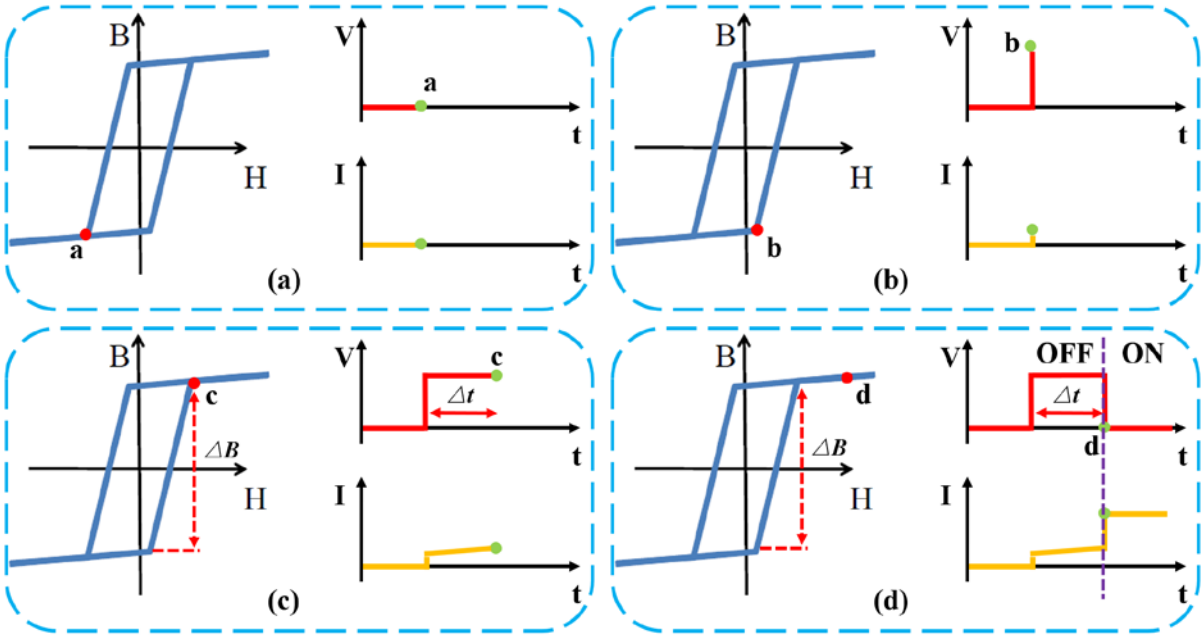

Figure 1-7. Principle of magnetic switch.

$$V = L\frac{\mathrm{d}I}{\mathrm{d}t} \tag{1-9}$$

$$V \triangle t = L \triangle I = \frac{\triangle \phi}{\triangle I} \triangle I = NS \triangle B \tag{1-10}$$

The advantages of the magnetic switch are that it can carry high voltage (~1000 kV) and large current (~1000 kA) on the pulse circuit. Also, it can be operated at high frequency. However, the switch on or off of the magnetic switch is deeply dependent on the parameter of the magnetic core. Once the magnetic core parameters are determined, the parameter of the magnetic switch

is determined, too, which is hard to provide a flexible pulse waveform in the pulsed power circuit. And before the magnetic switch is used in the pulsed circuit, it must be reset to the unsaturated state.

Based on the character of the magnetic switch, a typical application for the magnetic switch is for the magnetic pulse compression circuit, which is widely used in pulsed power fields [12]. A traditional pulse compression circuit is shown in Figure 1-8. Figure 1-8(a) shows the equivalent of the pulse compression. The critical point of the pulse compression circuit is $C_1 = C_2$, and $L_1 \gg L_2$. When switch S turns on, the energy of the C_1 transforms to the C_2. When switch S_2 is conducted, the energy of C_2 is released to the load. The current waveforms of I_1 and I_2 are shown in Figure 1-8(b). Compared with I_1, the waveform of I_2 is significantly sharper, and the rise time is shorter. Thus, the carried voltage and current requirement of S_2 is more strict than S_1. Traditional S_2 uses the gas spark switch. When S_1 conducts, the energy is transformed to C_2, and the switch S_2 carries the high voltage of C_2. However, the gas may break down and the gas spark switch may conduct when it reaches the gas discharge voltage. After the circuit discharge, it cannot be reoperated until the gas is recovered. This process may take a long time, and the conduct of the gas spark switch is uncontrollable. This is the main disadvantage of using a traditional gas spark switch for the pulse compression circuit.

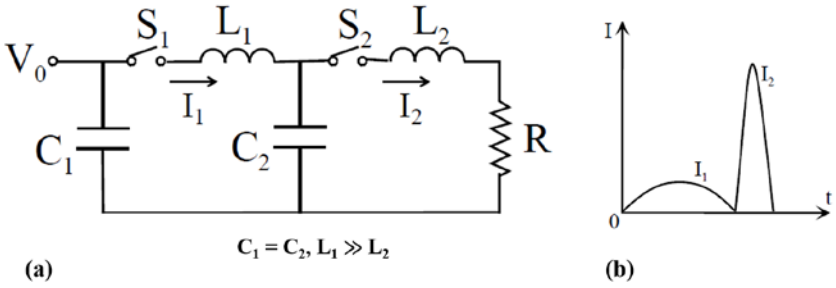

Figure 1-8. Principle of pulse compression.

Due to its characteristics, such as the ability to change inductance before and after saturation, carry high voltage and current, and be repeatedly operated, the magnetic switch is an ideal component for use in pulse compression circuits.

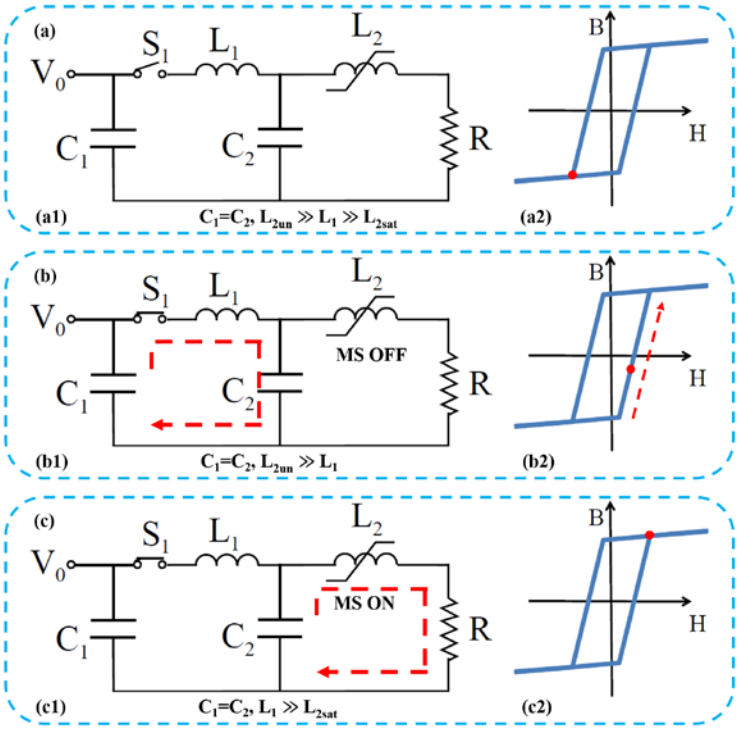

Figure 1-9. Equivalent circuit and principle of magnetic pulse compression.

A typical magnetic pulse compression circuit and its principle are shown in Figure 1-9. Figure 1-9(a) shows the equivalent circuit of magnetic pulse compression (a1) and the hysteresis loop model of the magnetic switch (a2). C_1 is charged to V_0, and S_1 is turned off. The magnetic switch is reset to the unsaturated state, so the inductance of the magnetic switch L_{2un} is much larger than L_1. As shown in Figure 1-9(b), when switch S_1 turns on, the energy of C_1 is transferred to C_2. The magnetic switch carries the voltage of C_2, causing the flux density point B to move from $-B_s$ to B_s. Considering that the magnetic switch (MS) is in an unsaturated state, it remains off in the circuit. With appropriately designed parameters, the magnetic core saturates and MS

turns on immediately when the energy of C_1 transformer is completely transferred to C_2, as shown in Figure 1-9(c). When the magnetic core is saturated, the inductance of the core drops significantly, resulting in $L_1 \gg L_{2sat}$. Therefore, the output waveform on the load becomes compressed, as shown in Figure 1-8(b).

A typical magnetic pulse compression simulation circuit by LTSpice is shown in Figure 1-10. The detailed parameter information can be seen in the circuit Figure 1-10(a). L_1 is 10 μ H. L_2 is the model of the magnetic switch. The output waveform of I_1 and I_2 is shown in Figure 1-10(b). Compared with I_1, the waveform of I_2 is significantly sharper, and the rise time is shorter.

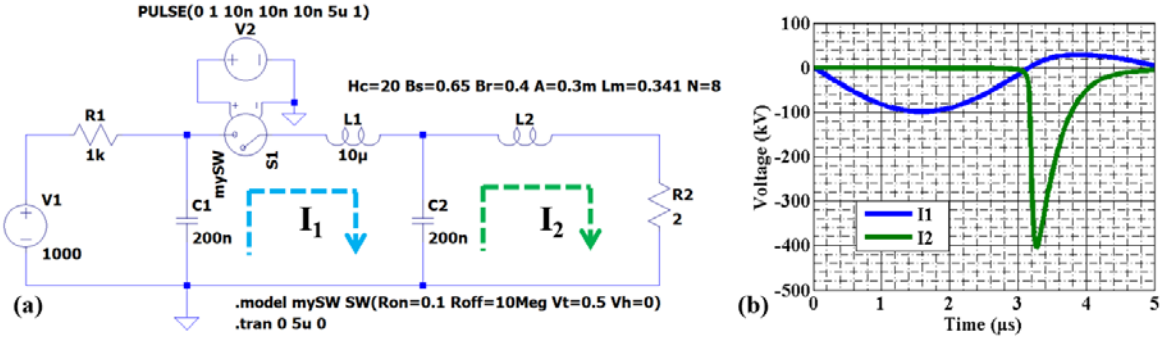

Figure 1-10. Magnetic pulse compression simulation circuit, (a) equivalent circuit, (b) discharge waveforms.

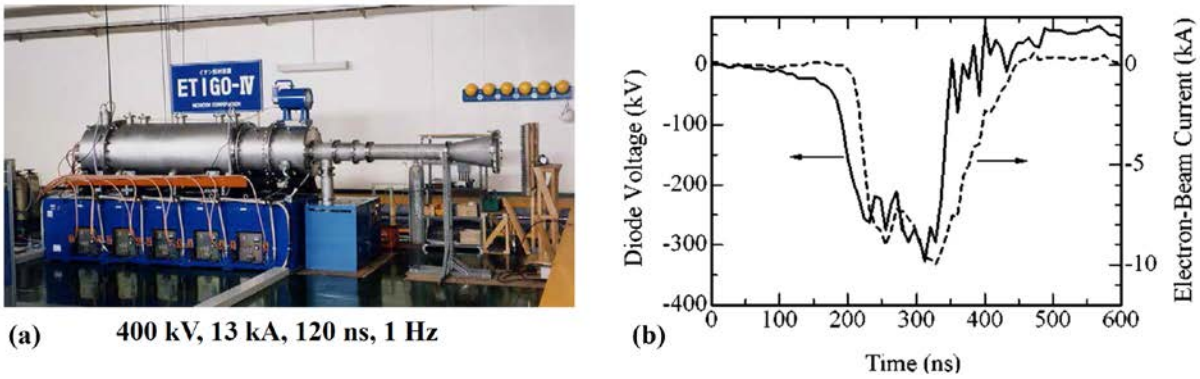

Figure 1-11. ETIGO VI, (a) photograph, (b) discharge waveforms.

Based on the concept of MPC, a large pulsed power, ETIGO VI, was built at Nagaoka University of Technology, Japan, in 2000 [12]. The photograph and main parameter of ETIGO VI are shown in Figure 1-11(a). And a typical output waveform using ETIGO VI is shown in Figure 1-11(b).

Table 1-3. Parameter of MPC circuit used in G41K Excimer laser.

Transmission	Time(μs)	Peak Current (kA)	Total Inductance (nH)
$C_0 \rightarrow C_1(I_0)$	4.4	2.6	2580
$C_1 \rightarrow C_2(I_1)$	1.0	9.4	160
$C_2 \rightarrow Load(I_2)$	0.55	30	25

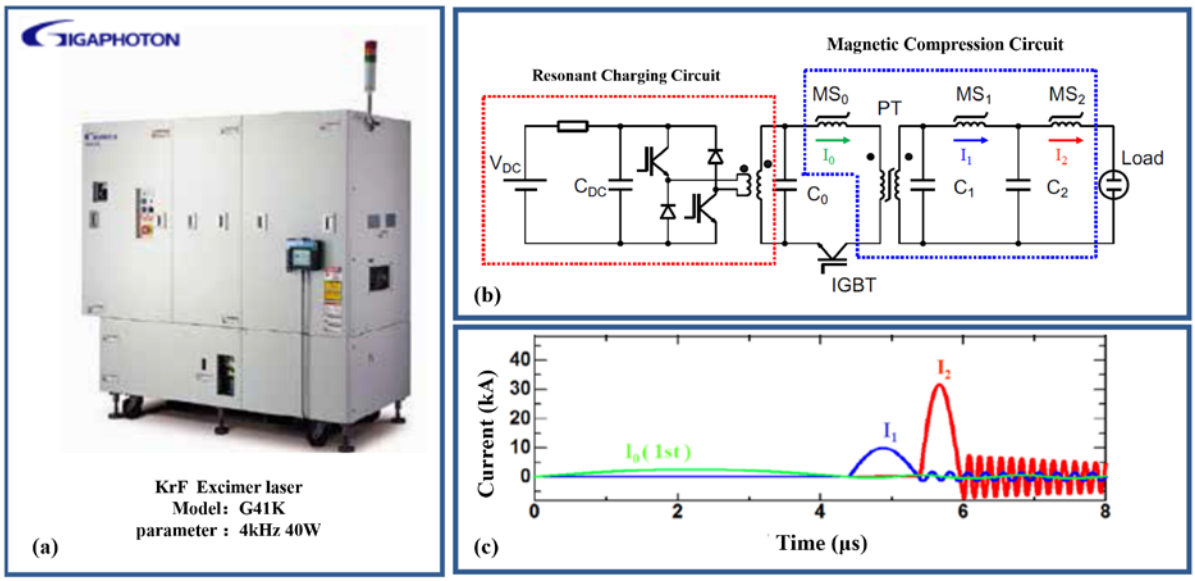

Figure 1-12. MPC circuit used in G41K Excimer laser, (a) photograph of G41K, (b) MPC circuit, (c) discharge waveforms.

As for the excimer laser industry field, a pulse with several hundreds of nanosecond lengths and a short rise time is required. Taking into consideration the features of the MPC circuit, it has a unique advantage in the excimer laser industry field. A typical MPC circuit application is the

EVU Excimer Laser, designed by GIGAPHOTON [13]. The photograph of the EVU Excimer Laser model of G41K is shown in Figure 1-12(a). The equivalent circuit of MPC is shown in Figure 1-12(b). The MPC circuit in the G41K is composed of three-stage pulse compression. The parameters of each stage can be seen in Table 1-3. With the inductance of each stage decreasing, the peak current increases significantly. And a typical output waveform obtained by the MCP circuit is shown in Figure 1-12(c).

1.2.2 Semiconductor Open Switch (SOS)

Another circuit that utilizes a solid-state switch scheme to meet the pulse circuit requirements of the excimer laser industry is the semiconductor open switch (SOS) pulse circuit. The SOS pulse circuit was developed by the Institute of High-Current Electronics (IHCE) of the Russian Academy of Science. It uses the SOS to generate a sharp voltage spike followed by a relatively long capacitor discharge pulse. The nature of the SOS is that of a high-power pulse diode. Ideally, the voltage and current waveform through the diode should behave as shown in Figure 1-13(a), with the current interrupted immediately when a reverse voltage is applied to the diode. However, the actual current waveform of the diode is shown in Figure 1-13(b), where there is a small reverse current through the diode, and the reverse current is cut off for a short time. Based on this phenomenon, researchers have developed the concept that a high voltage on the load can be obtained by increasing the inductance of the diode circuit and interrupting currents at density levels up to the top, as shown in Figure 1-13(c). This is the basic principle of the SOS [14].

Based on the above discussion, Figure 1-14 illustrates the operating principle of the SOS. First, a forward current is applied to the SOS as shown in Figure 1-14(a). Next, a reverse current

is drawn from the SOS, as shown in Figure 1-14(b). Finally, taking advantage of the nature of the SOS, the reverse current is immediately interrupted, resulting in a high-voltage pulse being generated on the load, as shown in Figure 1-14(c).

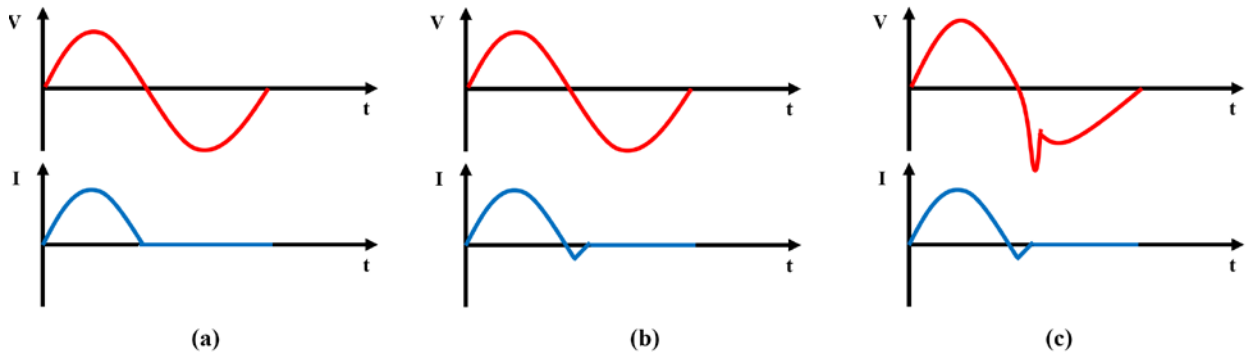

Figure 1-13. Waveform on the diode, (a) ideal diode, (b) actual diode, (c) SOS diode.

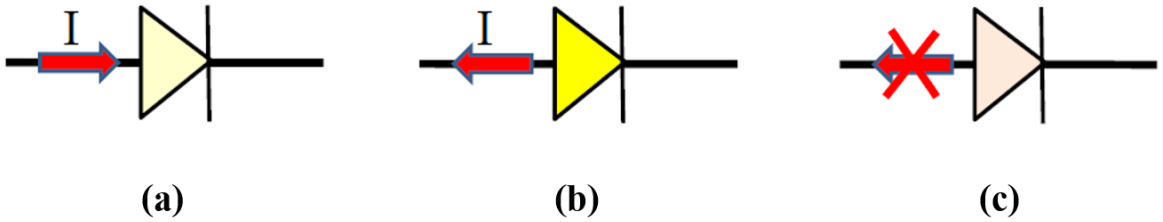

Figure 1-14. Operated principle of the SOS, (a) forward input current, (b) reverse draw current, (c) reverse interrupting current.

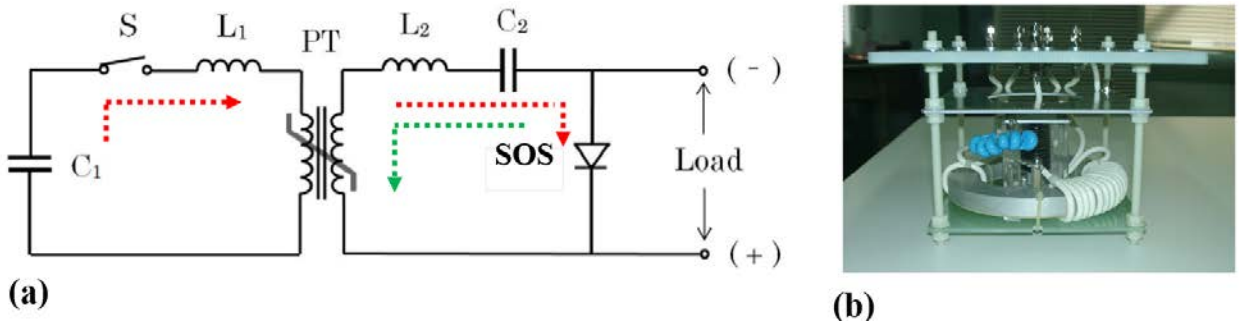

Figure 1-15. Typical SOS pulsed circuit, (a) typical equivalent circuit, (b) photograph.

Figure 1-15 shows a typical pulse circuit and photograph based on SOS [15]. Figure 1-15(a)

shows the equivalent circuit, and Figure 1-15(b) shows the photograph. In the circuit, the saturable transformer feature of the magnetic core is used. When switch S in the primary circuit is turned on, the energy of C_1 is transferred to C_2 through the magnetic core, as shown in the red line in Figure 1-15(a). During the charging process of C_2, SOS injects current. When the magnetic core is saturated, C_2 discharges and draws away the current of SOS, as shown in the green line in Figure 1-15(a). Figure 1-16(a) shows the primary and secondary output waveforms. When the current is drawn away from the current of SOS, a high voltage pulse is output on the load, as shown in Figure 1-16(b). It is worth noting that, similar to inductive energy storage, the output voltage of SOS is load-dependent. When the load resistance decreases, the SOS output voltage decreases, while the output current increases.

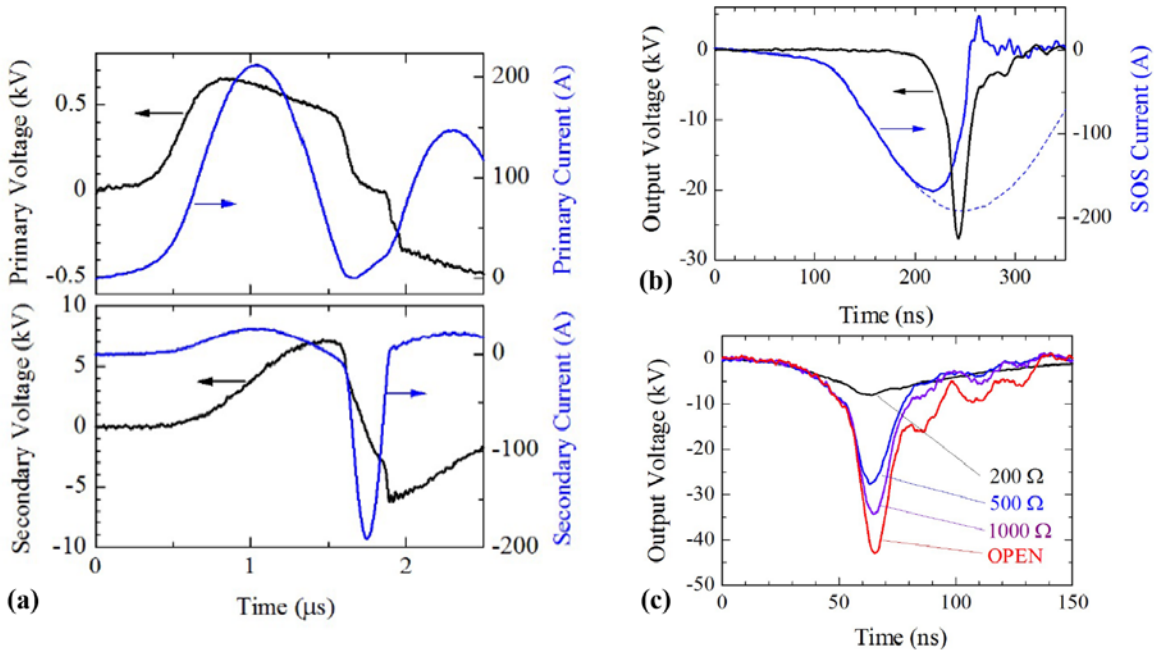

Figure 1-16. Typical output waveform using SOS pulsed circuit shown in Figure 1-15, (a) voltaeg and current waveforn on the primary and secondary side, (b) output waveform on the load, (c) output waveform on the load with different resistor.

1.2.3 Metal-Oxide-Semiconductor Field-Effect Transistor (MOSFET) Switch

The solid-state switches mentioned in the previous chapters have different application scenarios depending on their performance. Although these solid-state switches are somewhat more flexible in operation than gas switches, once the parameters of the magnetic switch are determined, the on and off times of these switches will also be determined, which is unable to achieve user freedom of control. Scientists have recently developed semiconductor switches based on Metal-Oxide-Semiconductor Field-Effect Transistor (MOSFET) [16]. The user can control the opening and closing of the switch through an electronic signal.

The traditional Metal–Oxide–Semiconductor (MOS) structure is obtained by growing a layer of silicon dioxide (SiO_2) on top of a silicon substrate, commonly by thermal oxidation and depositing a layer of metal or polycrystalline silicon (the latter is commonly used). As silicon dioxide is a dielectric material, its structure is equivalent to a planar capacitor, with one of the electrodes replaced by a semiconductor.

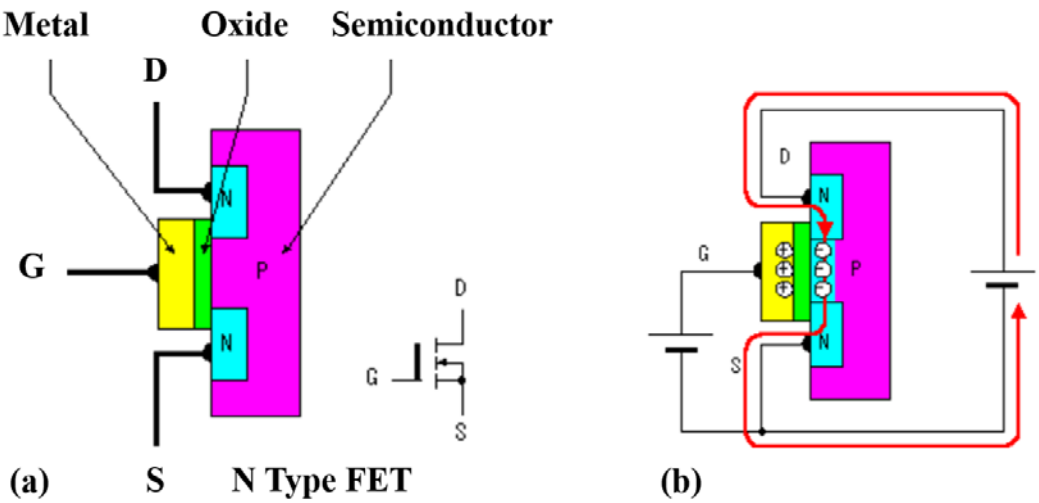

Figure 1-17. Typical model of MOSFET switch, (a) MOSFET model, (b) MOSFET switch in turn status.

Figure 1-17(a) shows a typical N-Type MOSFET switch model. The MOSFET structure includes Drain (D), Source (S), and Gate (G). When a voltage is applied across a MOS structure in G, it changes the distribution of charges in the semiconductor. Thus, the MOSFET switch is conducted, shown in Figure 1-17(b). Reverse, the MOSFET switch is turned off when the voltage is removed from G. Such a voltage can be achieved using an electronic signal. Therefore, the user can turn the MOSFET switch on and off independently and controllably.

However, as mentioned in Table 1-2, the operating voltage of the MOSFET switch is much lower than any other solid-state switch. Thus, it is hard for the MOSFET switch to be used in high-voltage conditions.

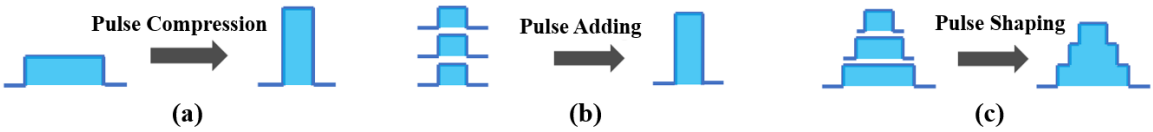

Figure 1-18. Concept of (a) pulse compression,(b) pulse adding, and (c) pulse shaping.

Luckily, the concept of a modular pulsed power generator has been developed in recent years. Modular pulsed power is much different from pulsed compression type pulsed power generator. From the previous description, it is not hard to find that pulsed power generated in pulse compressing offers very limited flexibility in the output waveform variation, as shown in Figure 1-18(a). Specifically, the high-power pulses obtained by pulse compression cannot be used to adjust the pulse output waveform according to the needs of the user. However, the pulsed power generator with flexible waveform has significant applications in the industrial field. Over the last decades, a new way of pulsed power generator has been developed that a high-power pulse can be obtained by many synchronous module low-power pulses output on the same load, as shown

in Figure 1-18(b). In principle, any sharp pulse waveform can be obtained by some proper synchronized small module lower power pulsed adding, as shown in Figure 1-18(c).

In this case, this pulsed power system provides more flexible waveforms than traditional MPC or SOS pulsed power generators. By combining the concept of modular design and solid-state switch technology, two typical examples of modular pulsed power topology circuits are Solid-State Marx (SSMarx) and Solid-State Linear Transformer Drivers (SSLTD) [17][18] .

A typical equivalent circuit of SSMarx is shown in Figure 1-19(a). The charge and discharge principle of SSMarx are shown in Figure 1-19(b). The circuit generates a high-voltage pulse by charging a number of capacitors in parallel, then suddenly connecting them in series.

- Charging process. The charging process is shown in Figure 1-19(b). The solid-state switch of each module is kept turned off. The DC charge circuit is shown in the red line through the diode to charge each capacitor. The DC charge voltage we set as V_0. Thus, the charge voltage of the capacitor equals V_0-(n+1)V_f. n is the stage number of the Solid-State Marx. V_f is the forward voltage of the diode. Usually, V_f is less than 1.2V, much less than V_0. Thus, V_f can be ignored. The capacitor voltage of each module is near V_0.

- Discharging process. The discharge process is shown in Figure 1-19(c). The solid-state switch of each module is turned on. Each capacitor is connected in series to discharge the load. The discharge circuit is shown in the blue line. The discharge voltage on the load is -nV_0.

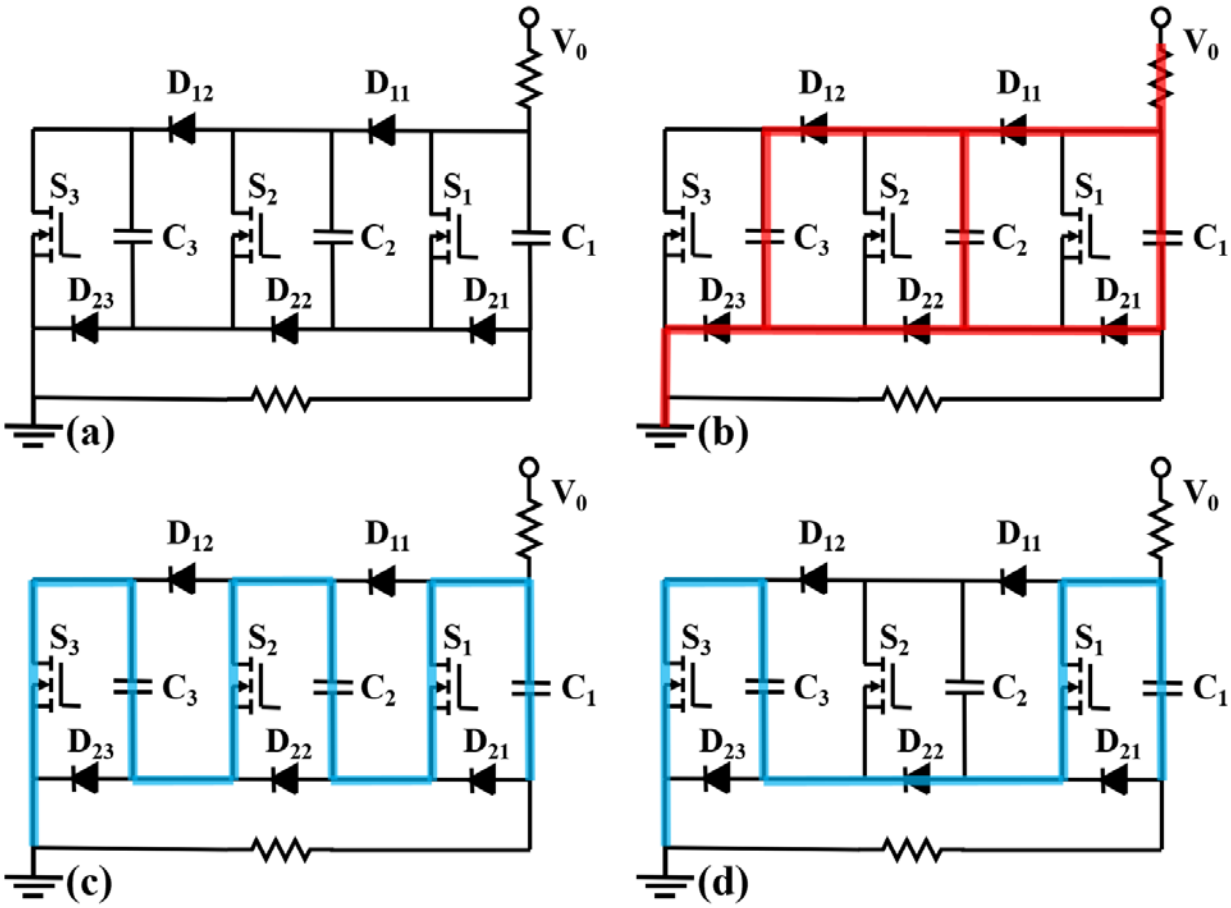

Figure 1-19. Solid-State Marx circuit, (a) equivalent circuit, (b) charging process, (c) discharging process, (d) offside discharging process.

As the modular pulsed power generator, a typical characteristic of the SSMarx is it can work in an offside state. The principle of the offside state is shown in Figure 1-19(d). When SW_1 and SW_3 are turned on while SW_2 is turned off, the diode of D_2 will conduct automatically to connect the capacitors C_1 and C_3, avoiding the SW_2 damage by the high voltage. The output circuit is shown in the green line. The equivalent circuit is shown in Figure 1-19(d). All of the capacitors are charged to V_0. And the discharge voltage on the load is $2 \times V_0$. SSMarx circuit with an offside state indicated that it is not necessary to turn all modules simultaneously. Hence, a flexible pulse waveform is possibly generated by the SSMarx circuit. A typical SSMarx simulation and

experiment circuits are shown in Figure 1-20. Figure 1-20(a1) shows the simulation circuit.The detailed parameter information can be seen in the simulation circuit. The charge voltage is 500V. When the switches are turned on simultaneously, the output voltage of -1500V on the load is confirmed, as is shown in Figure 1-20(a2). When we turn on or off different modules at different times, we can obtain flexible output waveforms, as shown in Figure 1-20(a3).

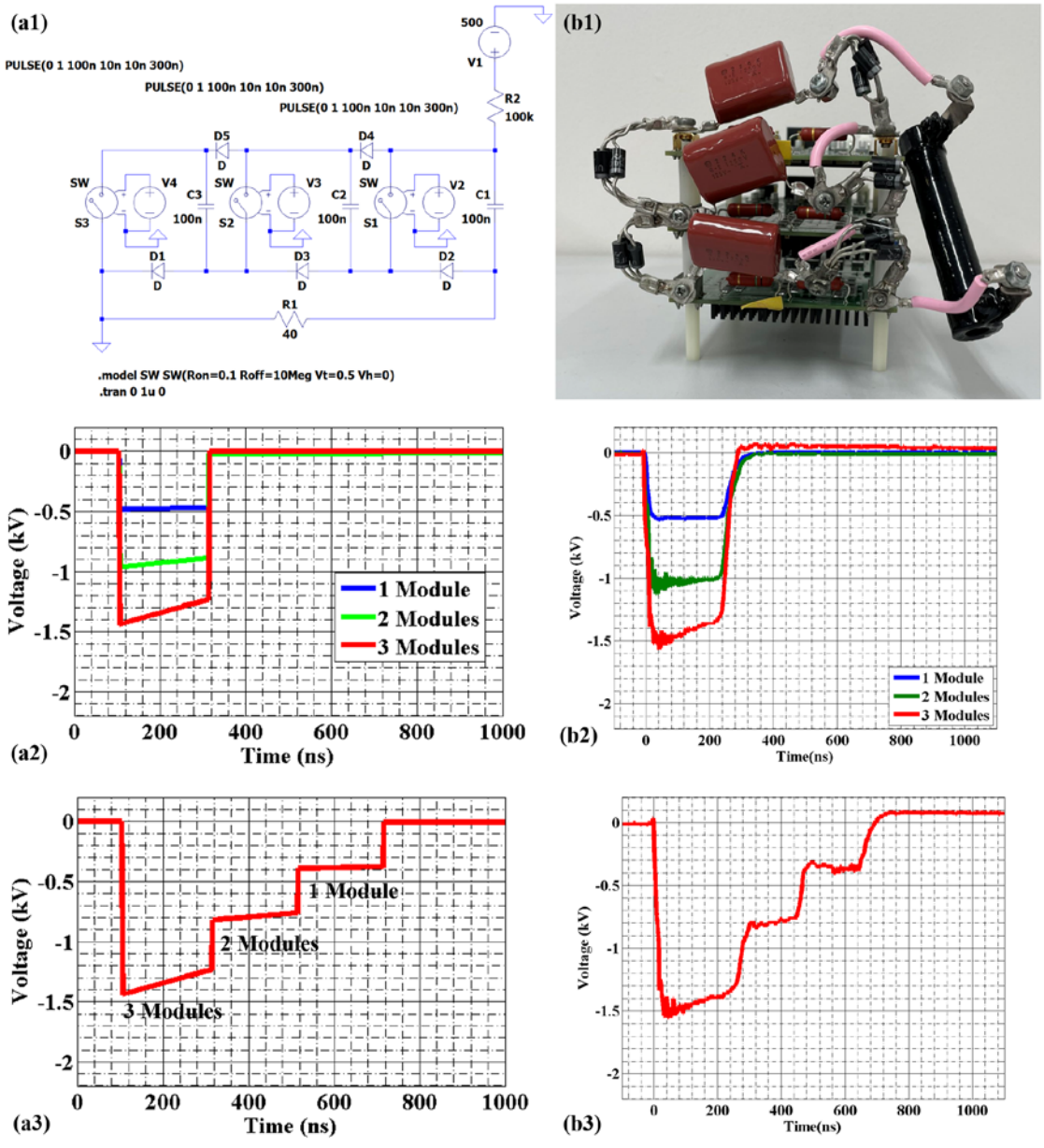

Figure 1-20. Solid-State Marx circuit, (a) simulation, (b) photograph.

Based on previous discussion and simulation, a photograph of SSMarx with 3 modules is shown in Figure 1-20(b1). The main component of green PCB is the MOSFET switch. The main parameter of the SSMAR circuit is almost near the same as the simulation shown in Figure 1-20(a1). Figure 1-20(b2) shows the output waveforms with different modules operated. Figure 1-20(b3) shows the pulse shaping by different modules turned on at different times. The experiment results are nearly the same as the simulation results shown in Figure 1-20(b) and Figure 1-20(c).

Another typical modular solid-state pulsed power generator is SSLTD. Detailed information on the SSLTD is illustrated in Chapter II.

1.3 Typical Applications of Solid-State Pulsed power Generators

With the development of solid-state switch technology, pulsed power technology has transitioned from its original defense applications into the industrial sector, leading to the convergence and advancement of various disciplines.

Especially when using nanosecond pulsed power devices to discharge atmospheric pressure gases and generate plasmas, a large number of high-energy electrons and ions are produced due to the high electric field generated in a short period of time by the nanosecond pulsed power. Due to the extremely short duration of the nanosecond pulse and the huge difference in mass between the electrons and ions generated during ionization, the electrons can move at high speeds and impact target objects during the discharge period, while the motion of the ions remains almost unchanged. This can maintain the low-temperature state of the plasma generated by using nanosecond pulse gas discharge. Such low-temperature plasmas have great potential for industrial applications, such as wastewater treatment, exhaust gas treatment, sterilization and disinfection, and food preservation.

In this section, we will provide a brief introduction to some typical industrial applications of pulsed power and the associated challenges encountered during their implementation.

1.3.1 Pulsed power Technology used in Cancer Treatment

As a new approach to cancer treatment, pulsed electric field therapy has received increasing attention in recent years. The primary goal of cancer treatment is to kill cancer cells. Unlike conventional therapies such as surgery, medication, and radiation, pulsed electric field therapy stimulates cancer cells through an external pulsed electric field, inducing them to undergo apoptosis on their own. In other words, the objective of pulsed electric field therapy is not to physically destroy cancer cells but to induce them to undergo their inherent programmed cell death process, thereby achieving the therapeutic purpose. Therefore, the biological mechanism of pulsed electric field therapy is relatively complex. Although research in this field is still in its early stages, if breakthroughs are made in the mechanisms and control methods, pulsed electric field therapy could make a significant contribution to cancer medicine.

Experimental results have shown that one of the key technical factors in pulsed electric field therapy is the pulse waveform. Research conducted at Chongqing University in China has indicated that compared to a single constant parameter pulse, synergistic pulse combinations (high-voltage narrow pulses and low-voltage wide pulses) exhibit more pronounced advantages in terms of cancer cell lethality.

Figure 1-21 presents the schematic diagram of the experimental setup used by Chongqing University for cancer cell treatment, as well as the experimental results [19]. Figure 1-21(a) shows the experimental setup, and Figure 1-21(b) displays the cancer cell treatment results under different pulse conditions. In this context, HSV stands for High Short Voltage, and LLV

represents Long Low Voltage. The experimental results demonstrate that the mixed pulse electric field yields better treatment effects on cancer cells compared to the single pulse electric field condition.

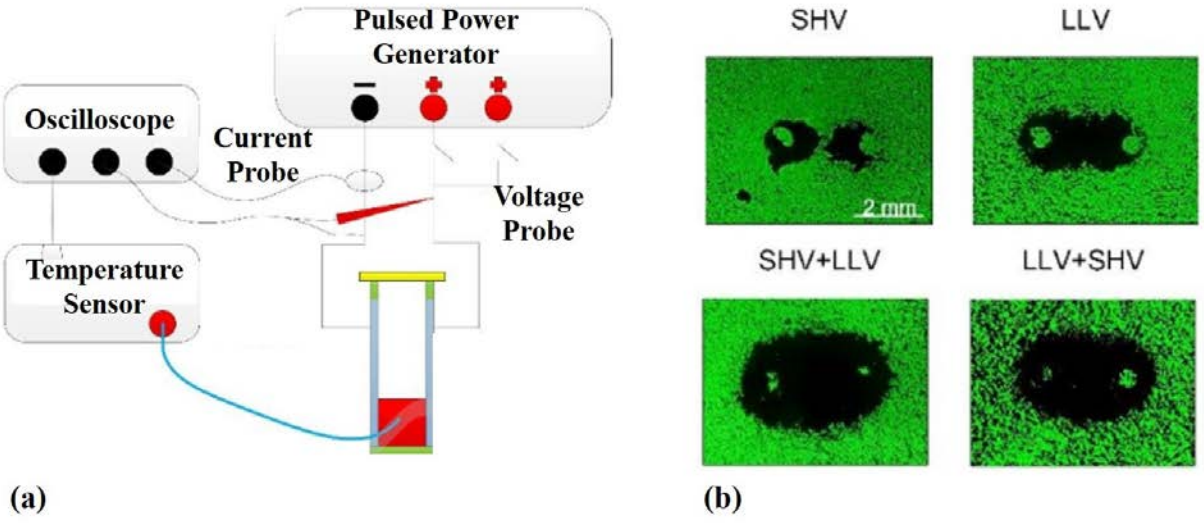

Figure 1-21. Pulsed power used in cancer treatment, (a) experimental apparatus, (b) typical results.

1.3.2 Pulsed power Technology used in Gas Treatment

One of the important goals of waste gas treatment is denitrification. The current main denitrification technologies use catalysts. Various plasma treatment technologies based on gas discharge have been studied for a long time, but so far they have not reached a practical level. Although the chemical role of plasma in denitrification reactions is well understood, practical devices must meet certain conditions in terms of energy efficiency and lifespan.

Gas treatment methods using plasma are mainly based on electron collision dissociation and control of chemical bonding pathways. Collision dissociation requires electrons in the plasma to have sufficiently high kinetic energy (several eV). On the other hand, ions and neutral particles in the plasma must be at or near room temperature. Therefore, this is a non-equilibrium plasma.

As mentioned earlier, pulse gas discharge is one of the methods for generating non-equilibrium plasma. Gas between the electrodes undergoes breakdown under the action of high electric fields. Jet-type discharge generates a large number of free electrons, which are accelerated and collide with gas molecules under the influence of the applied electric field. In atmospheric pressure gas without using a blocking medium, jet discharge eventually develops into arc discharge. The characteristic of pulse gas discharge is that it ends before the arc channel is fully formed.

Figure 1-22 shows typical experimental results of NO and NO_2 decomposition using pulse gas discharge. With increasing repetition frequency of pulse discharge within a fixed time, the removal efficiency of NO and NO_2 approaches 100%. This demonstrates the decomposition effect of gas discharge on nitrogen oxides [20].

Furthermore, as shown in Figure 1-23, comparing different types of pulse discharge methods such as DBD (Dielectric Barrier Discharge), Pulsed Corona Discharge, and Nanosecond Pulsed Discharge, it can be observed that Nanosecond Pulsed Discharge has significant advantages in terms of NO removal efficiency and energy efficiency.

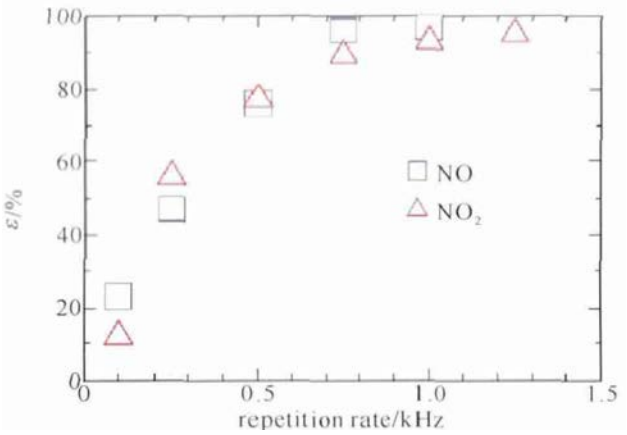

Figure 1-22. NO and NO2 removal rate as a function of repetition rate.

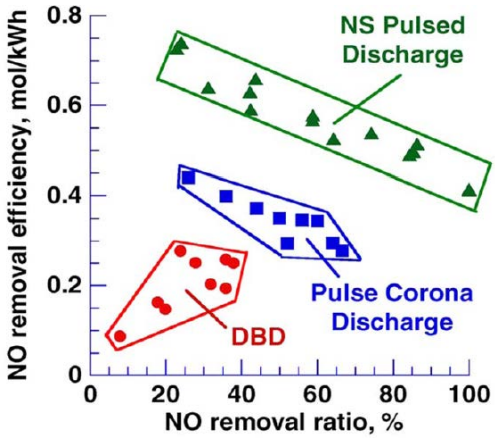

Figure 1-23. Different types of pulsed discharge devices and their effects on NO removal.

1.3.3 Pulsed power Technology used in Water Treatment

With the increasing requirements from governments worldwide for the quality of wastewater discharge and the reuse of wastewater, large-scale emission industries, mainly in the semiconductor manufacturing sector, are exploring technological approaches to establish environmentally friendly production methods. One important aspect is the removal of harmful components from wastewater to reduce emissions and enhance water reuse. Currently, chemical and biological methods are predominantly employed. In the future, pulsed power plasma treatment of wastewater is expected to become popular as an auxiliary method.

Plasma technology has evolved from gas treatment to liquid treatment. The concept is fundamentally similar, involving the direct or indirect decomposition of harmful substances through electron collisions. However, compared to gas, the breakdown field strength in liquids is much higher, and the range of action of metastable particles in liquids is limited. A practical approach is to perform the discharge under conditions where the liquid and gas are mixed. For example, a simple method is to discharge near the liquid surface, while a more complex method involves injecting gas bubbles into the liquid or spraying water droplets into the gas before

initiating the discharge. In these cases, the discharge primarily occurs in the gas phase, and the generated free radicals interact with the liquid molecules across the liquid-gas interface.

Figure 1-24 presents a schematic diagram of a typical spray discharge liquid treatment experimental setup using pulsed power technology for water treatment. It employs a nozzle to spray fine droplets within a coaxial discharge region. With the action of a water pump, the liquid is circulated and subjected to multiple treatments. When the treated liquid is a dilute solution of indigo carmine, the color variation over time is shown in Figure 1-25 [21].

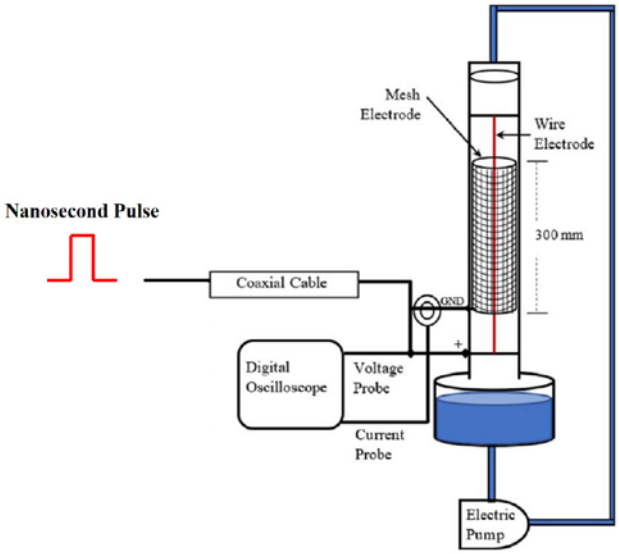

Figure 1-24. Typical pulsed power water treatment system.

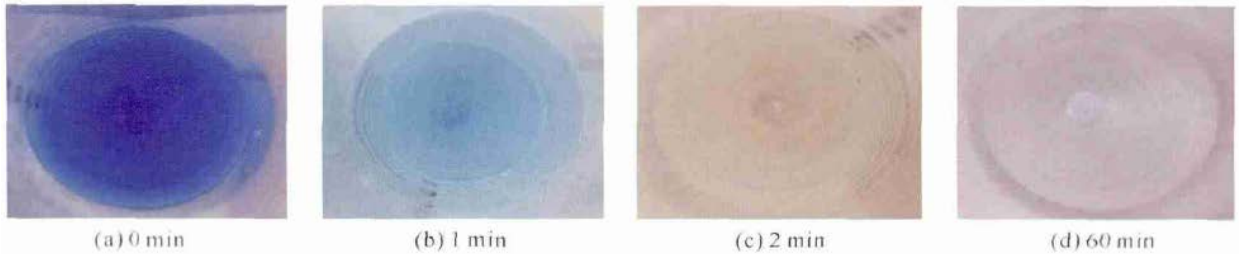

Figure 1-25. Color change of the sample liquid, which is water diluted indigo carmine.

1.4 Application Issues of the Pulsed power Technology

1.4.1 Future Development Trends of Pulsed Power Generators

Pulsed power technology is a branch in the field of electrical engineering. It fully utilizes high power by using short pulses as the main means to produce unique phenomena or effects. The main goal of compact pulsed power technology is industrial applications. While relying on and borrowing from peripheral technology achievements, pulsed power has formed a unique technical system after years of development. Pulsed power sources have also penetrated into many practical applications in industrial production and scientific research. However, the current development progress of pulsed power technology is still far from meeting the actual industrial application needs. The following are the directions for exploring the future development of pulsed power generator technology [22].

- Flexible Output

Industrial pulsed power generators are usually designed with specific parameter targets in mind. All components of the system are optimized to achieve this goal, which often makes it difficult to change the output parameters of the pulsed power generators. This is particularly evident in magnetic pulse compression circuits, which are currently the main technology used in industrial pulsed power applications. Due to the fact that the output time of magnetic switches is determined by parameter conditions rather than external control, the normal output parameter range of this technology is very limited.

The variability of the output parameters of pulsed power generators is related to their range of applicability, as different applications require different parameters. So far, the development of pulsed power generators has been based on the idea of specialization, which means developing

power generators specifically for a certain need, targeting a specific parameter. There are few pulsed power generators designed to cover a range of parameters from the outset.

As pulsed power applications become more widespread and mature, the trend toward the universality of pulsed power generators is inevitable. Although there are many pulsed power parameters, and each parameter has a wide range, a pulsed power generator that can only output a fixed parameter will eventually lose its market competitiveness.

However, in industrial applications, the flexibility of pulsed power parameters deeply affects the effectiveness of pulsed power in industrial applications, especially as a low-temperature plasma source. Therefore, the development of pulsed power sources with flexible and controllable parameters is crucial for the industrial application of pulsed power technology.

- Modularization

Compact pulsed power is aimed at industrial applications, with standardization and low cost as the main development directions. Therefore, modularization is inevitably the most promising way for its future development.

The key to modularization technology is pulse adding, which includes not only strict synchronous control but also intentional time-delay pulse adding. The purpose of synchronous synthesis is to obtain the highest possible output power, while the result of time-delay pulse adding is arbitrary waveform combination. Experiments have shown that the outputs of different modules can be overlaid on the time axis. In theory, as long as there are enough modules, sufficient peak values can be obtained, or any output voltage waveform can be pieced together.

This modularization route actually forms a new concept of pulsed power generation. The

traditional method of pulsed power generation is to determine the pulse energy first, and then compress it in time to produce high power. The method of modularized pulsed power generator is to first determine the output of a single module, and then achieve the required output power through overlaying. Meanwhile, the output waveform can also be controlled through the time relationship between modules.

From a technical point of view, modularized pulsed power generator is an effective means to achieve flexible and adjustable pulse parameters.

- Intelligent identification and feedback control

The intelligence of the pulsed power generator may sound unrealistic, but in fact, the self-protection capability of the power supply can be considered one of the lowest levels of intelligent functions. Industrial pulsed power generators have varying degrees of protection functions, which means that when the power supply detects that a certain parameter exceeds the threshold, it will automatically take protective measures to avoid catastrophic damage. However, the intelligence mentioned here places further demands on the self-management ability of the pulsed power generator, which is not limited to simple protection functions but also includes automatic parameter adjustments within a limited range.

Compared to traditional single-output pulsed power, intelligent pulsed power contains two levels. The first is to fully utilize the flexibility of the pulsed power source to generate rich and diverse pulse waveforms. In the traditional sense, high-repetition-frequency pulsed power refers to the repeated output of the same pulse, such as a pulse string that is a simple repetition of the same pulse. However, modular pulsed power generators can now achieve arbitrary changes in output peak and pulse width within a limited range, so a pulse string can consist of multiple

pulses with different voltages and pulse widths. Such pulse strings are very meaningful because some gas discharge applications and research on the biological effects of electric fields require pulse strings with increasing or decreasing amplitudes.

The second level is the pulsed power generator has the ability to understand the circuit information and take some action to respond based on the load information. Traditional pulsed power generators usually release pulse energy to the load according to the designed indicators unilaterally and basically do not have an understanding of the load condition and corresponding response capabilities. However, an ideal industrial pulsed power source should have a certain self-adjustment ability. This point is closely related to the generalization of the above pulsed power source. That is, an ideal intelligent pulsed power generator should have the ability automatically adjust its output parameters as the load changes. For gas discharge loads, for example, there is an optimal value for the voltage peak and pulse width, and this optimal condition can be found by gradually changing the output parameters and analyzing the load waveform. This work is usually done manually, and one of the goals of intelligent pulsed power is to automatically find the optimal load voltage and pulse width.

The premise of intelligent pulsed power includes the hardware output parameter adjustability and software state analysis and judgment capability. The above-mentioned modular pulsed power technology has provided certain technical support in the hardware aspect. With appropriate software improvements, the intelligence of the pulsed power generator can be gradually improved. In recent years, solid-state pulsed power modules have mostly used microcomputers or FPGAs for control, and these chips have varying degrees of external feedback and logic processing capabilities based on feedback signals. Therefore, it can be seen that the software goal of supporting intelligent pulsed power is not difficult to achieve technically.

1.4.2 Issues in Pulsed Gas Discharge Low Temperature Plasma

Plasma is the fourth state of matter, accounting for 99% of the visible matter in the universe, but is less commonly found in the natural world at atmospheric pressure and low temperature. In recent years, with the development of pulsed power technology, various forms of atmospheric pressure low temperature plasmas have been generated by gas discharge, and successfully applied in fields such as environmental protection, biomedicine, material modification, and flow control. Compared to the widely used low-pressure, low-temperature plasmas in modern industry, atmospheric pressure low-temperature plasmas do not require a vacuum chamber, have lower cost, and are more versatile in their applications (such as in clinical treatment). The application of atmospheric pressure gas discharge and its plasmas is an emerging and important interdisciplinary field that demonstrates rich scientific exploration value and broad market application prospects.

This emerging scientific field has made significant breakthroughs in the past 20 years, especially in establishing quantitative/semi-quantitative theoretical systems and control strategies for stability, uniformity, chemical activity, and interaction with matter of atmospheric pressure low-temperature plasmas, promoting the development of theory and applications in multiple interdisciplinary fields.

However, pulsed atmospheric pressure gas discharge differs from traditional Townsend gas discharge, and pulsed atmospheric pressure discharge low-temperature plasmas often involve strong coupling of multiple physical fields and complex chemical processes. Some key scientific and technological issues need to be further studied, such as the chaotic processes of plasmas, development mechanisms of nanosecond pulsed discharges, quantitative diagnosis of active

particles in plasmas, biomedical effects of plasmas, large-volume production of low-temperature plasmas, time-varying impedance issues, and memory effects of residual particles in gas discharge [23].

To promote the application of pulsed atmospheric pressure gas discharge, it is essential to understand the basic physical behavior of pulsed atmospheric pressure discharge.

1.5 Research Main Work

The main work of this article is based on the improvement in performance based on solid-state pulsed power topology and its application, which have included an automatic feedback control system and hardware pulsed power circuit. And then used the solid-state pulsed power system to study the physics of pulsed atmospheric pressure gas discharge. The main structure and work of each chapter are as follows:

- The first chapter explores the pulsed power technology and its applications. It elaborates on typical compact pulsed power circuits that utilize solid-state switches and highlights several typical applications made possible by these generators. Additionally, the chapter introduces some of the challenges inherent in pulsed power applications and outlines the latest trends in the field's development.

- In the second chapter, the main circuit structure and components of SSLTD are introduced. Some typical waveform performance tests and analyses of SSLTD are presented. Finally, to meet the requirement of industrial applications, the further development of SSLTD technology is discussed.

- In the third chapter, the time-varying impedance issues of atmospheric pressure gas discharge have been controlled by using the SSLTD with a automatic feedback control system. This

study shows that our SSLTD feedback control pulsed power generator can see the load behavior of the previous pulse. It can think in order to find out a better output waveform. And it can act by generating this improved waveform, which can change the load behavior.

- In the fourth chapter, a bipolar SSLTD is developed to study the memory effect of the atmospheric pressure gas discharge on the behavior of the following pulse for consecutive operations. Considering applications of atmospheric pressure gas discharge require a repetitive operation, it is always significant to understand the memory effect it can create in the gas that may result in different behavior of the next pulse following it. This research is going to prepare a physical interpretation of this topic by its designed model.

- In the fifth chapter, a conclusion of this article and future work is given.

- The sixth chapter introduces the publication of article, conference participation, and awards during the doctoral period.

CHAPTER II: SOLID-STATE LINEAR TRANSFORME-R DRIVER (SSLTD)

2.1 Traditional Linear Transformer Driver

2.1.1 Inductive Voltage Adder

Initially, LTD pulsed power generator is proposed based on the Inductive Voltage Adder (IVA) pulsed power generation method. It is better for us to understand the IVA circuit before we study the LTD circuit.

The IVA circuit is one mode of modular pulsed power generation. An IVA pulsed power generator consists of n-level modules and a central conductor. Each module is composed of a pulse transmission line and a magnetic core, and each module is connected in series by the central conductor. The voltage adder technique in IVA connects the drive module circuit voltages in series and limits the high voltage to the central conductor, resulting in a higher voltage gradient. When pulses are simultaneously generated by n modules and fed into the load, the output voltage at both ends of the central conductor is n times the voltage of each module [24].

A schematic diagram of a simple 3-level inductive voltage adder system is shown in Figure 2-1[1]. Each drive unit is charged with V volts and connected in series. An inner diameter gradually decreasing metal rod is connected to the drive unit at the left end and passes through three induction cavities. When pulses are generated by each module and simultaneously fed into the load, the output voltage at both ends of the central conductor is three times the voltage of each module.

One advantage of IVA is the quick superposition of voltage between each module through

the transformer principle, which allows the output terminal to reach a relatively high voltage while keeping the voltage of each sub-module relatively low. This simplifies the high voltage insulation between the modules. In theory, if there are enough modules and delay time between them is not considered, an infinitely high output power can be obtained.

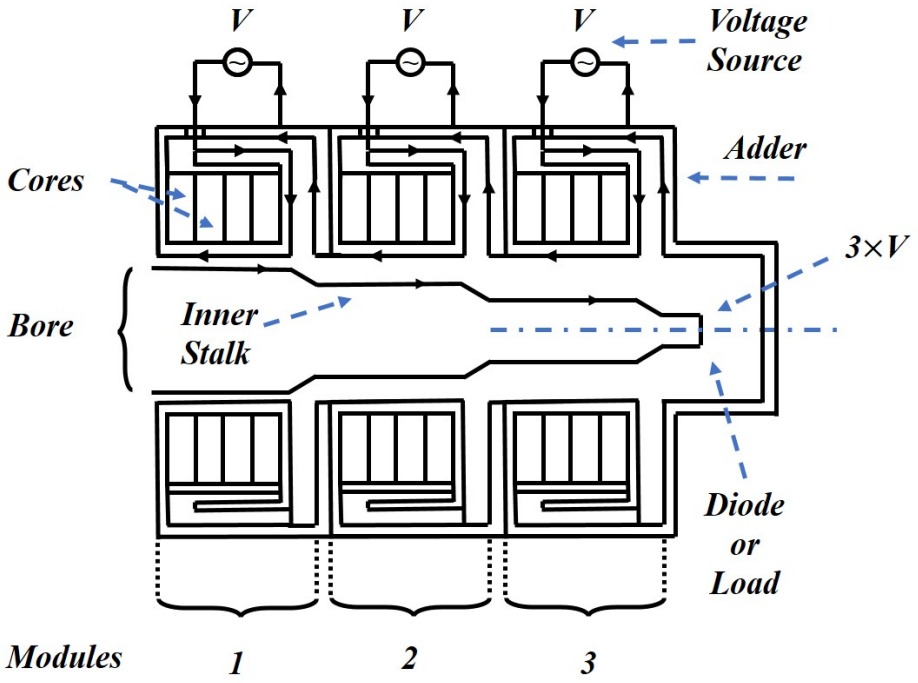

Figure 2-1. Equivalent circuit of the IVA.

Using IVA technology, the world's largest nuclear explosion gamma-ray simulation device, Hermes-III, was constructed at the US Sandia Laboratory (SNL) in 1988. Figure 2-2 illustrates the construction of Hermes III, where Figure 2-2(a) shows the equivalent circuit, and Figure 2-2(b) displays a photograph of Hermes III. Hermes III is a 730-kA, 22-MV, 40-ns pulsed power accelerator that drives an electron beam diode/converter to generate an intense pulse of bremsstrahlung radiation. In the Hermes III pulsed system, eighty individual 1.1-MV, 220-kA pulses are generated and added in groups of four to create twenty 1.1-MV, 730-kA pulses, which are then fed through inductively isolated cavities and added in series by Magnetically Insulated

Transmission Line (MITL). An extension MITL delivers this summed output to the electron beam diode [25].

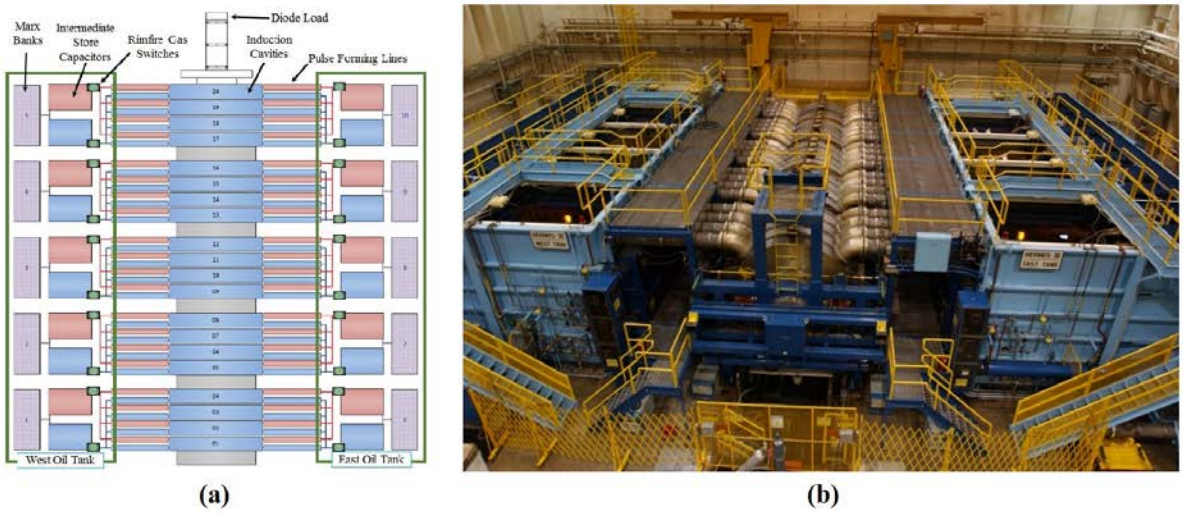

Figure 2-2. Hermes III, (a) equivalent circuit, (b) photograph.

2.1.2 Traditional Linear Transformer Driver

The LTD pulsed power generator was proposed by the Institute of High-current Electronics (IHCE) in Russia in the 1970s, based on the inductive voltage adder (IVA) pulsed power generation method. The main difference between the IVA and LTD circuits is that the IVA transmits the pulses from the external pulsed power generator through PFL and then superimposes the output together, while the LTD has capacitors and switches at each stage to output the voltage independently [26].

The equivalent circuit of the LTD is shown in Figure 2-3. The essentials of the LTD system can be described as that there is a capacitor and a switch consisting of a unit. An LTD module consists of n unit circuits, and LTD systems consist of m LTDs modules. A series connection of the secondary windings of multiple transformers obtains the output voltage of LTD.

LTD, as a module pulsed power system, has the unique ability to generate any desired output voltage waveform by adding together the outputs of multiple unit circuits. Therefore, if sufficient LTD modules are available, it is possible to obtain any suitable voltage waveform. LTD stands out from other pulse compression-based pulsed power systems in that it generates its output voltage by inductively adding together the outputs of multiple modules, eliminating the need for switches to handle the total output power. As a result, there is virtually no limit on the output power of the LTD system. This feature makes LTD a valuable technology for both defense-related and industrial applications. For instance, it can be used to output high enough energy to achieve inertial fusion ignition.

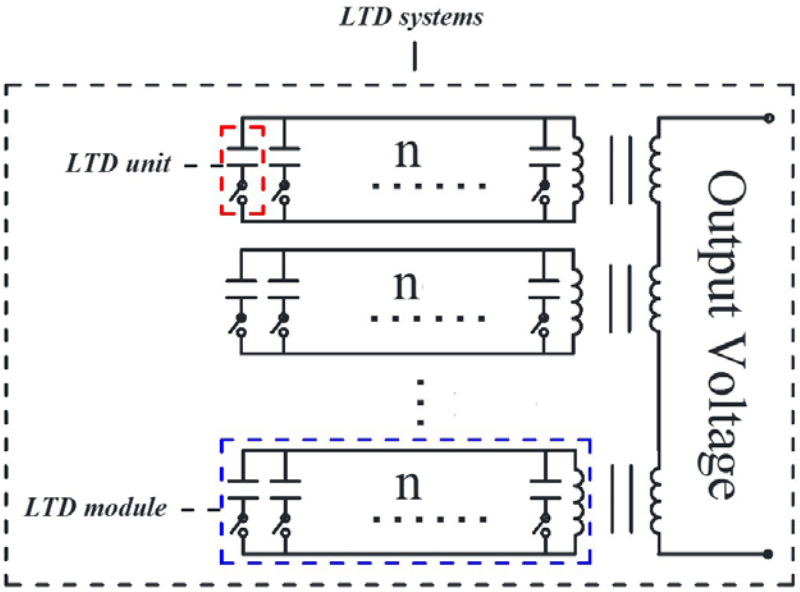

Figure 2-3. Equivalent circuit of the LTD.

Large LTDs originated in the 1970s and are a hallmark of the pulsed power technology developed by the Russian High Current Electronics Institute. In 2004, the largest LTD system in the world was built, called LTDZ, which consists of 40 spark gap switches and 80 capacitors per module with a diameter of 3m, as shown in Figure 2-4. The rise time for LTDZ is 70 ns, and it can produce a current of up to 1MA. This type of LTD was designed for research related to

nuclear fusion.

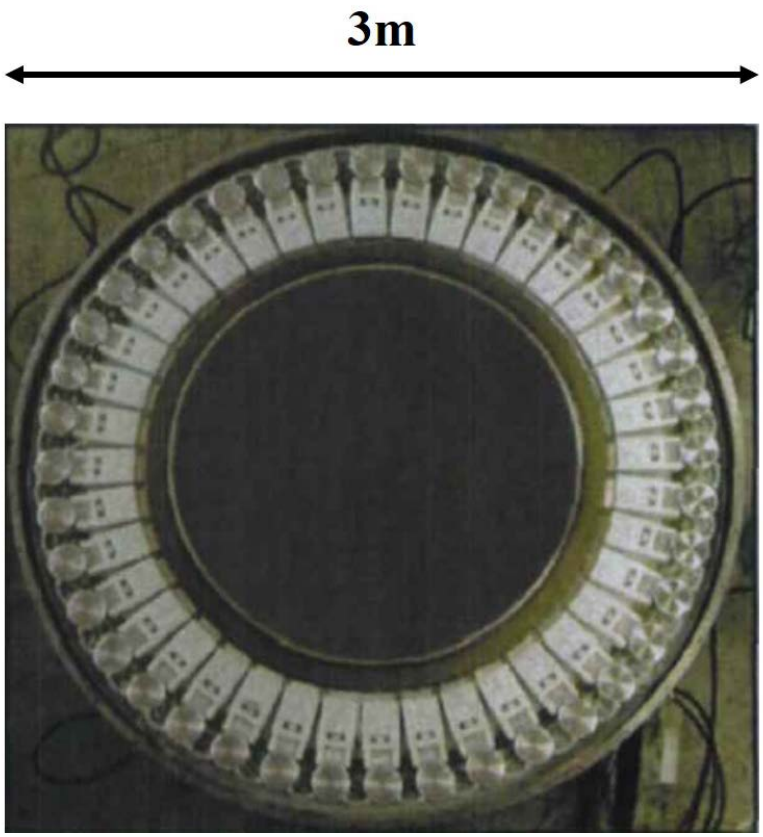

Figure 2-4. The front-side image of an LTDZ module.

2.2 Solid-State Linear Transformer Driver

In the previous section, we introduced the basic concept of traditional large LTDs. However, traditional large LTDs usually use a spark gap switch, which is large in size and cannot be switched on or off controllably. Thus, it is difficult for traditional LTDs to be used in industrial applications.

Over the past decade, the rapid development of semiconductor switch technology, such as IGBT, MOSFET, SiC switches, and others, has significantly advanced the use of pulsed power technology in industrial applications. Compared to traditional gas spark switches, solid-state switches have unique features of controllability, high repetition rates, and long-lasting operation.

Therefore, in order to meet the demands of industrial applications, it is recommended to use solid-state switches in LTD circuits, which can combine the advantages of LTD circuits and solid-state switches.

Compared to the traditional large LTD, LTD using solid-state switch has the following advantages:

- Controllability: Solid-state switches can be turned on and off in a controlled manner, allowing for precise timing and control of the pulsed power output.
- High repetition rate: Solid-state switches have a much higher repetition rate compared to traditional gas spark switches, which makes them more suitable for industrial applications that require frequent pulsing.
- Long-life operation: Solid-state switches have a longer lifespan than traditional gas spark switches, reducing the need for frequent maintenance and replacement.
- Compact size: Solid-state switches are smaller in size than traditional gas spark switches, making them more space-efficient and easier to integrate into industrial systems.
- High efficiency: Solid-state switches have a lower switching loss and higher energy efficiency compared to traditional gas spark switches, which results in less energy wastage and lower operating costs.

Based on previous discussions, LTD using solid-state switches has significant advantages in industrial applications.

In recent years, we have developed LTD topology circuits based on solid-state MOSFET

switches, which we call solid-state linear transformer drivers (SSLTD). The basic principle of SSLTD is the same as that of large LTD, which we introduced in Section 2.1.2, but with solid-state switches. The equivalent circuit of SSLTD is nearly the same as that of traditional large LTD, as shown in Figure 2-3.

In our case, a typical SSLTD module comprises 24 circuit units, 4 protection diodes, and a magnetic core [27-29]. Figure 2-5(a) shows a photograph of one module SSLTD. Each circuit unit contains a powerful solid-state switch and a film capacitor. The protection diodes are connected between the output electrodes and the ground to safeguard the module against external reverse voltage and effectively bypass the circuit current driven by other modules when the solid-state MOSFET switches are turned on or off at different times. The magnetic core functions as a transformer that separates the primary circuits from the secondary and allows all modules to be grounded during operation. It is important to note that, for an ideal magnetic core, the current between the primary and secondary should be nearly the same, and the net current through the unsaturated inductance of the magnetic core can be neglected. Based on this, the circuit behavior in the SSLTD module acts as a 1:1 transformer, effectively coupling the discharge energy of the capacitor to the output. After each pulse, the magnetic flux in the core must be reset; otherwise, the core will quickly saturate in repeated operations. We usually use a 5V 2A DC power source to reset the magnetic core. Table 2-1 lists the main components of the SSLTD module.

The SSLTD PCB board has a cross-sectional illustration shown in Figure 2-6(a). The central yellow ring is the magnetic core, surrounded by capacitors. The MOSFETs are positioned outward from the capacitors, and each switch is connected one-to-one with the driver IC. A conducting film on the bottom surface of each circuit board serves as one of the output electrodes while also providing a top cover for the housing of the neighboring module below it. The output

voltage is induced between the top and bottom coatings of the 1-mm-thick resin board, while a leakage current around the core flows in the housing of the module. To prevent overvoltage damage to the MOSFETs without an additional snubber circuit, diodes are connected across the output gap.

Table 2-1. Major devices in each SSLTD module.

Device	Manufacturer	Model	Specifications	Number per module
MOSFET	IXYS	IXFT6N100F	1000V,6A(DC)	24
Driver IC	MIcrochip	MCP1407	4.5~18V,6A	25
Capacitor	Murata	GRM55DR73A	1kV,100nF	72
Magnetic Core	Sichuan Liyuan Electronics	1K107	130mm(OD)× 5mm	1
Optic receiver	HITACHI	DR9300	DC~50Mb/s	1
Diode	Vishay	UF5408	1000V,3A(DC)	4

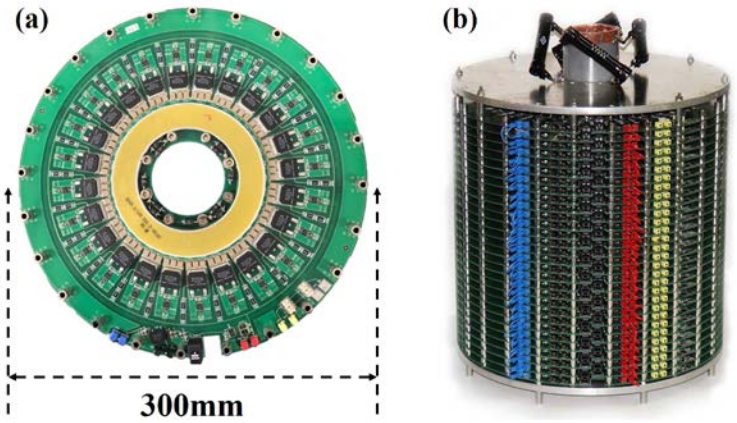

Figure 2-5. The photograph of SSLTD, (a) form view, (b) SSLTD stack with 30 modules.

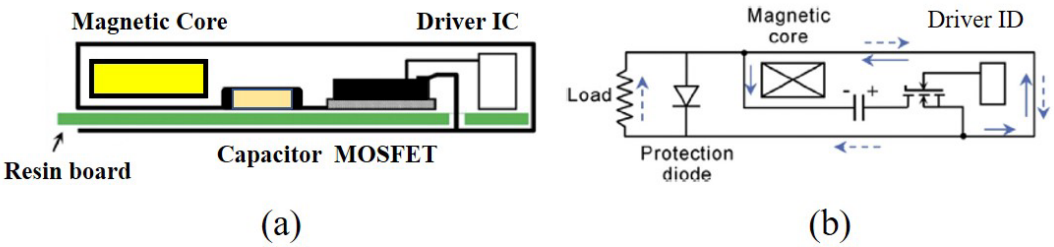

Figure 2-6. The cross-sectional illustration of the SSLTD PCB board.

If there are many SSLTD modules stacked together, the output voltage of each module will add up and output as the whole system output voltage. Thirty SSLTD modules are stacked together, as shown in Figure 2-5(b). The SSLTD stack weighs about 23 kg. And it has a diameter of ~30 cm and a height of~35 cm, which is much more compact than the traditional large LTDZ shown in Figure 2-4. The conductive sheet on the inner surface of the centrally located polyester tube (5 mm thick) is connected to the bottom electrode of the lowest module. This conductive sheet plays the role of a center conductor, bringing the bottom potential to the top. The output can be obtained by using a load to connect the top of the center conductor and the top metal plate.

2.3 Operation Method of SSLTD

Each module in an SSLTD system can be independently controlled, with all control signals delivered via optical fibers. As a result, the SSLTD system can be operated electronically, utilizing tools such as pulse width modulation (PWM) signal generators or field-programmable gate arrays (FPGAs).

2.3.1 SSLTD Operated by Pulse Width Modulation Signal Generator

Traditionally, we use a Pulse Width Modulation (PWM) signal generator to operate the SSLTD system. The control processes are shown in Figure 2-7. The operational principle can be illustrated as follows:

① The PWM control signal is output by the PWM signal generator and sent to the signal converter via fiber optic cable.

② The signal on the converter controls the entire optical transmitter system, with each optic signal controlling each independent SSLTD module.

③ The optical signal is converted back into an electric signal on the SSLTD module and amplified by the driver IC.

④ The electronic signal from the driver IC is sent to the 24 independent driver ICs of the MOSFETs, causing the 24 solid-state MOSFET switches in the module to turn on simultaneously.

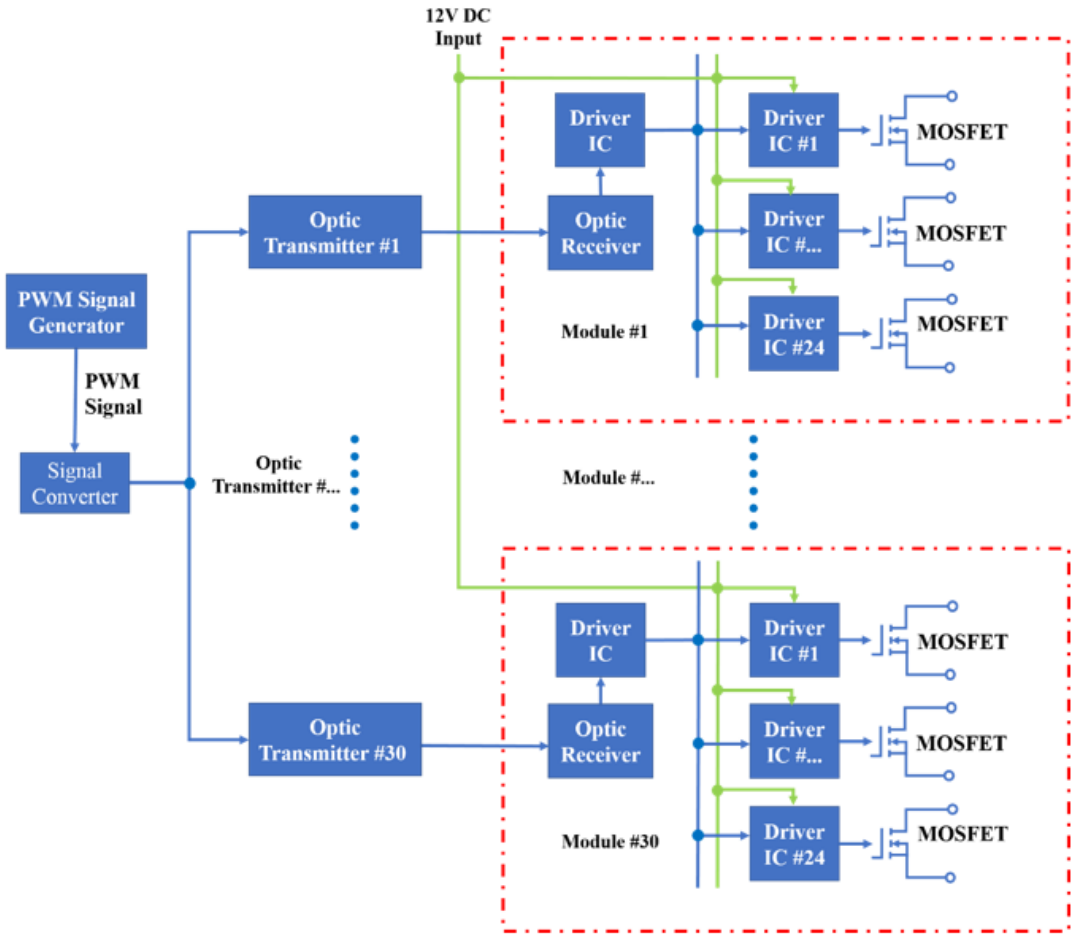

Figure 2-7. SSLTDs are controlled by a signal generator.

Based on the previous control process, the output pulse between the top and bottom modules is simultaneously delivered to the load.

However, one disadvantage of using the PWM signal generator is that the number of output channels is limited, and typically only one channel is used to turn on or off all SSLTD modules. Therefore, it can be challenging to independently turn on or off each SSLTD module at different times, which limits the potential benefits of SSLTD in pulse shaping.

2.3.2 SSLTD Operated by Field-Programmable Gate Array (FPGA)

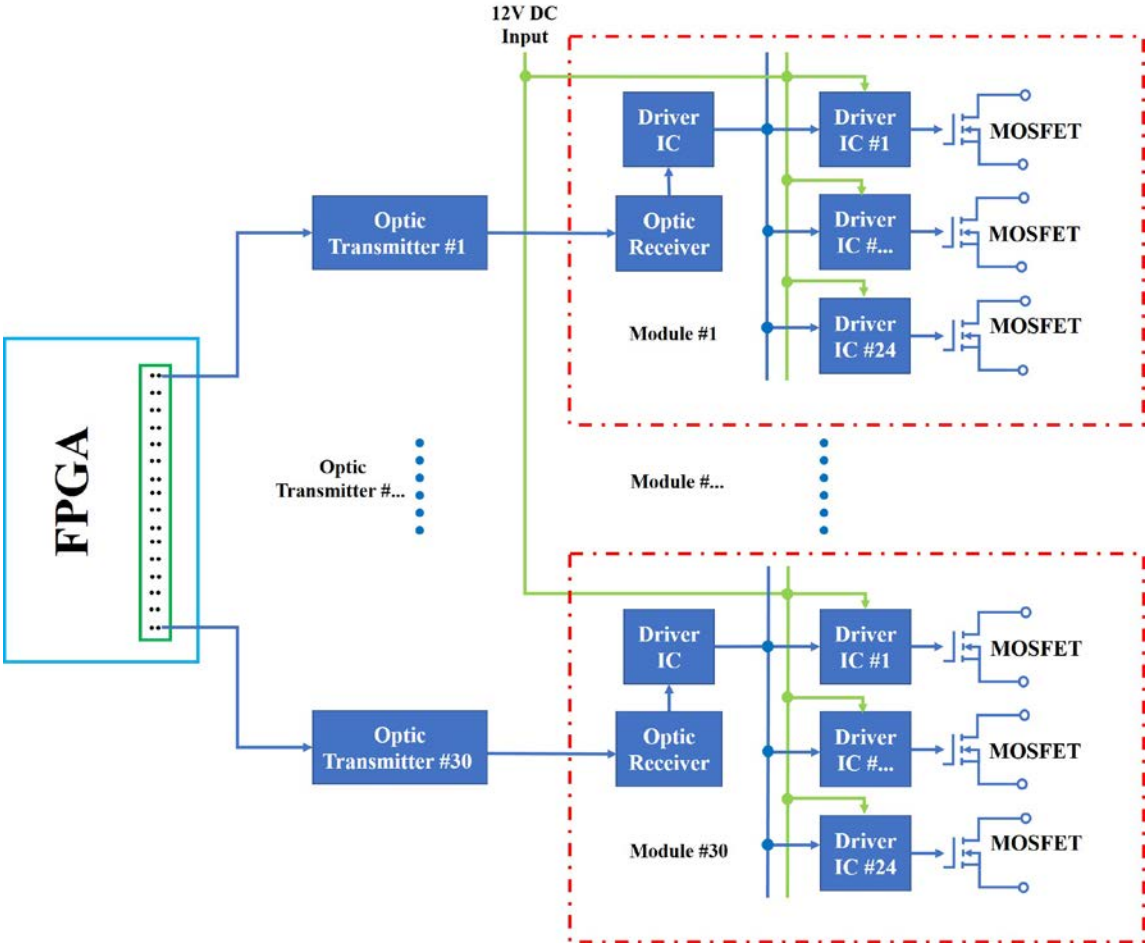

Figure 2-8. SSLTDs are controlled by FPGA.

An FPGA, or field-programmable gate array, is an integrated circuit that can be configured by a customer or designer after manufacturing, making it easily programmable. While a typical FPGA board has many functions, we have utilized it as a multi-channel pulse generator and field-programmable function, making it an ideal device for the signal source of SSLTD. Each FPGA board has many I/O pins, allowing us to assign one pin to each module of our SSLTD, which can be controlled independently by the program preloaded on the FPGA. Figure 2-8 illustrates these control processes, where each module is controlled by one independent signal, unlike in Figure 2-7. We primarily use the Terasic DE0-Nano FPGA, which has 80 I/O independent pins, to

generate the control signal for our SSLTD. Despite the DE0-Nano FPGA's 50 MHz clock, we have utilized the phase-locked loop (PLL) function provided by Altera to boost the clock frequency up to 100 MHz, allowing us to define timings with 10-ns steps using the FPGA control signal. The control processes of SSLTD using FPGA are depicted in Figure 2-8, where each independent control signal controls each SSLTD module, distinguishing it from Figure 2-7. By using the FPGA control method, we have not only demonstrated the flexibility of the output waveform but also its ability to vary from pulse to pulse, as indicated in the following sections.

2.4 Performance Test and Analysis of SSLTD

2.4.1 Performance Test and Analysis of Magnetic Core Used in SSLTD

Table 2-2. Magnetic core information used in the experiment.

Magnetic Core	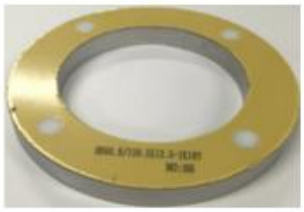		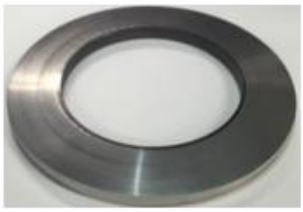
Model	1K107	1K107	FT-3H
Material	Nanocrystalline	Nanocrystalline	FINEMET
Inner diameter(mm)	86.5	86.5	89.1
Outer diameter(mm)	130.5	130.5	133
Thickness(mm)	13.5	6.5	6.5
Cross section(mm^2)	297	143	143
Mean path length in the magnetic core(mm)	341	341	349

The magnetic core is a crucial component of the SSLTD circuit as it functions as a transformer, separating the primary and secondary circuits. The characteristics of the magnetic core significantly impact the output waveform and energy effect of the SSLTD. Therefore, the magnetic core used in the SSLTD must have high saturation flux density, good high-frequency characteristics, and a compact size. Recently, materials such as Fe-Si, Finemet, Metglas, and

other amorphous nanocrystalline have been primarily used for magnetic cores. In this section, we analyze the SSLTD's performance using different magnetic cores, and the magnetic core information used in the experiment is shown in Table 2-2.

2.4.1.1 Hysteresis Loop of Magnetic Core

The hysteresis loop is a crucial parameter of the magnetic core, as it provides important information about the core's behavior. Parameters such as saturation magnetic flux density and coercive force can be determined from the hysteresis loop. For the magnetic core used in the SSLTD, it is important to have a compact size, high saturation magnetic flux density, and low coercive force.

The equivalent circuit used to measure the hysteresis loop is shown in Figure 2-9. Two independent and opposite pulse circuits are used as the primary circuit, and opposite voltage is applied to the magnetic core. The secondary side is left open. The number of turns of the coil on both the primary and secondary sides is one. When S_1 is turned on, the primary side I_1 and the secondary side V_1 are recorded. After the magnetic core is saturated, S_1 is turned off, and S_2 is turned on. Then, the primary side I_2 and the secondary side V_2 are measured. A typical waveform obtained using this method to measure the 1K107 (6.5mm thick) is shown in Figure 2-10. The applied voltage is 100 V, and the frequency is approximately 100 kHz. It should be noted that the first pulse should be ignored, as it is used to confirm that the magnetic core is saturated.

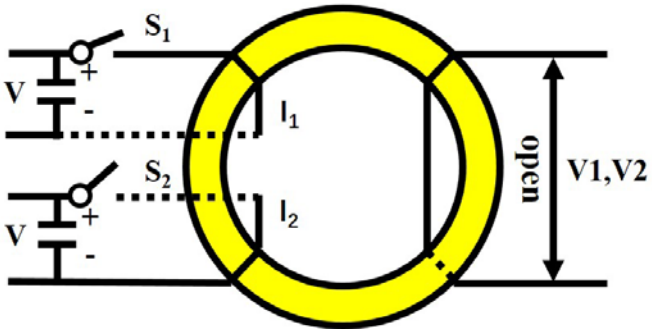

Figure 2-9. Equivalent circuit used to measure the hysteresis loop.

Then, the magnetic flux φ is derived in Equation (2.1) according to Faraday's law, and the magnetic flux density B and magnetic field H are derived using Equations (2.2) and (2.3). N1 is the number of turns of the primary side coil. S is the cross-sectional area of the magnetic core. l is the mean path length of the magnetic core. V and I are the measured voltage and current, respectively. B and H are the magnetic flux density and magnetic field.

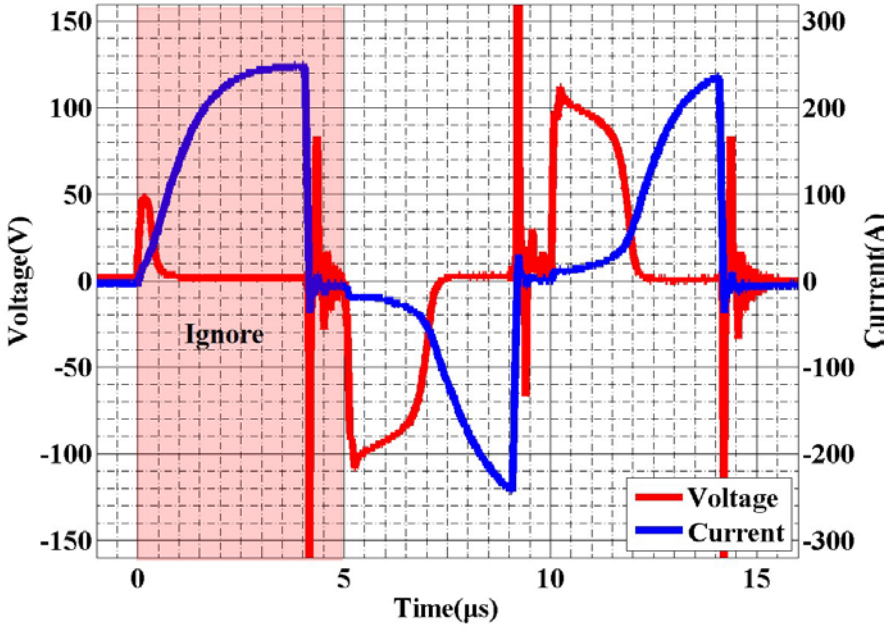

Figure 2-10. Typical voltage and current waveform of the magnetic core.

Table 2-3. Magnetic core characteristic parameters.

Magnetic Core	1K107 (13.5 mm)	1K107 (6.5 mm)	FT-3H (6.5 mm)
Saturation magnetic flux density	0.6	0.6	1
Coercive force	20	50	20

Based on the previous formula, we can obtain the hysteresis loop of the magnetic cores mentioned in Table 2-2. The hysteresis loops are shown in Figure 2-11, and the basic information of the hysteresis loops is presented in Table 2-3. The results indicate that the saturation magnetic flux density of FT-3H is higher than that of 1K107. With the same thickness, the coercive force

of FT-3H is smaller than that of 1K107. For the same material, the saturation magnetic flux density is nearly the same. However, increasing the thickness of the magnetic core is equivalent to increasing the unsaturated inductance, which results in an increase in the coercive force.

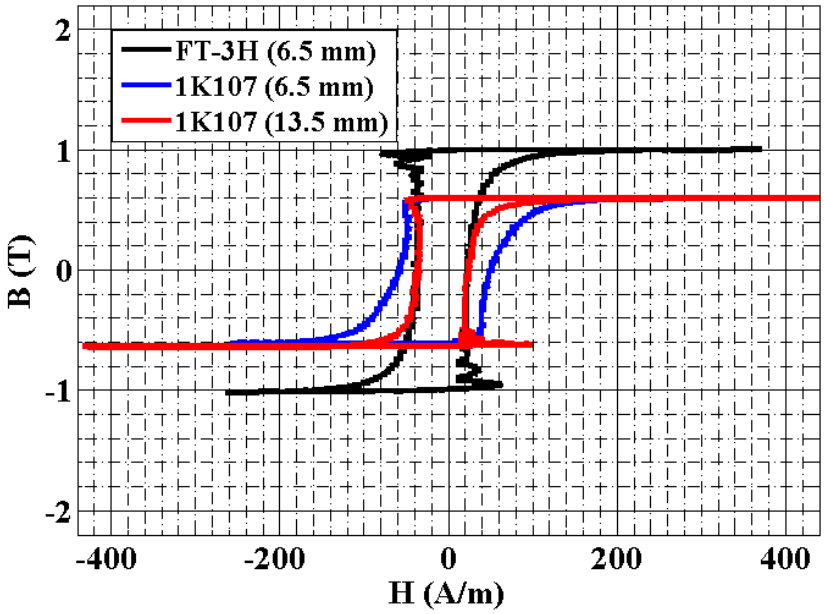

Figure 2-11. Hysteresis loop of the magnetic core.

Based on Equations (2.1) and (2.2), we can understand that the pulse duration of SSLTD is also increased with the B and S increase. As a demonstration experiment, we take one module charge to 600 V and test its maximum output pulse width of different magnetic cores. The results are shown in Figure 2-12. From the experiment result, we can confirm that with the same magnetic core size, FT-3H has a long pulse duration. Since the FT-3H saturation flux density is higher than 1K107. Also, as the same material (1K107), we can increase its cross-sectional area to increase pulse duration. However, it may cause an increase in the volume of SSLTD.

$$\varphi = \frac{1}{N_1}\int V dt \tag{2.1}$$

$$B = \frac{\varphi}{S} \tag{2.2}$$

$$H = N_1 \frac{I}{l_e} \tag{2.3}$$

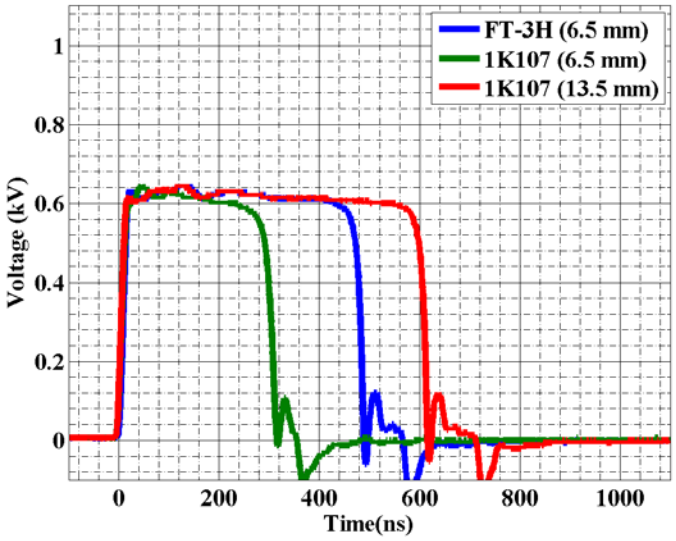

Figure 2-12. Maximum volt-second product of different magnetic cores.

2.4.2 Leakage Current of the Magnetic Cores

Regarding energy loss in the magnetic core, hysteresis loss that occurs in ferromagnetic materials is significant and depends heavily on the geometry and material of the core. For a given magnetic core, the energy loss is determined by the voltage waveform, so it can be seen as a leakage resistor connected in parallel to the load. We call the current flowing through this resistor the leakage current, which is a crucial parameter for SSLTD. The magnetic core used in SSLTD must have a low leakage current to minimize energy loss and ensure high energy efficiency.

In this section, we analyze the leakage current of different magnetic cores in one module SSLTD. This is important because hysteresis loss, which depends on the material and geometry of the core, occurs in ferromagnetic cores and can be modeled as a leakage resistor connected parallel to the load.

The experiment conditions are listed as follows: the charge voltage is 600 V, the pulse width

is 200 ns, the operating frequency is 1 kHz, and the load resistor is 40 Ω. The leakage current can be evaluated by calculating the difference between the primary and secondary side currents.

The leakage currents of different magnetic cores are shown in Figure 2-13. It is worth noting that the magnetic core of 1K107(20 mm) is connected in series with 1K107(6.5 mm) and 1K107(13.5 mm). From the results, we can understand that for a given material (1K107), the leakage current decreases as the thickness of the magnetic core increases. For a given thickness (6.5 mm), the leakage current of FT-3H is significantly lower than that of 1K107. The leakage current of FT-3H (6.5 mm) and 1K107 (13.5 mm) is nearly the same. The increase in leakage current indicates an increase in energy loss in the magnetic core. Thus, in principle, we can conclude that, based on the previous experimental conditions, the energy efficiency of SSLTD using FT-3H and 1K107(13.5 mm) magnetic cores is nearly the same. However, the lowest energy efficiency is obtained using 1K107 (6.5 mm). The detailed energy efficiency of SSLTD using FT-3H (6.5 mm), 1K107(6.5 mm), and 1K107(13.5 mm) magnetic cores is 93%, 42%, and 95%, respectively.

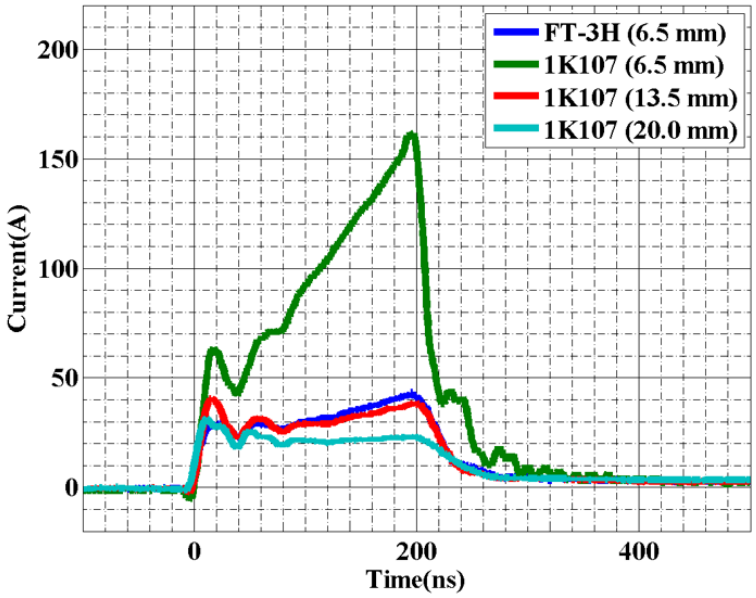

Figure 2-13. Leakage current of the magnetic core.

Based on the previous discussion, with the same thickness, compared with 1K107 (6.5 mm), FT-3H (6.5 mm) has better saturation magnetic flux density and lower leakage current. Hence, replacing the magnetic core from 1K107 to FT-3H can make the SSLTD smaller in size and increase energy efficiency.

2.4.3 Performance Test and Analysis of the Output Waveform of SSLTD

The SSLTD pulsed-power system has several advantages over traditional MPC methods. First, it offers greater flexibility in the output waveform variation. By adjusting the width and delay of each small pulse, we can shape the output waveform according to our requirements. Second, the SSLTD system allows for scalability and modularity. Each small pulse is generated by an independent module, and by adding more modules, we can increase the output power. This makes it easier to adapt the system to different applications and power requirements. Finally, the SSLTD system has a higher energy efficiency compared to traditional MPC methods. By using high-frequency switching and resonant circuits, we can reduce energy losses in the system and achieve higher energy efficiency.

Overall, the SSLTD pulsed-power system represents a new and promising approach to pulsed-power generation, offering greater flexibility, scalability, and energy efficiency compared to traditional methods.

2.4.3.1 Pulsed Adding and Shaping by Using SSLTD Stacked

Typical output voltage waveforms obtained by using the SSLTD stacked with 28 modules are shown in Figure 2-14, where each module is charged 800 V. Figure 2-14(a) shows the output waveforms obtained with different numbers of modules, which have been increased from 2 to 28 only through FPGA synchronize control without changing the hardware assembly. The peak voltage increases from ~1.6 to ~23kV, confirming the voltage multiplication by inductive voltage

adding. Figure 2-14(b) shows the output waveforms of 28 modules obtained with different pulse widths, ranging from 30 to 200 ns by FPGA control signal. The experiment result shows that the SSLTD system cannot output the full waveform when the control signal is less than 50 ns. This phenomenon may be caused by the control signal being less than the rise time of the SSLTD system. When the gate signal is varied from 50 to 200 ns, the full width at half-maximum of the output pulse increases from ~50 to ~200 ns, indicating that the output pulse width can be continuously varied by changing the pulse length of the control signal. However, the maximum variation of the pulse width is limited within a certain range due to the saturation of the magnetic flux in each SSLTD module, which limits the pulse length. In principle, we can extend the pulse width by decreasing the charge voltage of each module or by increasing the size of the magnetic core. Figure 2-14(c) shows the maximum pulse width based on different charge voltages without changing the magnetic core. As a result, the pulse width decreases as the charge voltage increases.

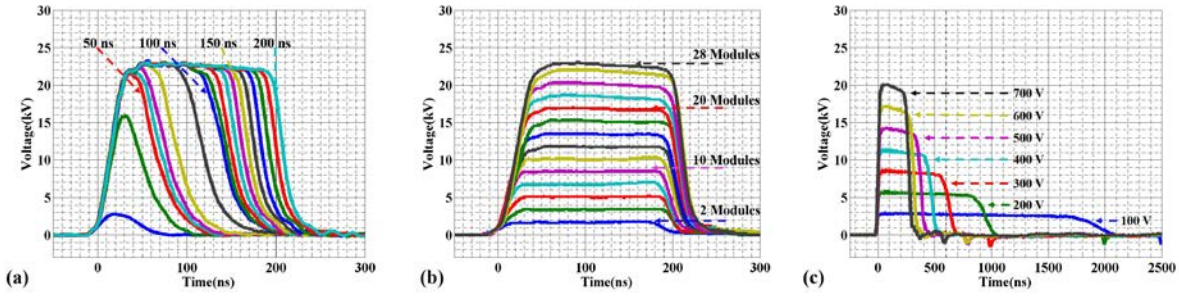

Figure 2-14. Typical output waveform (a) different pulse width, (b) different modules, and (c) maximum pulse width under different charging voltage conditions.

2.4.3.2 Pulsed Shaping by Using Solid-State Linear Transformer Driver Stacked

A demonstration of pulse shaping obtained by sending different control signals to different modules at different timings is shown in Figure 2-15. Figure 2-15(a) shows the operating number at different timing. During ~ 80 ns, 18 modules SSLTD were turned on, causing a voltage increase. During 80 ~ 150 ns, 6 modules were turned off, leading the output voltage waveform

to drop. After 150 ns, 6 modules were turned on again, increasing the voltage waveform. Figure 2-15(b) shows the voltage waveform obtained by the SSLTD based on the control signals.

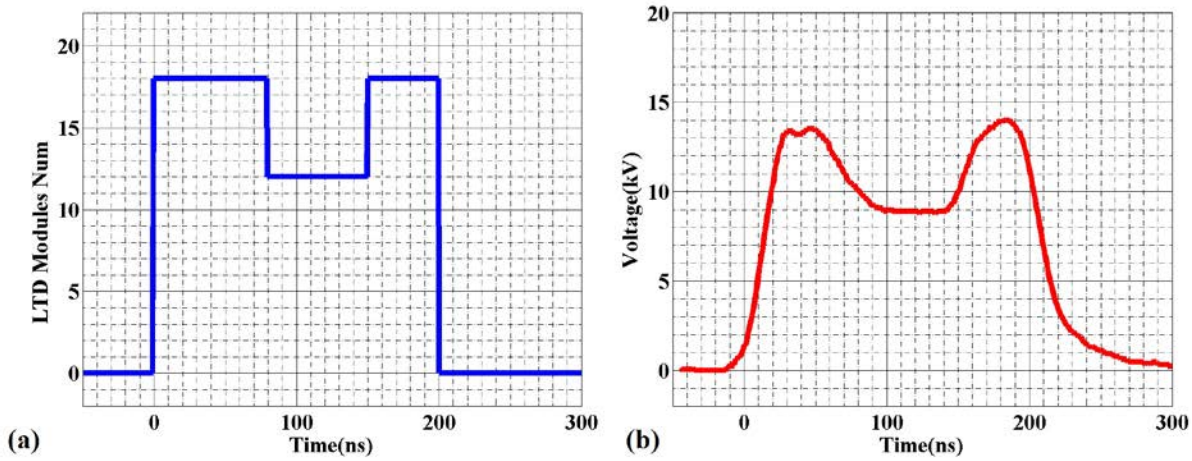

Figure 2-15. Pulse shaping using SSLTD,(a) SSLTD modules number, (b) output waveform.

The SSLTD has an essential feature where it is not required to switch on all the modules as circuit current can still pass through the ones that are not turned on. As a result, the output voltage at any given time is proportional to the number of modules that are on at that moment. This fact opens up the possibility for pulse shaping using different combinations of control signals.

The pulse shaping experiment indicated that, with appropriate control signals, we could theoretically obtain any reasonable pulse output waveform. Such flexible waveforms are of great significance for the scientific community and industry field, such as biological applications of pulsed power, environmental treatment, and atmospheric pressure gas discharge.

2.5 Further Development of Solid-State Linear Transformer Driver

The article will continue to focus on the development of SSLTD technology to meet the requirements of industrial applications. The research in this article can be broadly classified into two aspects: feedback control and bipolar circuit configuration.

2.5.1 Feedback Control of Solid-State Linear Transformer Driver

The feedback control technology of SSLTD is still at the beginning of exploration. The ideal feedback function is that the SSLTD pulsed power generator can **SEE** the load behavior of the previous pulse. It can **THINK** in order to find out a better output waveform. And it can **ACT** by generating this improved waveform, which can change the load behavior.

It covers a wide range of challenges in sense response technology, intelligent control chip, and pulse shaping.To achieve the sense response ability, the response equipments, such as current probes, voltage probes, and so on are necessary. As for the intelligent control chip, FPGA is an idea device to control the solid-state modular pulsed power generator. The pulse shaping feature is easy to achieve with our SSLTD. As we have indicated in Section 2.4.3.2, each module of our SSLTD system can be switched on or off independently, all controlled signals are delivered through optical fibers, and FPGA can carry out all the SSLTD modules control.

In principle, the feedback control system with an appropriate sensor, FPGA and SSLTD system allows us to build a close communication loop from the pulsed power source to the load and back from the load to the pulsed power source, as shown in Figure 2-16. When this link is established, we can build a fully self-controlled pulsed power generator.

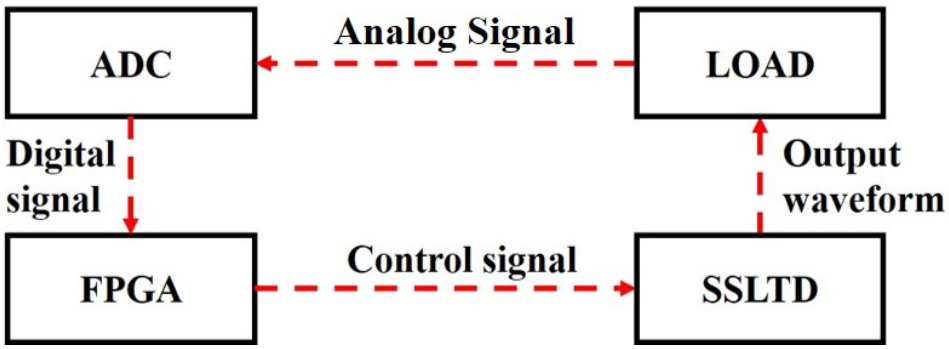

Figure 2-16. The feedback loop of SSLTD pulsed power generator.

An intelligent feedback control pulsed power generator system is significant for industrial

applications as it enables the feedback control system to read the load behavior and analyze its performance to generate a better output waveform based on a specific user scenario. In CHAPTER III, we demonstrate a typical application of the feedback control system through a case study of impedance control of atmospheric pressure gas discharge.

2.5.2 Bipolar Circuit Configuration of Solid-State Linear Transformer Driver

There are many applications that require bipolar high-voltage pulses, such as atmospheric pressure gas discharge and biological applications. Recently, many Bipolar-Marx circuits have been investigated. The Bipolar SSLTD circuit configuration is an exciting direction due to its flexible features. Considering that SSLTD allows us independent control and output of different modules, it could provide a relatively easy technical approach to bipolar output from a single stack. In this article, we propose a new method for generating bipolar waveforms using SSLTD. A bipolar SSLTD can be formed by connecting unipolar modules with opposite directions in series. The critical point of our bipolar SSLTD is allowing reverse current to flow through the modules when they are not outputting. In CHAPTER IV, we demonstrate a typical application of the bipolar SSLTD through a case study of the memory effect of atmospheric pressure gas discharge.

2.6 Conclusion

In this chapter, we have introduced the SSLTD from various perspectives, including its equivalent circuit, external configuration, and working principle. Compared to traditional large LTDs, SSLTD offers advantages in terms of compactness, high-repetition-frequency operation, and operational flexibility. We also analyzed the advantages and disadvantages of traditional PWM control and FPGA control for LTDs. Under the control of FPGA, SSLTD can output typical pulse adding and pulse shaping waveforms, and we also analyzed the influence of

magnetic core parameters on SSLTD's output. Finally, based on the characteristics of SSLTD, we highlighted the potential future development directions for this technology.

CHAPTER III: DISCHARGE IMPEDANCE CONTROL USING SOLID-STATE LINEAR TRANSFORMER DRIVER

3.1 Overview

Atmospheric pressure gas discharge has been shown to have more significant advantages compared to traditional plasma generation methods. The cold plasma generated through this method has potential applications in water treatment, gas treatment, and sterilization [30-31]. As an example, non-thermal plasma shows promise in cracking abundant but low-quality heavy oil into value-added chemicals due to its wide feedstock adaptability and high conversion rate, as illustrated in Figure 3-1 [32]

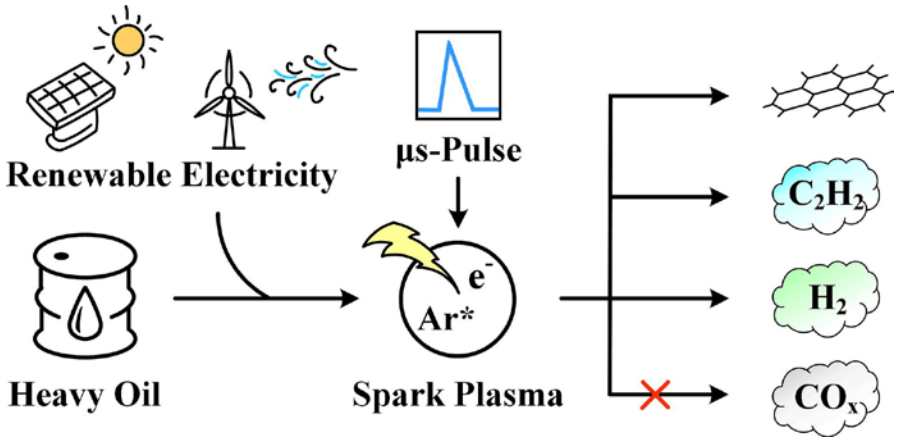

Figure 3-1. Illustration of heavy oil cracking using low-temperature plasma.

However, the generation of cold plasma using atmospheric pressure gas discharge is usually accompanied by a phenomenon of constant voltage but varying current. This can be attributed to the time-varying load impedance of the discharge load, resulting from the rapid plasma development between the electrodes [33-38]. Figure 3-2 illustrates a typical discharge waveform using a discharge tube, with (a) showing the voltage and current waveform, and (b) showing the corresponding impedance waveform. Experimental results demonstrate that the current

significantly drops while the impedance rises after 100 ns, even when the applied voltage remains constant. In the case of atmospheric pressure gas discharge load, the current is highly sensitive to the voltage, and the relationship is non-linear. For instance, a slight increase in the applied voltage may result in a significant increase in the current, leading to an impedance drop, while a slight decrease in the voltage may result in a significant decrease in the current, leading to an impedance rise.

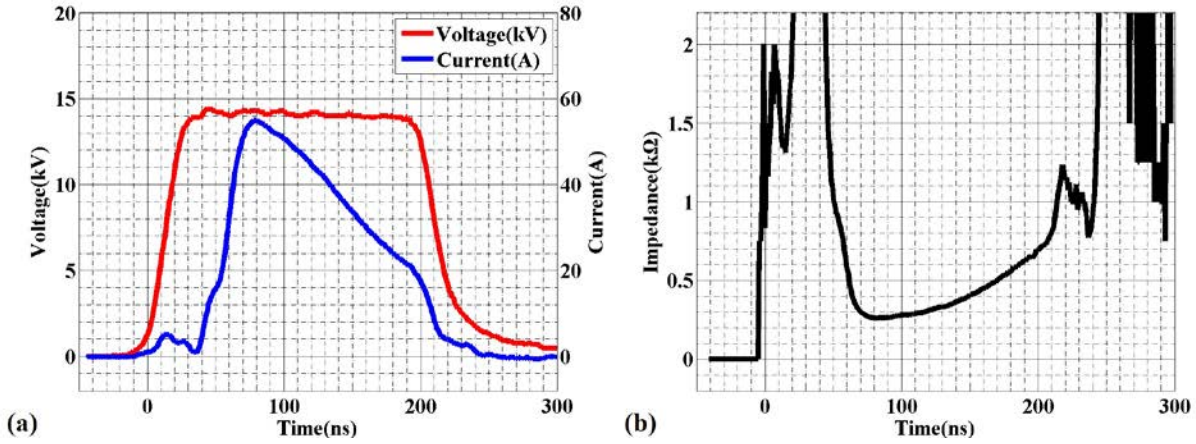

Figure 3-2. Discharge waveform, (a) voltage, and current, (b) impedance.

Therefore, we can say that an appropriate voltage waveform can bring us desirable load impedance behavior, as shown in Figure 3-3. In other words, if we need to control the impedance behavior of the discharge load, the voltage waveform becomes very important.

The main challenge is how to generate an appropriate pulsed waveform. As discussed in CHAPTER II, the SSLTD is a pulsed power generator consisting of multiple modules that can be independently controlled. By adding up the output waveforms of all modules, we can create an arbitrary voltage waveform, provided that we use a sufficient number of modules. Thus, the SSLTD is an ideal modular pulsed power generator for maintaining the desired impedance behavior in atmospheric pressure gas discharge. Essentially, the SSLTD system enables us to control the impedance behavior of the discharge load.

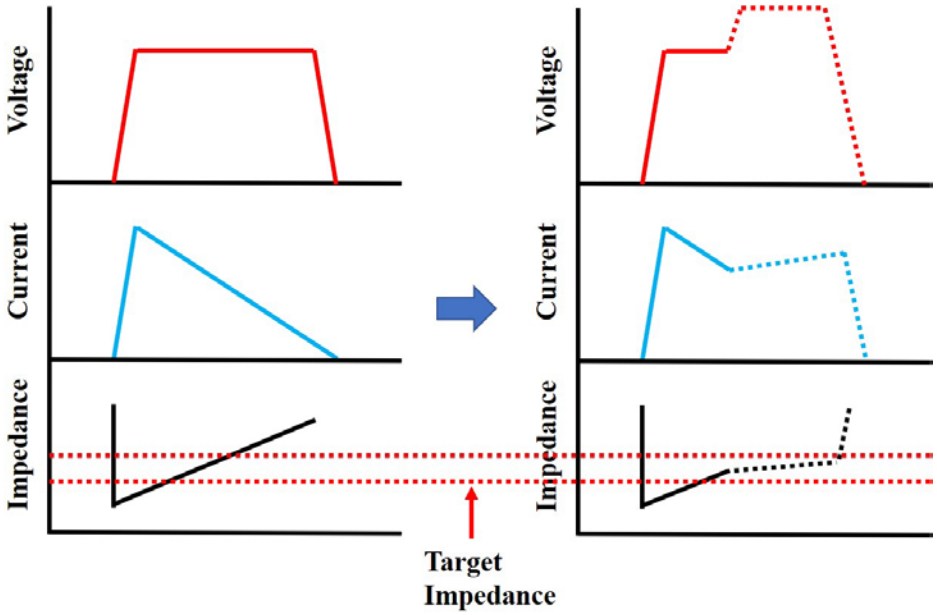

Figure 3-3. A schematic diagram illustrating the adjustment of impedance by modifying the pulse waveform.

3.2 Atmospheric Pressure Gas Discharge Impedance Driven by SSLTD

To illustrate the non-linear relation phenomenon mentioned in Section 3.1, we conducted some demonstration experiments on atmospheric pressure gas discharge driven by SSLTD. Using the SSLTD system introduced in CHAPTER II, we powered an atmospheric pressure gas discharge tube as shown in Figure 3-4(a), with a 20 mm diameter and a 1 mm copper wire at its center. A photograph of our discharge tube is shown in Figure 3-4(b).

Figure 3-5 presents typical experimental waveforms obtained using our SSLTD and discharge tube. The initial experiment is shown in Figure 3-5(a1), where the SSLTD output voltage is around 14 kV and the pulse width is around 200 ns. At 100 ns, the discharge current reaches 55 A and then decreases slowly. As shown in Figure 3-5(a2), the impedance increases from 300 Ω to 700 Ω between 80 ns and 210 ns. However, when we decrease the voltage from 14 kV to 10 kV after 60 ns, the current drops significantly, causing the impedance to rise significantly, as shown in Figure 3-5(b). In principle, we can increase the voltage waveform when

the discharge current drops, leading to a decrease in impedance and a rise in discharge current, as shown in Figure 3-5(c). Compared with Figure 3-5(b), Figure 3-5(c) shows an increasing current between 150 ns and 210 ns and a corresponding decrease in impedance.

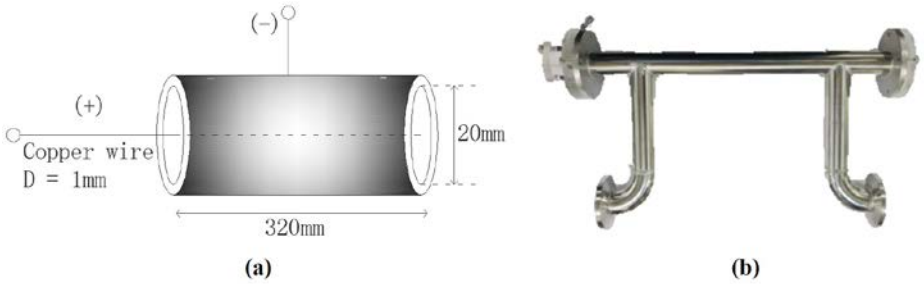

Figure 3-4. Discharge tube model, (a) equivalent circuit, (b) photograph.

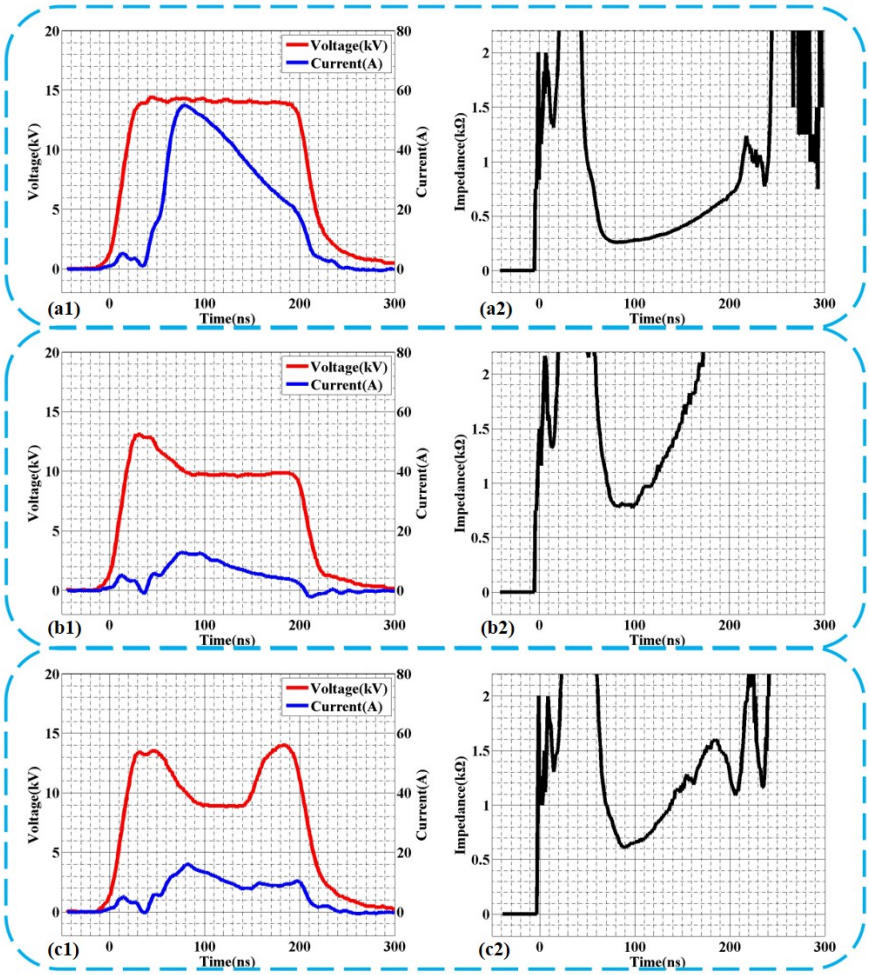

Figure 3-5. Experiment with different discharge waveforms of SSLTD on discharge tubes.

Based on the experimental results shown in Figure 3-5, we can adjust the current and impedance values in the discharge load by changing the voltage waveform during the same pulse. Therefore, if we can provide a suitable voltage waveform, we can arbitrarily control the current and impedance behavior in the discharge load.

3.2.1 The Scenario of the Impedance Control

The experiments shown in the previous section have indicated that the pulse waveform may control the impedance behavior of gas discharge. And taking advantage of the SSLTD in waveform flexibility, we can expect to find a proper pulse waveform to bring us desirable load impedance behavior.

However, it is difficult to find the best waveform from theoretical calculations or numerical simulations because neither of them can accurately represent the real experimental situation. We believe that the best way to do waveform optimization is through experimental try-and-error for a system with good reproducibility in repetitive operation.

As for the atmospheric pressure gas discharge experiment, there are some fundamental assumptions for this operation we need to illustrate.

- The load impedance can be decreased at any time by increasing the voltage.
- The load impedance can be increased at any time by decreasing the voltage.
- The load impedance is not affected by the voltage waveform after this time of the same pulse.

Based on previous fundamental assumptions, the impedance control using the SSLTD experiment scenario is described below.

For repetitive operation, we move along the time axis one step at a time for the entire pulse.

At any time, we start with a low voltage to determine whether the impedance is too high or too low and make adjustments accordingly until we find the appropriate value, then move to the next step. For example, if the impedance is too high, we can increase the voltage to bring it into the target range, as shown in Figure 3-6(a). The red dotted lines indicate the desired impedance interval. As previously mentioned, the load impedance at any time is not affected by the voltage waveform after that time in the same pulse. Therefore, we can use the previous waveform to analyze the impedance at the following timing step, as shown in Figure 3-6(b). If the impedance is too low, we can decrease the voltage to increase the impedance. Since the voltage at any time does not affect the load behavior before that time in the pulse, we can find the desired voltage waveform after firing a certain number of shots at the load by the end of the pulse, as shown in Figure 3-6(c) and Figure 3-6(d).

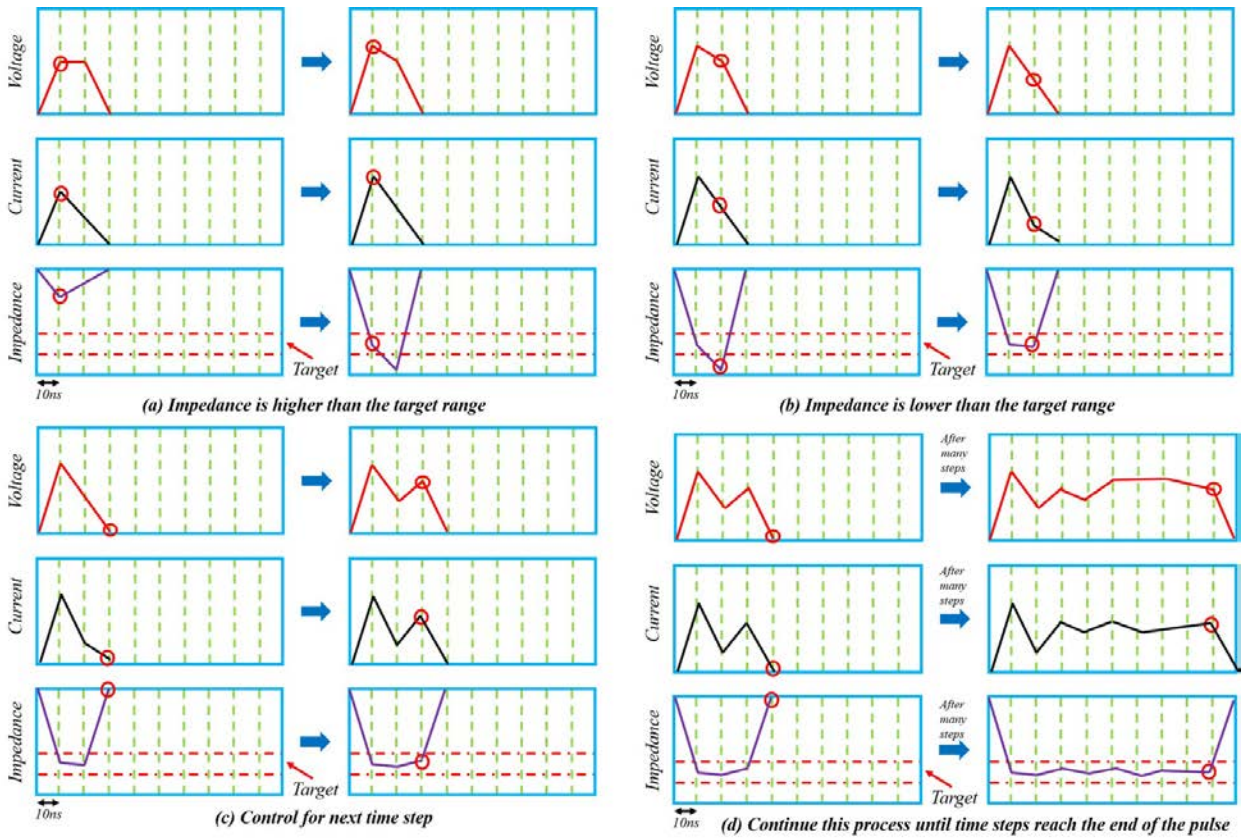

Figure 3-6. The scenario of the feedback control process.

As we have previously experienced in our experiments on atmospheric pressure gas discharge, adjusting load behavior through visual inspection and manual control, particularly current control, can be a straightforward task. However, achieving the desired impedance control can be more complex and time-consuming. In this chapter, we introduce a new approach for automatically controlling SLTD behavior to optimize waveform selection through feedback control, based on the concept presented in Section 2.5.1.

3.2.2 The Feedback Control Scenario of the Impedance Control

In the previous section, we introduced the control scenario of the impedance by manual operation. However, the main problem with the manual operation scenario is that the voltage and impedance relationship is not linear. And it is hard to find the appropriate pulse waveform to control impedance behavior. In this section, we are going to introduce the feedback scenario to automatically control the behavior of SLTD to find the best waveform for the load.

Our feedback control scenario consists of components such as the FPGA, analog-to-digital converters (ADCs), sensors, and SSLTD system. The most common use of an analog-to-digital converter is to convert voltage or current from the sensor into parallel binary digital quantities. It is often utilized as an input channel of a process control system, which is connected to a controller such as FPGA to achieve automatic control of the production process. This system is commonly referred to as a feedback control system.

The basic control flow is shown in Figure 3-7. Since the pulse duration of our SSLTD is very short, and there is no time to react during the pulse, we have to carry out waveform adjustments based on the previous pulse. What we are doing here is that for each shot, we collect the voltage and current waveforms from the discharge load and send them to two ADCs. The FPGA analyzes the digital information from the ADCs and prepares a new waveform for the next

shot. This process is repeated for every pulse.

The flowchart of the feedback control algorithm is shown in Figure 3-8, which provides an example of load impedance management. Initially, the required inputs to the FPGA program are set, including the repeat frequency, the total FWHM of the FPGA control signal, the maximum and minimum number of SSLTD modules that can be used in the SSLTD system, and the target impedance Z(t). The FWHM of the FPGA control signal is divided into several timing steps, each with a duration of 10 ns (i = 10 ns, 20 ns, etc.). In Figure 3-8, (i, j) indicates that j modules are active at i ns, where active means that all switches on the module are turned on.

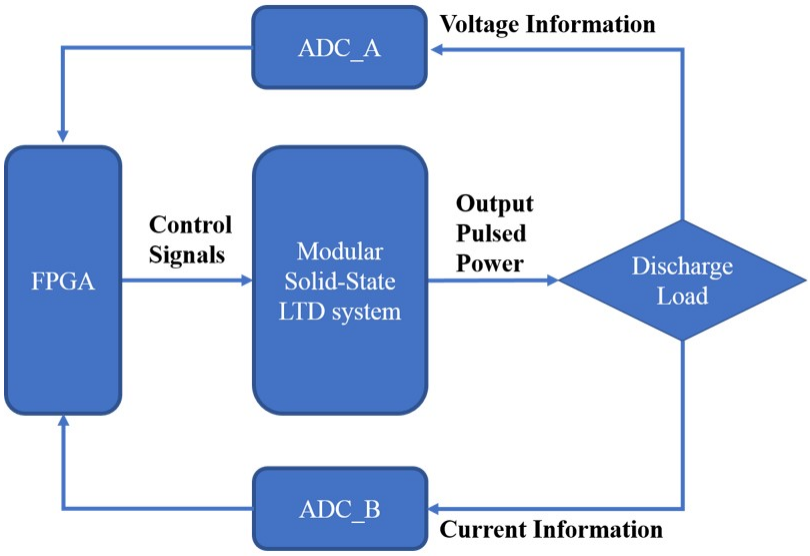

Figure 3-7. The flow of load information and the control signal.

For each timing step, the feedback information, such as voltage information and current information, is collected by the sensor. Since this feedback information is analog, the ADC turns those analog signals into digital and sends them to the FPGA. The FPGA calculates the impedance of this time step. If the impedance Z(i) calculated by the feedback information is higher than the target Z(t), the FPGA generates control signals so that the number of active modules is increased by 1 (j = j + 1) at this particular timing for the next pulse. On the contrary,

if the impedance is lower than the target value [Z(i) < Z(t)], the FPGA will reduce the number of active modules at this timing for the next pulse. Only when the impedance meets our requirement, [Z(i) ≈ Z(t)], the FPGA remembers the module number [Record(i, j)] of this time step and moves on to the next step. This process is repeated until the end of the pulse is reached.

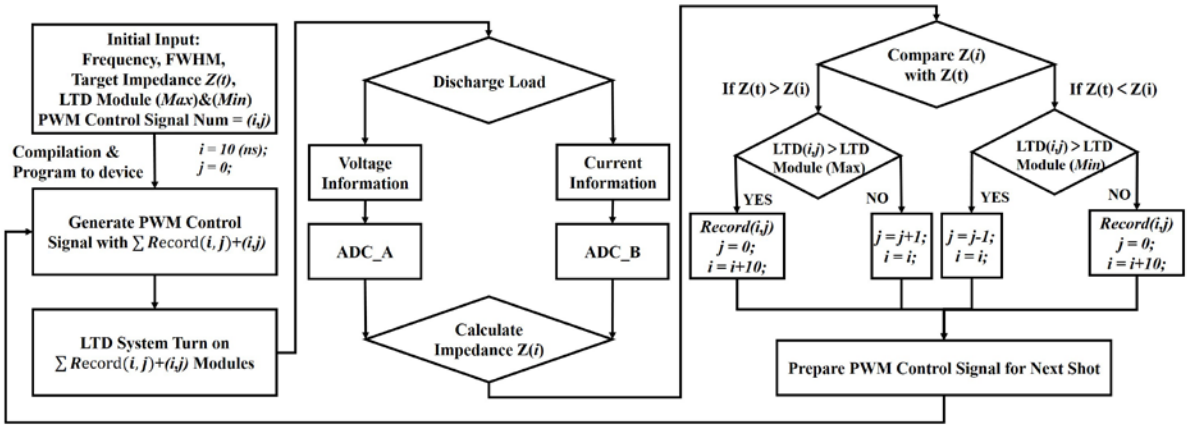

Figure 3-8. Flowchart of the feedback control algorithm.

3.2.3 Feedback Control Experiment Apparatus

The experimental setup of the feedback control system is illustrated in Figure 3-9. The experimental setup includes the SSLTD system with 28 modules to generate the output waveform, a homemade 2-A current source to reset the magnetic core in the SSLTD, a metal box to shield the ADC-SoC FPGA from noise, a Terasic ADC-SoC FPGA to collect and analyze feedback information, and an oscilloscope (Teledyne LeCroy WaveSurfer 3024z) to display and record the output waveforms. To measure the output voltage waveform of the SSLTD, a high-voltage probe (PMK PHV4002) is used, while three Pearson 6595 current probes are used to measure the load current. The first current probe is used to measure the current of the resistor in parallel with the discharge tube, and the current information is sent to the ADC to calculate the applied voltage. The other two current probes are used to measure the discharge current, which can be

recorded by the ADC and the oscilloscope.

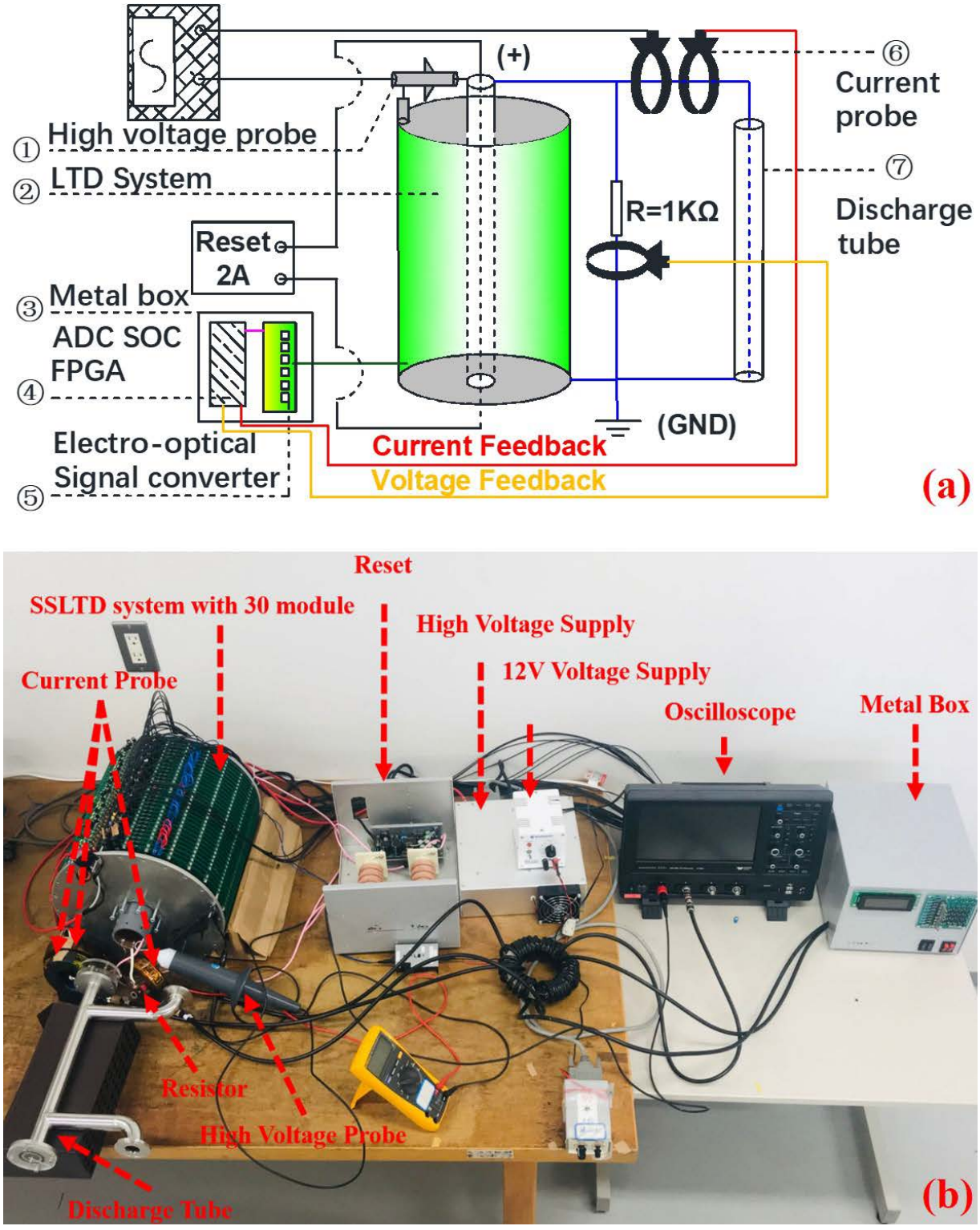

Figure 3-9. Experiment apparatus, (a) equivalent circuit, (b) photograph.

The key points here are that the SSLTD is very flexible in waveform variation and that it is controlled by an FPGA allowing pulse-to-pulse output control. The method we have used to control our LTD system is a feedback scenario. Since the pulse width is too short, and there is no time to react during the pulse, we have carried out waveform adjustment based on the previous pulse. So, after several trial pulses, we are expecting to arrive at an optimized voltage waveform. What we are doing here is that, for each shot, we collect the voltage and current information from the load and send them to ADCs, analog-to-digital converters. The FPGA analyzes the digitized information and find out a new waveform for the next shot. And it is done fully automatically based on a predetermined algorithm.

3.2.4 Proofreading ADC Input and Output Value

The ADC-SoC development kit provides a powerful hardware design platform based on the Intel System-on-Chip (SoC) FPGA [39]. This platform combines the latest dual-core Cortex-A9 embedded core with industry-leading programmable logic to achieve ultimate design flexibility. We can utilize powerful reconfigurable features with high-performance, low-power processor systems. Some photographs of the ADC-SOC FPGA are shown in Figure 3-10, which describe the layout of the board and indicate the location of connectors and critical components.

There are many parts in this ADC-SOC FPGA for many different usage purposes, but the main components that are important to us are the following:

- Clock with 50MHz from the clock generator.
- 40-pin expansion header.
- High-Speed Analog to digital conversion (ADC)

- Two channels
- 14-bit resolution
- Up to 150MSPS (Mega Samples per Second)

It is worth mentioning that even though the clock of ADC-SoC FPGA is 50 MHz, we have used the phase-locked loop (PLL) function provided by Altera to boost the clock frequency up to 100 MHz. Thus, the FPGA control signal allows us to define the timings with 10-ns steps. In addition, the sample rate of the ADC can be increased to 100 MSPS.

Before using the ADC to measure the load information, we need to proofread the proportional relationship between the analog and digital signals in the discharge load. This is a significant step for our feedback control scenario.

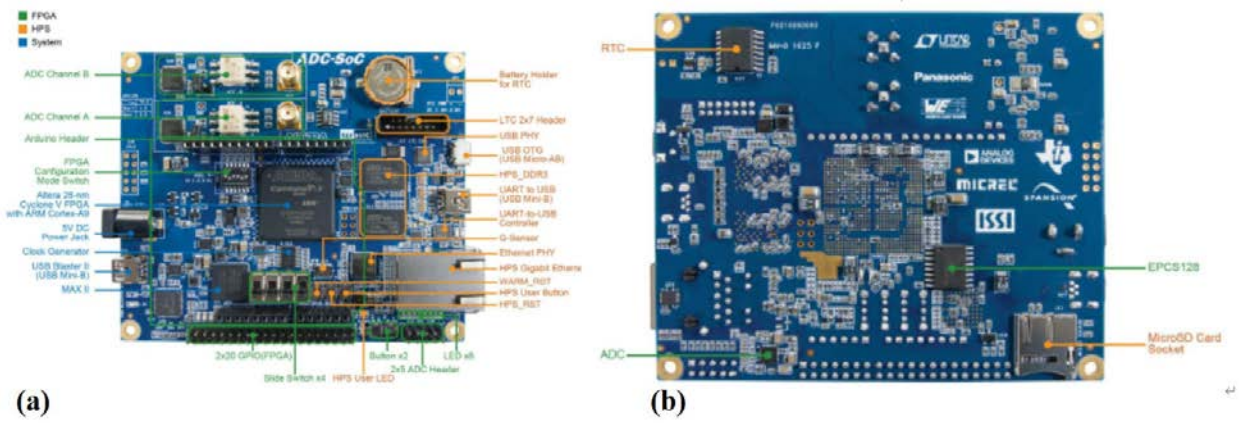

Figure 3-10. The photograph of the ADC-SOC FPGA, (a) front view, (b) back view.

As mentioned above, ADC-SoC FPGA has two High-Speed Analog to digital conversions. Each ADC channel has a 14-bit resolution. The Vpp of the ADC can be set as 1V or 2V, which indicates the allowed maximum and minimum input analog signal is ±1V or ±2V. Thus, to get the best resolution between the input analog signal and the digital signal, we need an attenuator to adjust the input analog signal to satisfy the maximum and minimum requirements of the digital

signal. The digital sample range shown in the ADC is from -8192 to 8192.

In our case, we used the current probe Pearson 6595 (0.5V:1A) and an attenuator (1:10) to measure the current of the resistor with 1.13 kΩ, which is parallel with the discharge tube. The current information is sent to ADC channel A, and the Vpp of the ADC channel A we set as 1 V. Thus, the applied voltage can be calculated using the current information recorded by ADC channel A. In principle, with the above apparatus, the maximum output voltage that can be recorded by our ADC channel A is 20 kV. Through proofreading, we can obtain the relationship between the output voltage and the digital signal of the ADC channel A. And the relationship is shown in Figure 3-11(a).

Similarly, we used the current probe Pearson 6595 (0.5V:1A) and two attenuators (total attenuation ratio with 1:100) to measure the current of the discharge load. The current information is sent to ADC channel B, and we set the Vpp of ADC channel B as 2 V. In principle, with the above apparatus, the maximum discharge current that can be recorded by our ADC channel B is 100 A. And the relationship between the discharge current and the digital signal of the ADC channel B is shown in Figure 3-11(b).

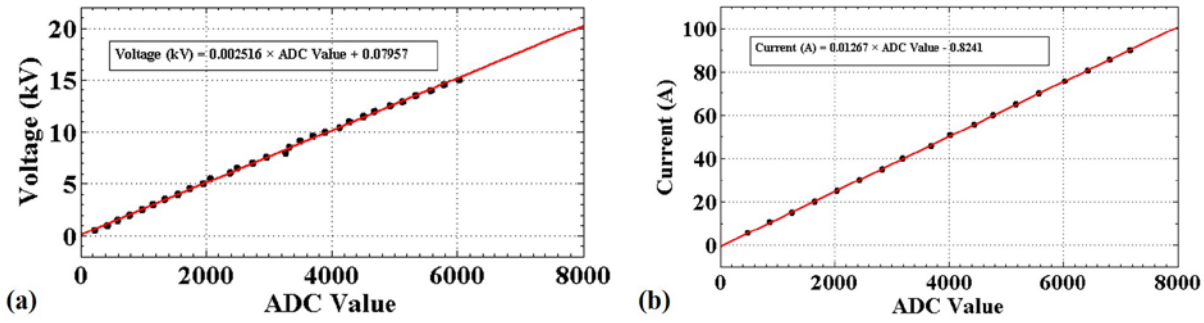

Figure 3-11. The relationship between the analog signal of the load and the digital signal of the ADC, (a) voltage and ADC channel A, (b) current and ADC channel B.

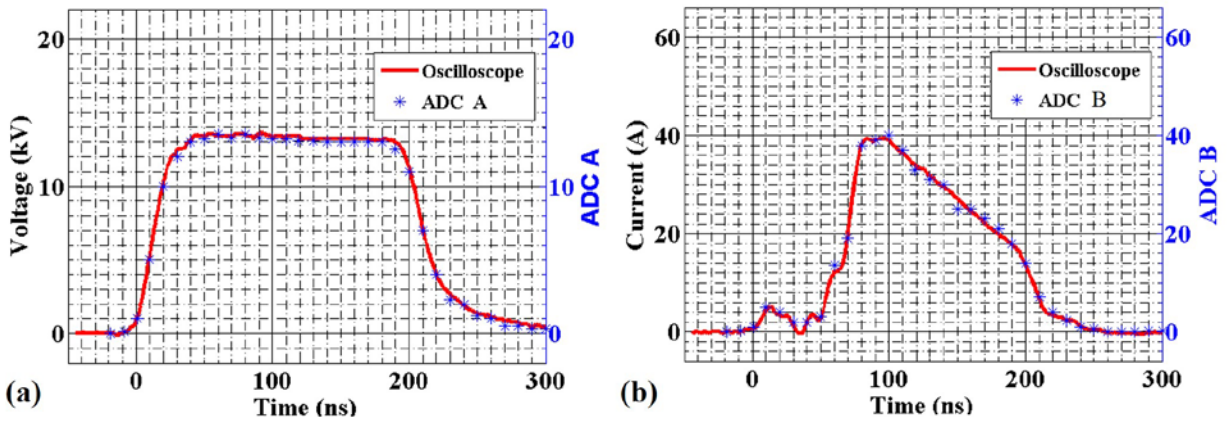

Figure 3-12. Compare the discharge waveform recorded by the oscilloscope and the ADC, (a) voltage, (b) current.

With the ADC-voltage-current relationship obtained above, we can compare the real discharge waveform recorded by the oscilloscope and the ADC. The results are shown in Figure 3-12(a) and Figure 3-12(b), and the impedance is shown in Figure 3-12(c). The results indicate that the ADC waveform record and the oscilloscope are almost the same. Thus, we can provide feedback on the load information to the FPGA through the sensor and the ADC. In principle, with our predetermined program, the FPGA has the ability to output appropriate control signals to control the SSLTD, and the behavior of the load is controlled based on the SSLTD behavior. Thus, with our feedback control system, automatic control of the load behavior is possible.

3.2.5 Delay Time of the Feedback Circuit

For high repetition frequency pulsed power, the delay time of the feedback is significant. Ignoring the repetition frequency of the switch, the transmission time of the feedback circuit and the time for the FPGA to process the feedback signal become essential factors in limiting the repetition frequency of the pulsed power based on the feedback control. In this section, we focus on analyzing the delay time of the feedback circuit.

As is shown in Figure 3-13, our feedback control system has 1000 ns delay times from shot

to shot. The delay time can be divided into two parts. The first part of the delay time is due to the transmission delay of the feedback circuit, which can take up to 340 ns and depends mainly on the transmission circuit. This delay can be divided into four steps:

(1) The FPGA transmits the control signal to the electro-optical conversion system, which takes about 20 ns.

(2) The control signal is then transmitted from the electro-optical conversion system to the SSLTD, which takes around 30 ns.

(3) Once the SSLTD receives the control signal, it outputs the voltage waveform to the load, which can be measured using a voltage probe. This transmission takes about 120 ns.

(4) At the same time, we measure the current of the resistor using a current probe with a three-meter-long coaxial cable, and the current information is transmitted to the FPGA via the ADC. This step can take up to 170 ns.

Therefore, the total transmission delay time of the first part is approximately 340 ns.

The second part is the delay time spent in the FPGA analyzing the feedback information from the circuit, and our FPGA program mainly dominates the delay time. This process may spend 600 ns. The detail as describing steps (5)~(6):

(5) . It is worth noting that we need to set a trigger signal to avoid the noise. When the continual digital signal is higher than our trigger, we record 40 valid signals at a time in sequence. Considering the timing of each signal is 10 ns, it's required for this process 400 ns. Those 40 valid signals include 10 valid signals before the trigger, 20 valid signals during the discharge, and 10 valid signals after discharge.

(6) . After the FPGA records all the feedback information, it calculates and analyzes it. The flowchart of the analysis process is shown in Figure 3-8. This step takes about 200 ns. Based on

the analysis result, FPGA prepares the control signal for the next pulse based on the analysis result.

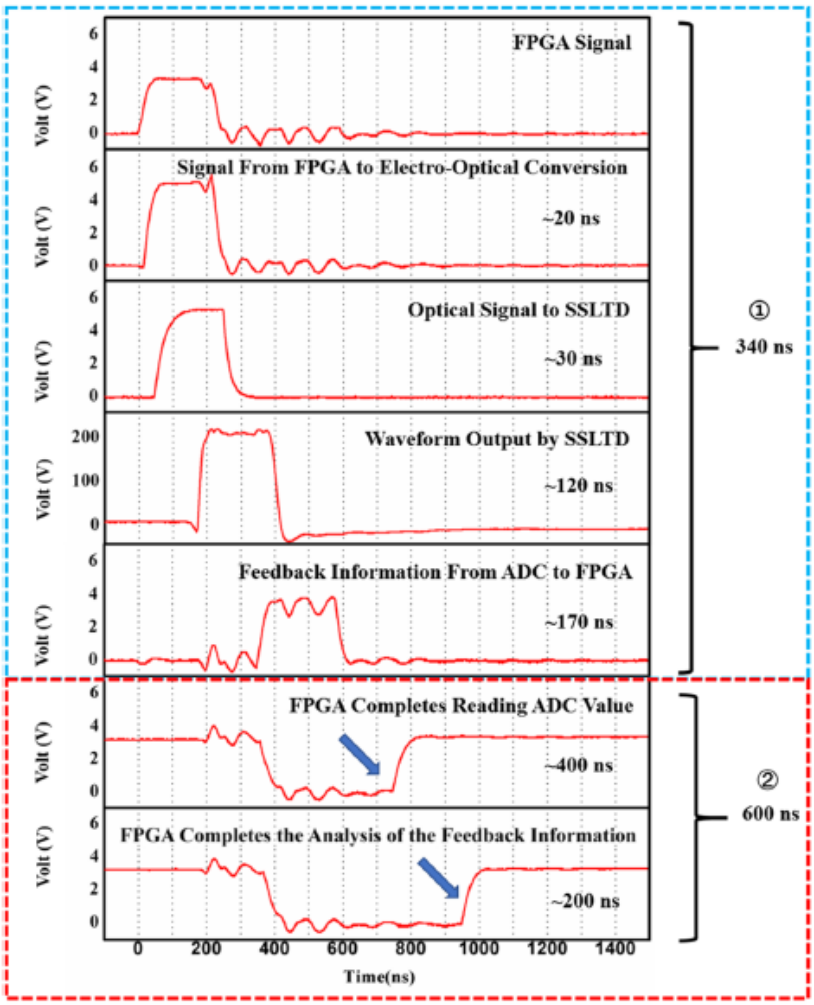

Figure 3-13. Delay time of each step in a feedback control cycle.

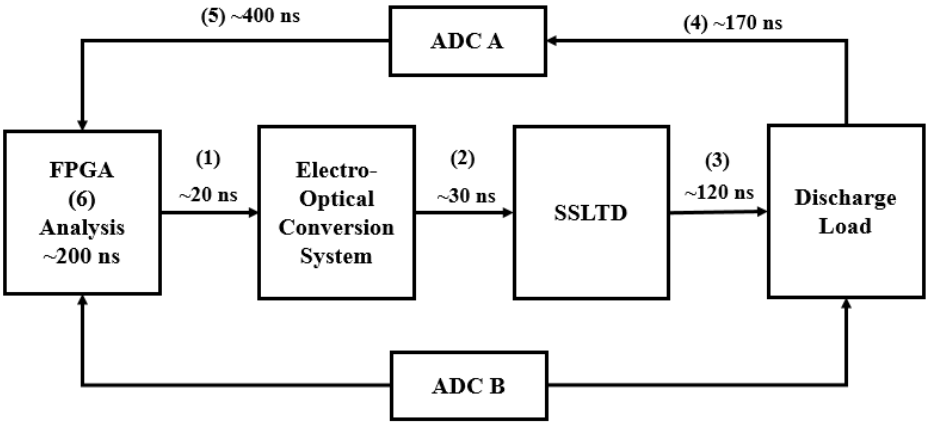

Figure 3-14. Delay information about the feedback circuit.

Based on the analysis results presented above, it can be concluded that the total delay time of the feedback control cycle is approximately 1000 ns, which includes the individual delay times of each step shown in Figure 3-14.

3.2.6 Feedback Control Experiment

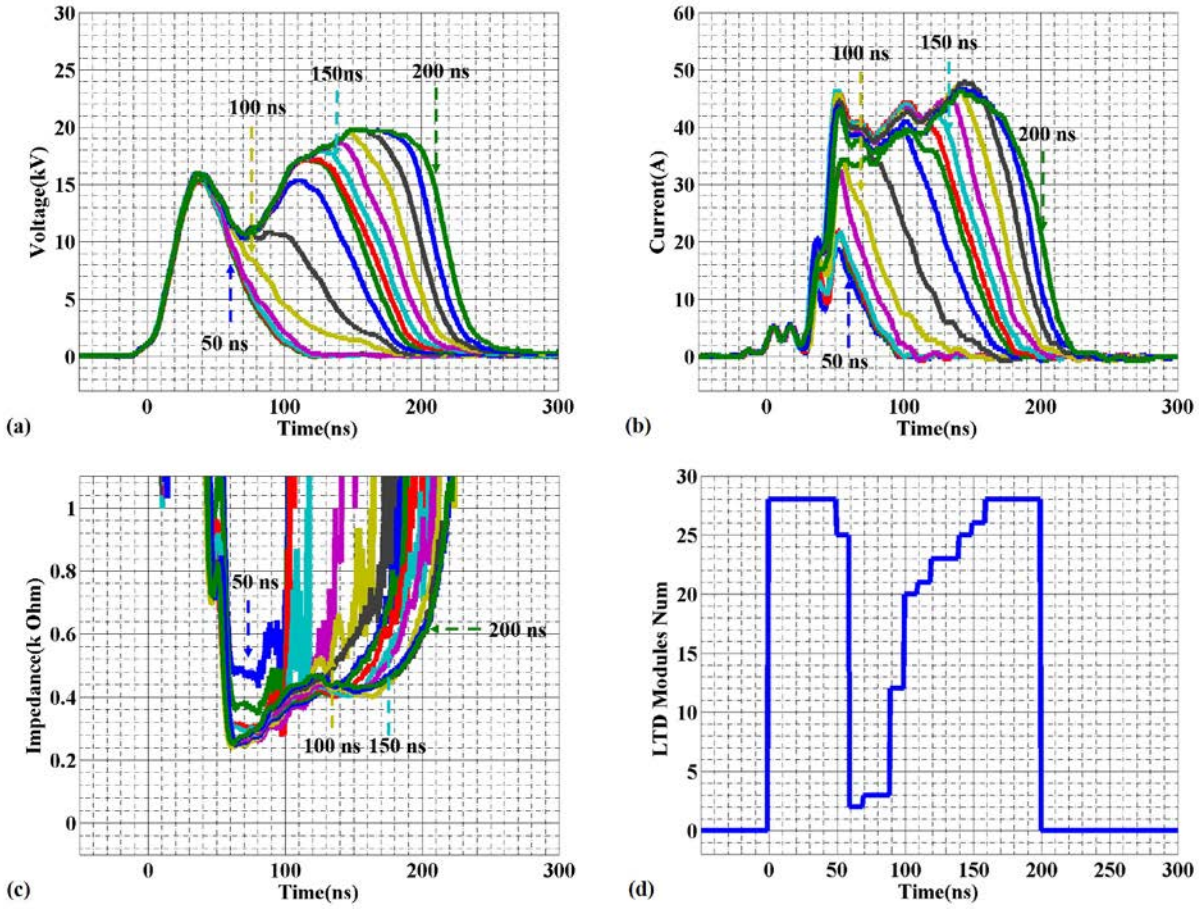

Figure 3-15. The waveform when the impedance of discharge load is maintained near 400 Ω, (a) voltage, (b) current, (c) impedance, and (d) SSLTD numbers.

We conducted a demonstration experiment on our SSLTD feedback control system to regulate the impedance of atmospheric pressure gas discharge at 400 Ω. The experiment involved charging 28 SSLTD modules to 650 V and gradually increasing the FWHM of the FPGA control signal from 0 to 200 ns. Our feedback control system automatically adjusted the output waveform

of the SSLTD for each shot based on the feedback information of the previous pulse. The experimental results are shown in Figure 3-15(a)-(c) for typical voltage, current, and impedance waveforms at different timing steps from 50 to 200 ns. Figure 3-15(d) illustrates the number of SSLTD modules that were switched on at each timing step when the discharge impedance was near 400 Ω.

According to Figures 3-15(c) and 3-15(d), we can see that a large number of modules were initially switched on (0-50 ns) to initiate gas breakdown and discharge current. However, if the voltage amplitude is sustained, it will expand the discharge plasma and quickly form a low-impedance channel between the electrodes. As a result, the number of active SSLTD modules decreases from 60 to 80 ns due to the residual charge after discharge, causing the discharge load impedance to gradually increase. Consequently, the remaining output voltage is insufficient to maintain a constant impedance, requiring a higher voltage to keep the impedance constant. Therefore, the number of SSLTD modules was increased step by step from 80 to 200 ns. After numerous shots, the impedance of the discharge load can be sustained near 400 Ω and remain nearly constant for about 100 ns.

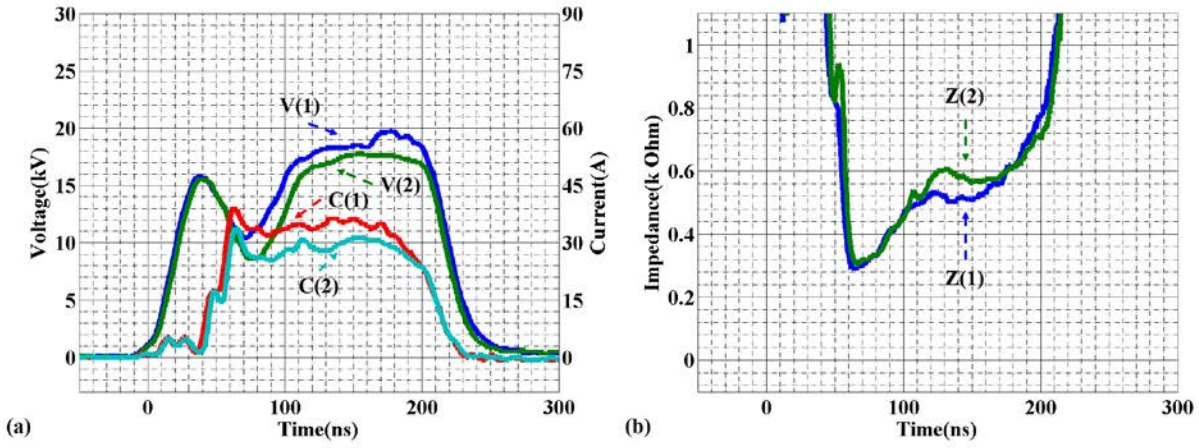

Figure 3-16. The waveform when the impedance of discharge load is maintained near 500 and 600 Ω, (a) voltage and current and (b) impedance.

This is just a demonstration experiment for our feedback control system. Similar experiments have been carried out for targeting impedance at 500 and 600 Ω, and the results are shown in Figure 3-16, where V, C, and Z represent the voltage, current, and impedance waveforms, respectively.

3.3 Conclusion

In this chapter, we studied the control problem of time-varying impedance in atmospheric pressure gas discharge. Given the characteristics of time-varying impedance, we proposed a method of flexibly controlling the pulse waveform within a single pulse to manage the time-varying impedance. In our control experiment, we used an SSLTD with flexible output as the pulsed power source and built a corresponding feedback control system to achieve automatic adjustment of the gas discharge impedance.

The experimental results demonstrate that the feedback control scheme based on SSLTD can maintain the impedance of atmospheric pressure gas discharge at a constant value of 400, 500, or 600Ω within a range of 100 ns.

The implication of this development is very significant. It shows that our SSLTD pulsed power generator can **SEE** the load behavior of the previous pulse. It can **THINK** in order to find out a better output waveform. And it can **ACT** by generating this improved waveform, which can change the load behavior.This has great practical importance for applications involving pulsed atmospheric pressure gas discharge

CHAPTER IV: RESIDUAL CHARGES PHENOMENON STUDIED BY BIPOLAR SOLID-STATE LINEAR TRANSFORMER DRIVER

4.1 Overview

The repetitive nanosecond pulsed discharge has been gaining more attention in the plasma science community because of its complex and sometimes stochastic behavior in atmospheric pressure gas discharge. Stochastic behavior means that even under identical controllable conditions, parameters such as occurrence time and amplitude of two atmospheric pressure gas discharge behaviors may differ. The pulse discharge phenomena are different from traditional AC/DC discharge, as evidenced by differences in discharge regime classification, runaway electron phenomenon, fast gas heating, and inherent memory effects [40-46].

The memory effect, which refers to the dependence of the present state on past history, is caused by products generated in previous pulses, such as residual charges, that alter the electric field strength and affect subsequent pulses. There are many factors that contribute to the memory effect in successive pulsed discharges, which can be categorized based on their impact. One category is associated with the aging process that produces a permanent change in material or geometrical structure, such as surface conductivity change, gas composition variation, or electrical tree propagation discharge.

Our previous research has shown that applying positive-positive (PP) pulses to atmospheric pressure gas discharge results in a memory effect where the peak current of the second pulse is smaller than that of the first [47]. Figure 4-1 shows a typical waveform of this phenomenon, generated by the unipolar SSLTD pulse waveform discussed in CHAPTER II.

The reason for this phenomenon is easily understood through our understanding of discharge

physics. After a pulse discharge, residual charges accumulate in the discharge space, which can affect the electric field strength of subsequent pulses. In the case of positive pulse discharge, positive residual charges are generated in the discharge space after the first pulse. As a result, the positive ions weaken the electric field strength of the second positive pulse, causing a drop in its current, as demonstrated in our previous research.

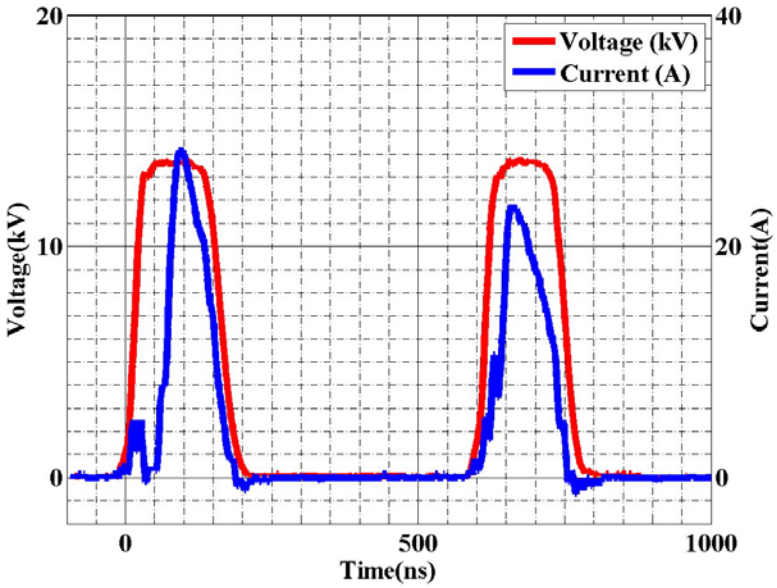

Figure 4-1. Typical successive positive-positive pulsed discharges waveform.

Figure 4-2 depicts a typical 1-D discharge model to demonstrate the changes in residual charge and electric field strength during pulse discharge. The model illustrates the cross-sectional area of the discharge load. As seen in Figure 4-2(a) under scenario P1, there are no residual charges present in the discharge space prior to the first positive pulse discharge. As for P2 in Figure 4-2(a), the positive ions are created in the discharge space after the first positive pulse discharge. The electric field strength can be calculated using the Poisson Equation, and the equivalent electric field strength of the first and second positive pulses is illustrated in Figure 4-2(b). Due to the effect of positive ions, the electric field strength of the second positive pulse

discharge is expected to be lower than that of the first pulse discharge.

Additionally, residual ion clearing can improve the performance of pulsed discharge systems and contribute to the development of new applications, such as plasma-based medical treatments and environmental remediation. In the following sections, we will review various methods for residual ion clearing, including dielectric barrier discharge, pulsed arc discharge, and corona discharge, and discuss their advantages and disadvantages. We will also provide experimental results to demonstrate the effectiveness of each method. Overall, this chapter aims to provide a comprehensive overview of residual ion clearing techniques for pulsed discharge systems and to promote further research in this area.

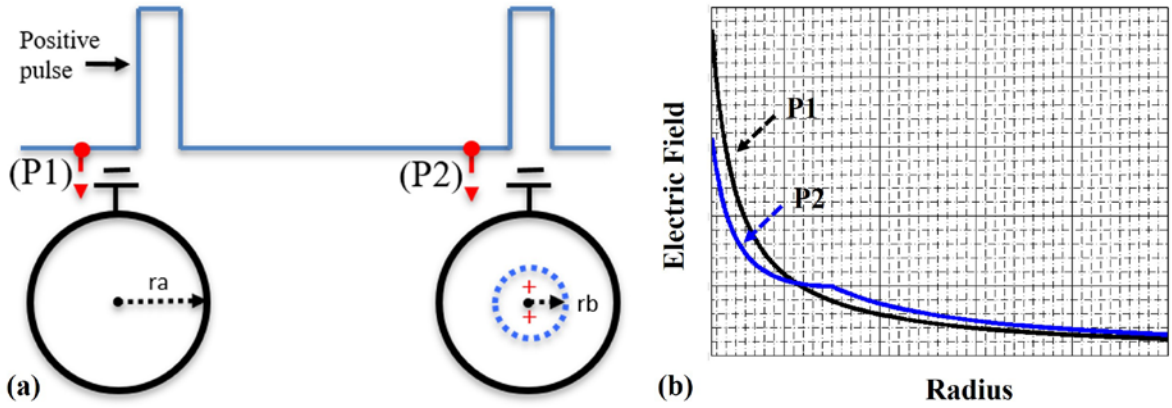

Figure 4-2. One-dimensional model explanation of the phenomenon in Figure 4-1, (a) Equivalent residual charge before pulse discharge, (b) equivalent electric field strength for the first pulse and the second pulse.

4.2 Theoretical Analysis

As mentioned earlier, residual positive ions can weaken the electric field strength of the following positive pulse discharge, causing a drop in current. Conversely, negative residual charges can enhance the electric field strength of the positive pulse, resulting in an increase in current. Injecting electrons into the discharge space after the positive pulse discharge can neutralize the charge effect of positive ions.

It has been reported that negative charges can be generated through high electric field strength field emission by negative pulse discharge, following the Fowler-Nordheim law [48]. Moreover, the number of electrons in the discharge space can increase due to explosive emission effects when the discharge material is uneven. As illustrated in Figure 4-3, injecting electrons into the discharge space between the first and second positive pulse using a negative pulse can neutralize the charge effect of positive ions, resulting in an increase in the electric field strength and current of the second positive pulse.

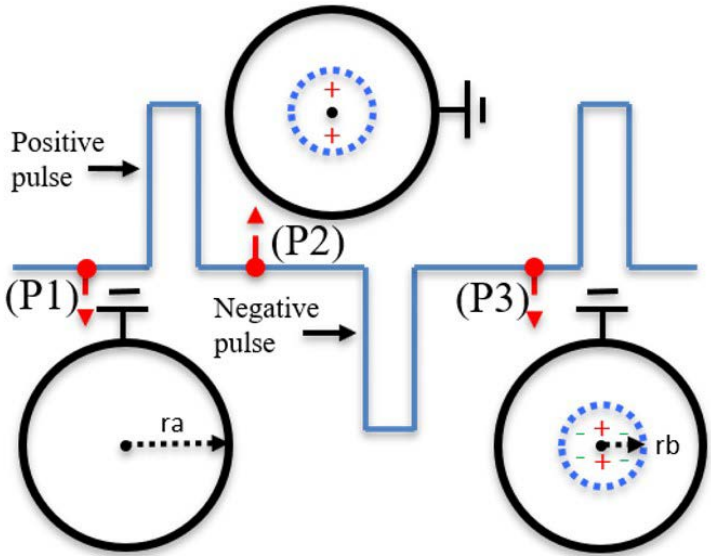

Figure 4-3. One-dimensional model explanation of the residual charge phenomenon for bipolar pulsed gas discharge.

To effectively study the memory effect and neutralize the charge effect of positive ions, it is essential to use a flexible bipolar pulsed power generator that can provide a negative pulse waveform immediately after the positive pulse discharge. This allows the injection of electrons into the discharge space to neutralize the residual positive charges, which enhances the electric field strength and current of the subsequent positive pulse. Without such a generator, it would be difficult to investigate the effects of residual charges on the discharge behavior and gain a deeper understanding of gas discharge physics.

4.3 Development of bipolar SSLTD Pulsed Power Generator

4.3.1 Introduction of Bipolar SSLTD

To study the memory effect and neutralize the charge effect of positive ions, a flexible bipolar pulsed power generator is crucial. The modular structure of the SSLTD enables adjustments based on the specific application requirements. For instance, flipping certain modules can output a negative pulse waveform on the load, resulting in bipolar output. With appropriate control signals, a wide range of bipolar output waveforms can be generated using our bipolar SSLTD. These waveforms have potential applications in several fields, such as environmental studies, biological organisms, and gas discharge physics research.

The scheme for our bipolar SSLTD is to connect positive polarity modules and negative polarity modules in series. However, the crucial aspect of a bipolar SSLTD is that it must allow reverse current to pass through non-working modules of a certain polarity. To achieve this, the magnetic core on the non-working modules must be kept in a saturated state. Otherwise, the reverse current passing through these non-working modules would be in the form of leakage current, which would limit the effectiveness of the bipolar SSLTD.

Based on the essential features of bipolar SSLTD discussed earlier, a new kind of bipolar SSLTD has been developed that utilizes positive and negative module-sharing magnetic cores. The BH curves of the magnetic core used in the bipolar SSLTD are shown in Figure 4-4. When the positive pulse waveform is output on the load, the magnetic excitation point of the core moves from $-B_S$ to B_S. Conversely, when the negative pulse is output to the load, the magnetic excitation point of the core moves from BS to -BS. This type of bipolar SSLTD can be operated at high frequencies.

The equivalent circuit of share magnetic core type bipolar SSLTD is shown in Figure 4-5(a). In our case, a bipolar SSLTD module is based on two unipolar SSLTD modules. As for one bipolar SSLTD module, the positive and negative modules share the same magnetic core. In principle, the reset circuit becomes unnecessary by keeping the Vdischarge×Tdischarge of the positive and negative pulse equal.

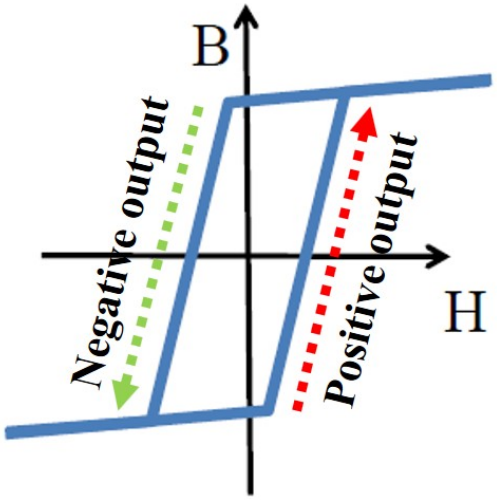

Figure 4-4. Hysteresis loops operated principle of share magnetic core scheme bipolar SSLTD.

The output principles of the bipolar SSLTD are shown in Figure 4-5(b), where Figure 4-5(b1) illustrates the positive output principle, and Figure 4-5(b2) illustrates the negative output principle.

It is important to note that in the shared magnetic core bipolar SSLTD scheme, the withstand voltage of both the positive and negative modules must be considered during each period. Regardless of whether the positive or negative pulse is being output, the switches in the working module can withstand a voltage of Vload minus Vcharge, while the switches in the non-working module can withstand a voltage of Vload plus Vcharge, and vice versa. Within each module, Vload equals Vcharge. However, this design has a disadvantage, as the maximum voltage that

the switches can withstand in a single cycle is limited to 2×Vcharge.

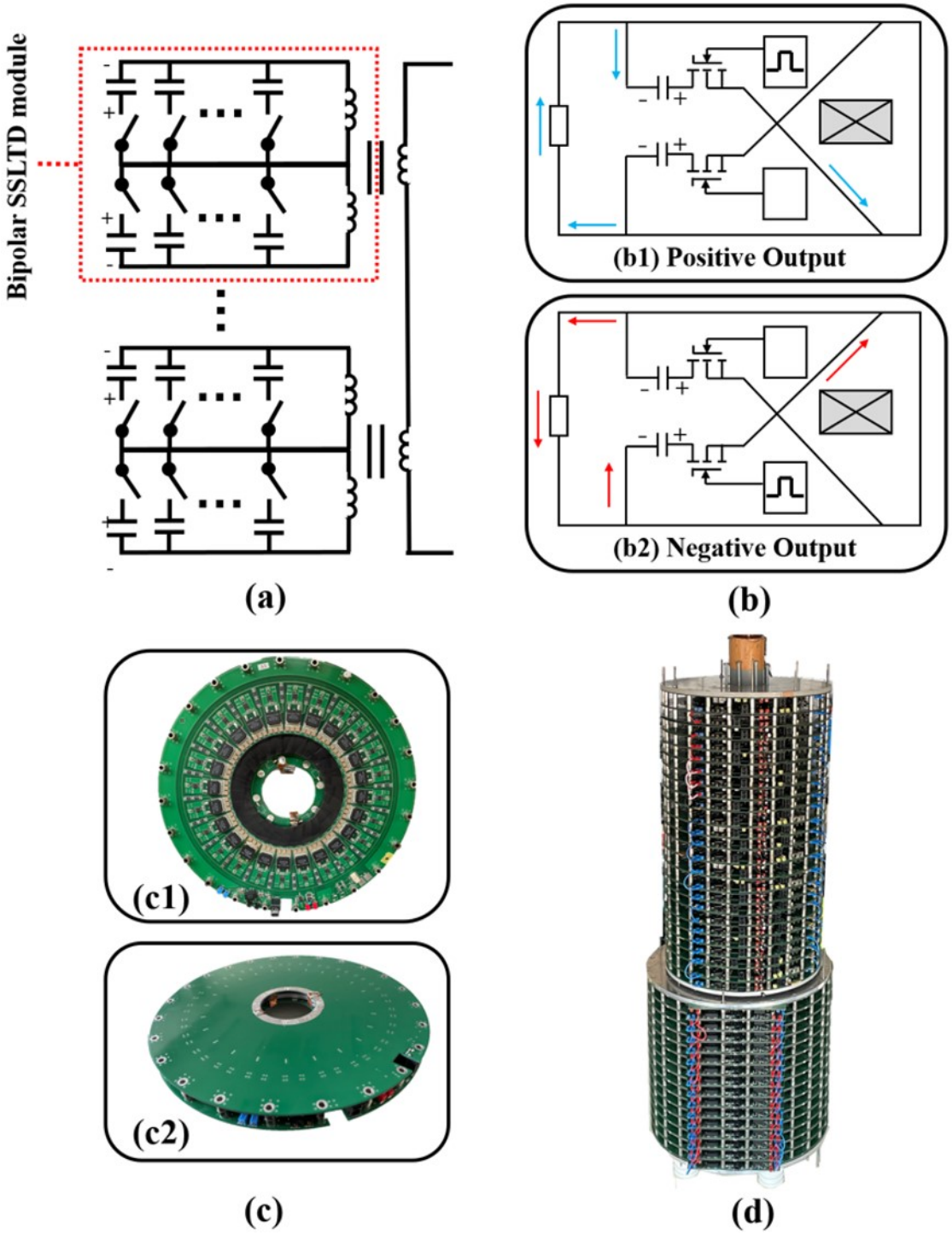

Figure 4-5. Bipolar solid-state linear transformer driver, (a) equivalent circuit, (b) operation principle of bipolar SSLTD, (c) front-side photo of an SSLTD module, and (d) the Bipolar SSLTD system consisting of 39 modules.

The front-side photos of one module of unipolar SSLTD and bipolar SSLTD are shown in Figure 4-5(c). In Figure 4-5(c1), a unipolar SSLTD module is presented, which is similar to the one mentioned in CHAPTER II, but with the diode removed from the board. Figure 4-5(c2) shows a bipolar SSLTD module, which is a combination of two unipolar SSLTDs. To achieve the bipolar output, one of the unipolar modules is turned upside down and then combined with another unipolar module. The magnetic core is located in the sandwiched space between the upper and lower modules of the bipolar SSLTD. As mentioned earlier, the maximum voltage the switches can withstand in a cycle is 2×Vcharge. Therefore, a large number of SSLTD modules are required to generate the necessary pulse amplitude. Figure 4-5(d) shows a bipolar SSLTD system with 39 modules. In our case, we used two sizes of SSLTD modules to set up the bipolar SSLTD system. The upper modules use the MOSFET switch with IXFT6N100F, while the lower modules use the MOSFET switch with DE475-102N21A. Although their sizes and switches are different, the equivalent circuits of these two types of SSLTD are the same. It is important to note that the withstand voltage of positive and negative modules should be considered during one period in the share magnetic core bipolar SSLTD scheme. Whether during the positive or negative pulse output, the withstand voltage of switches in the working module is Vload - Vcharge and switches in another non-working module are Vload + Vcharge, and vice versa. In each module, Vload = Vcharge. This means that the maximum voltage that the switches can withstand in a cycle is 2×Vcharge, which is a disadvantage of our bipolar SSLTD.

4.3.2 Performance Test and Analysis of Bipolar SSLTD

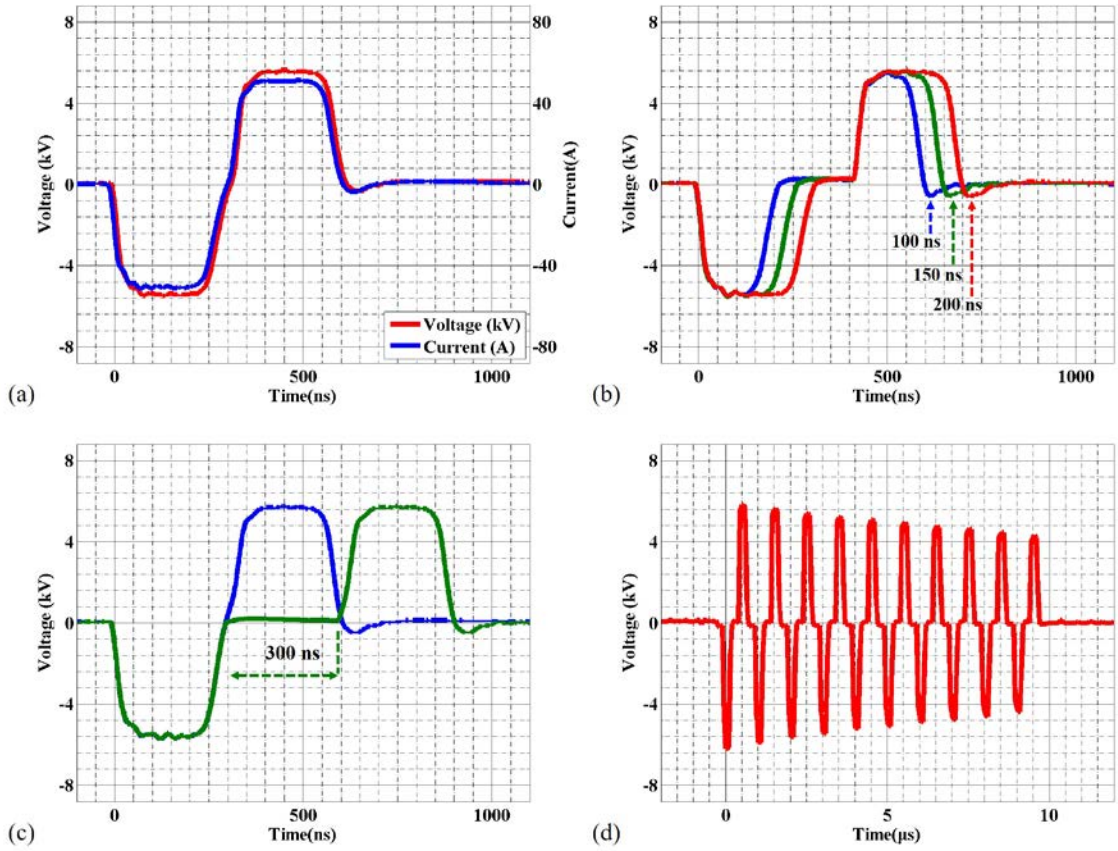

Figure 4-6. Typical output waveforms are obtained using the bipolar SSLTD system, (a) Typical voltage and current waveforms, (b) voltage waveforms with different pulse widths, (c) voltage waveforms with different pulse intervals between negative and positive, and (d) voltage waveform of 19 bursts at 1 MHz.

Figure 4-6 displays typical output waveforms generated by the bipolar SSLTD system using 39 modules to charge 400 V. Figure 4-6(a) presents the voltage and current waveforms, while Figure 4-6(b) shows the bipolar output waveform with pulse widths ranging from 100 to 200 ns. Figure 4-6(c) illustrates the output waveform with varying pulse intervals between negative and positive pulses. Finally, Figure 4-6(d) demonstrates the 19-burst output at 1 MHz. Although the first bipolar pulse output reaches ± 15 kV, the last bipolar output voltage decreases to ± 9 kV due to the small capacitance of the charging capacitor. However, with a larger capacitance, it is

believed that the system could operate even at 1 MHz.

The share magnetic core type bipolar SSLTD offers the advantage of high-frequency output on the load, but requires synchronous switching of all modules.

4.4 Gas Discharge Residual Charge Effect Experiment Driven by Bipolar SSLTD

4.4.1 Negative-Positive (NP) Pulse Gas Discharge Experiment

Figure 4-7 displays the waveform of a negative-positive (NP) pulse discharge generated by our bipolar SSLTD system consisting of 39 charged modules, each at 360 V. Figure 4-7(a) depicts the voltage waveforms, and Figure 4-7(b) displays the corresponding current waveforms. Voltage 1 and Current 1 represent the signal-positive pulse discharge, while Voltage 2 and Current 2 show the NP pulse discharge. The positive pulse amplitude is 14 kV, and the negative pulse is -14 kV, with both pulses having a duration of 200 ns. As shown in Figure 4-7(b), the negative pulse discharge effectively enhances the following positive pulse discharge.

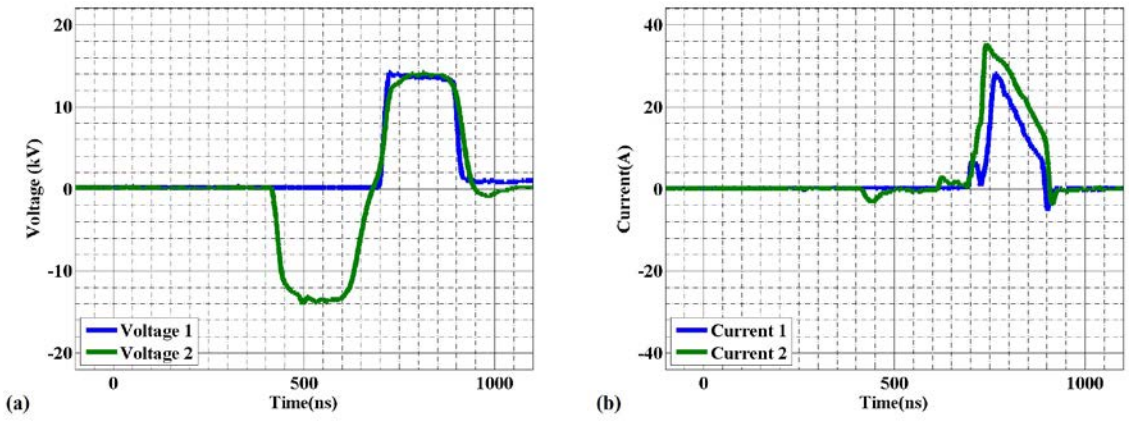

Figure 4-7. Voltage and current waveforms for P and NP pulse discharge, (a) Voltage waveforms, (b) Current waveforms. Voltage 1 and Current 1 are the signal-positive pulse discharge; Voltage 2 and Current 2 are the waveforms for NP discharge.

4.4.2 Positive-Negative-Positive (PNP) Pulse Gas Discharge Experiment

Building upon the previous discussion, we conducted an experiment to generate positive-negative-positive (PNP) pulse discharge using our bipolar SSLTD system. The resulting output waveform is presented in Figure 4-8. Specifically, Figure 4-8(a) displays the voltage waveform, Figure 4-8(b) shows the real discharge current waveform, and Figure 4-8(c) depicts the current waveform of the negative pulse based on Figure 4-8(b).

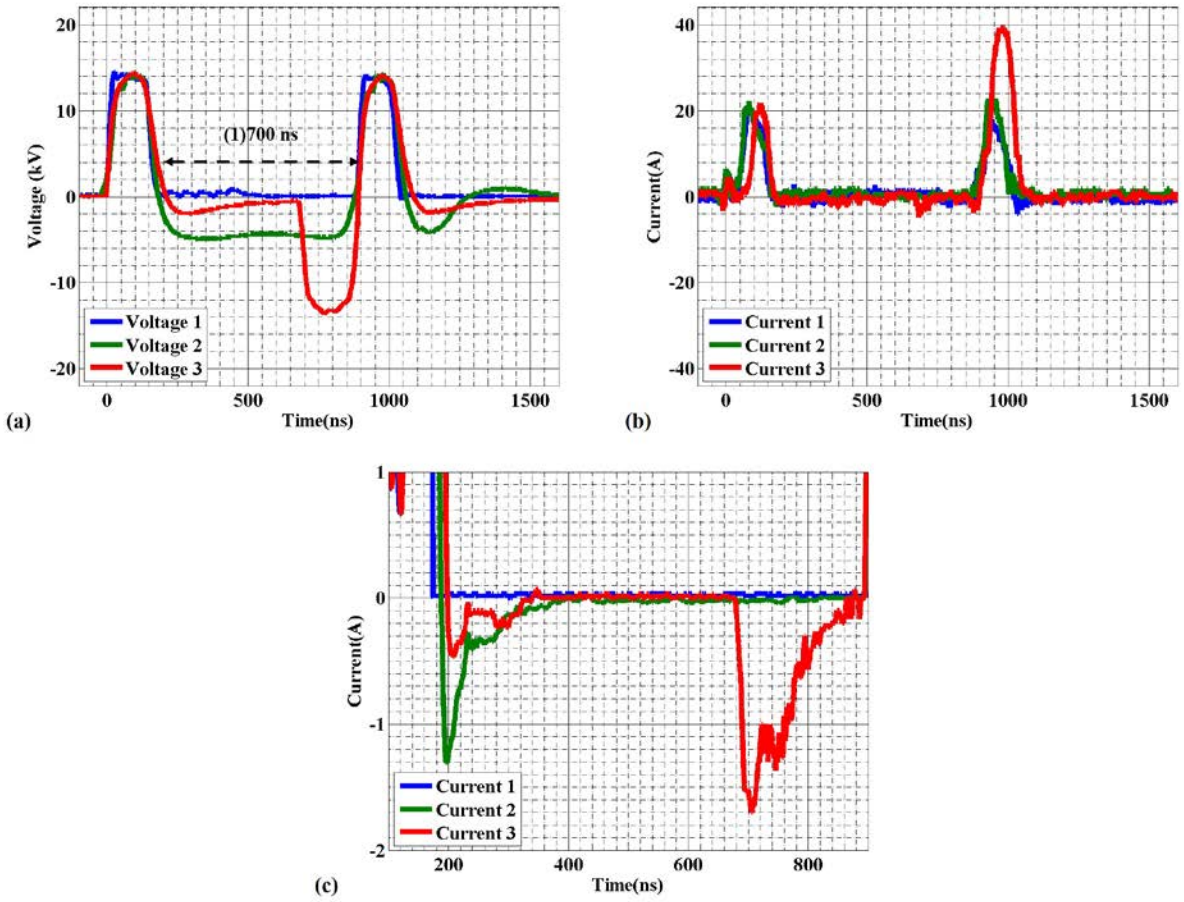

Figure 4-8. Voltage and current waveforms for PNP pulse discharge, (a) voltage waveform, (b) waveform of the discharge current, (c) current waveform of the negative pulse.

In Figure 4-8, Voltage 1 and Current 1 represent the waveforms of PP discharge, with the current of the second positive pulse being smaller than the first. However, after applying a

negative pulse with -4 kV between the first and second positive pulses, the current of both positive pulses becomes almost the same, as shown in Voltage 2 and Current 2. It's important to ensure that the $V_{discharge} \times T_{discharge}$ of the positive and negative pulse is equal for safe operation of our bipolar SSLTD. Therefore, the pulse time of the negative pulse needs to be extended. When a negative pulse of -14 kV is applied, the current of the second positive pulse in Voltage 3 and Current 3 is significantly higher than the first.

The discharge current of the negative pulse in Current 3 of Figure 4-8(c) is around 1 A. As a reference, we can calculate the field emission current using the simplified Fowler-Nordheim law for a negative pulse of -14 kV, which gives an estimated current of approximately 0.02 A. This is much lower than the measured value in Current 3, which may be due to fine concave-convex structures in the copper wire enhancing the local electric field, leading to explosive emission and increasing electron emission [49].

Figure 4-9 shows the luminescence images of coaxial electrode discharge. The images are taken on the direct rear side of our discharge tube, as shown in Figure 4-9(a). Its equivalent model is shown in CHAPTER III. The inner diameter of the discharge tube is 20 mm. And the diameter of the thin copper wire is 1 mm. Figure 4-9(b) ~ Figure 4-9(d) are the discharge luminescence images based on the pulsed waveform Voltage 1 ~ Voltage 3 shown in Figure 4-8(a), respectively. The pulse waveforms are operated at 100 Hz. As for the discharge images, the exposure time is 0.5 s, and the ISO is 1600. The inside of the red dotted line shows the images of discharge luminescence. From the images of the discharge luminescence, we can see that the glow discharge has occurred, and the plasma has been generated under our experimental conditions. Also, with the same positive pulse conditions, the luminous intensity is related to the discharge current. The stronger the discharge luminous intensity, the greater the discharge peak current.

Figure 4-9 shows that the luminous intensity sequence is Figure 4-9 (d) > Figure 4-9 (c) > Figure 4-9 (b), although the amplitudes of the positive pulse are near the same. However, the main different pulse condition of Figure 4-9 is the amplitudes of the negative pulse. It is indicated that the negative pulse is indeed beneficial to improve the residual charge effect produced by the positive pulse and increase the discharge intensity of the positive pulse.

Previous experiments and images prove that the residual charge effect of positive ions left by the first positive pulse can be neutralized by applied a apposite negative pulse between the first and the second positive pulse.

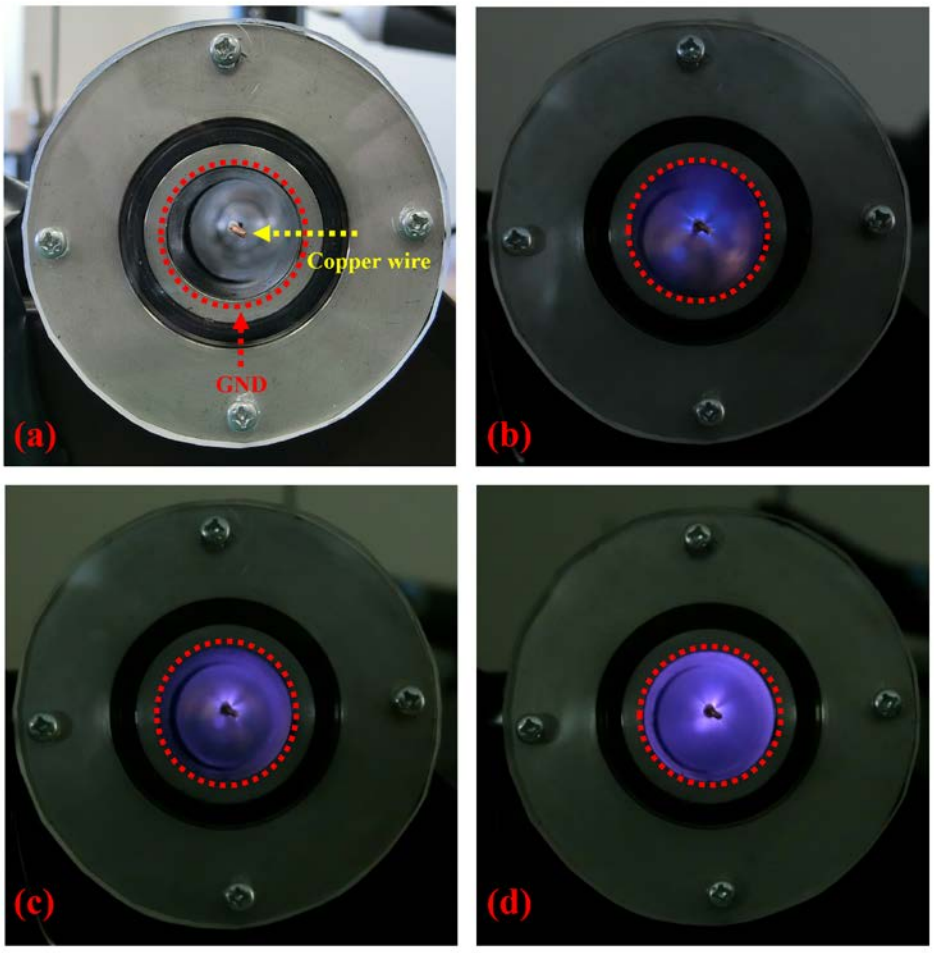

Figure 4-9. Luminescence images of coaxial electrode discharge based pulsed waveform in Figure 6(a), (a) Discharge tube structure, (b) PP discharge, (c) PN(-4kV) P discharge, (d) PN(-14 kV)P discharge.

Based on the condition shown in Figure 4-8, we can vary the amplitude of the negative pulse to investigate the relationship between the amplitude of the negative voltage and the current of the second positive pulse. The results are presented in Figure 4-10, where I_1 and I_2 represent the peak currents of the first and second positive pulses, respectively. The experimental findings suggest that as the amplitude of the negative pulse increases, the current of the second positive pulse increases significantly.

It should be noted that the current ratio of several data points on the right is slightly lower than that of the PP discharge mode (when the negative voltage amplitude is 0). Specifically, the current ratio of PP is 0.89, while the minimum current ratio of PNP is 0.86, which has a margin of error of 3%. Given that the impedance of the atmospheric pressure gas discharge is not constant and the peak current fluctuates within a small range of each pulse, we consider this slight fluctuation acceptable. Additionally, the amplitude of the negative pulse is too low to produce enough electrons to neutralize the positive ions.

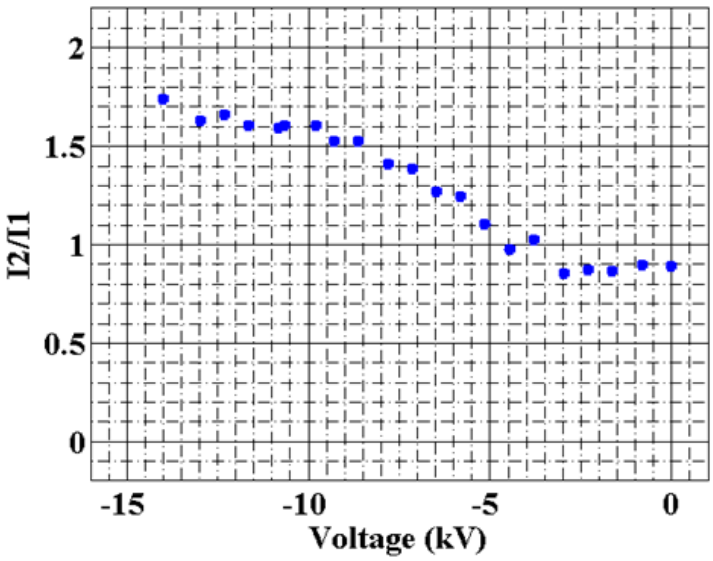

Figure 4-10. Current ratio versus negative pulse amplitude for PNP pulse discharge.

Similarly, we have investigated the relationship between the pulse time interval and the

current ratio. The pulse amplitude and duration are nearly the same as those of Voltage 3 in Figure 4-8, but the pulse interval is varied. The pulse time interval is defined as the time interval from the previous pulse drop to the following pulse rise. The results are shown in Figure 4-11. Figure 4-11(1) shows the current ratio versus pulse time interval based on the PP discharge, where the pulse interval is between the first and second positive pulses. An example of an interval with a duration of 700 ns is shown in Figure 4-8(a)(1). Figure 4-11(2) shows the current ratio versus pulse time interval based on the PNP discharge, where the pulse interval is between the negative and second positive pulses, and the interval between the first positive and negative pulse is a constant 500 ns.

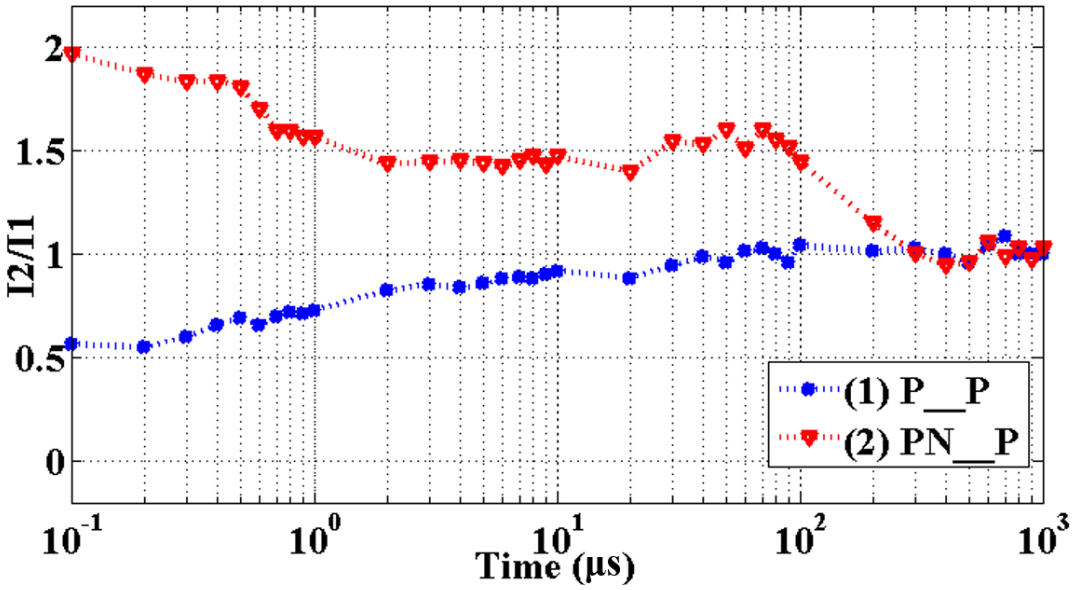

Figure 4-11. Current ratio versus pulse time interval.

Compared with PP discharge, the current of the second positive pulse significantly increased after we provided a negative pulse between the first and the second positive pulse.

It is worth mentioning that the influence of the negative pulse on the subsequent positive pulse can be divided into three parts. The first part is between 100 and 700 ns, during which the negative pulse has a significant impact on the peak current of the second positive pulse. The

second part is between 700 ns and 300 μs, during which the negative pulse affects the following positive pulse at a nearly constant level. After 300 μs, which is the third part, the peak currents of the first and second positive pulses are almost identical.

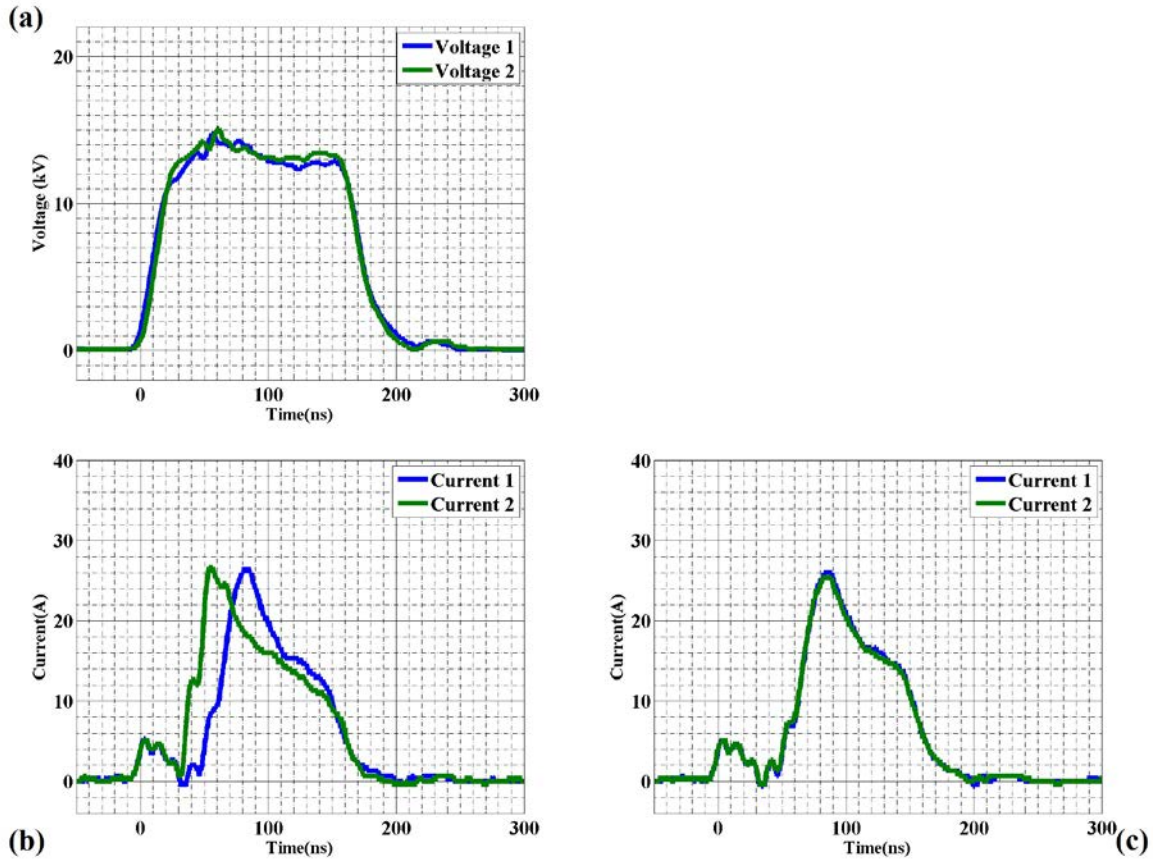

Figure 4-12. Under the PN_P interval conditions shown in Figure 4-11, the voltage-current comparison graphs of the first positive pulse and the second positive pulse are depicted, (a) Comparison graph of the first positive voltage and the second positive voltage at a PN_P interval of 300 μs, (b) Current wavform based on (a), (c) Comparison graph of the current at a PN_P interval of 3 ms.

Further, we provide a more intuitive comparison of the voltage and current waveforms during the discharge, as shown in Figure 4-12. Voltage 1 and Voltage 2 represent the voltage of the first positive pulse and the second positive pulse, respectively, while Current 1 and Current 2 represent the current of the first positive pulse and the second positive pulse, respectively. As

shown in Figure 4-12(a) and (b), when comparing the voltage-current graphs at the 300 μs interval, we observe that the voltage of the first positive pulse is nearly identical to that of the second positive pulse. Additionally, the peak current of the first positive pulse is almost the same as that of the second positive pulse. However, the rise time of the current for the second positive pulse is noticeably faster than that of the first positive pulse, and the discharge amount of the second positive pulse is slightly greater. It is approximately at a pulse interval of 3 ms that the discharge current of the second positive pulse aligns with that of the first positive pulse, as shown in Figure 4-12(c).

These experimental results shown in this section indicated that the charge effect of positive ions can be neutralized by the electrons after we provide a negative pulse between the first and the second positive pulse. The physical interpretation of the phenomenon is given in the next section.

4.5 Physical Explanation

In this chapter, the pulsed gas discharge has been studied by our bipolar SSLTD system. According to the experiment result observed in the previous section, we can learn that some products created after the pulse discharge affect the subsequent pulse discharge.

Considering the huge difference in electron and ion mass, after discharge, the electrons run to the anode in a short time. However, the ions remain in the discharge space for a long time until they dissipate by diffusion and recombination. Thus, the residual charges affect the electric field strength of the subsequent pulse before they are dissipated.

The discharge current is sensitive to the electric field strength of the discharge pulse, and the relationship is not linear. For example, a slight increase in the electric field strength may lead to a certain increase in the current. Conversely, a slight decrease in the electric field strength may

lead to a certain decrease in the current.

In the positive pulse discharge development process, many positive charges are produced. Similarly, many electrons are created in the negative pulse discharge. These positive ions and electrons may have caused the phenomena we observed in the previous section.

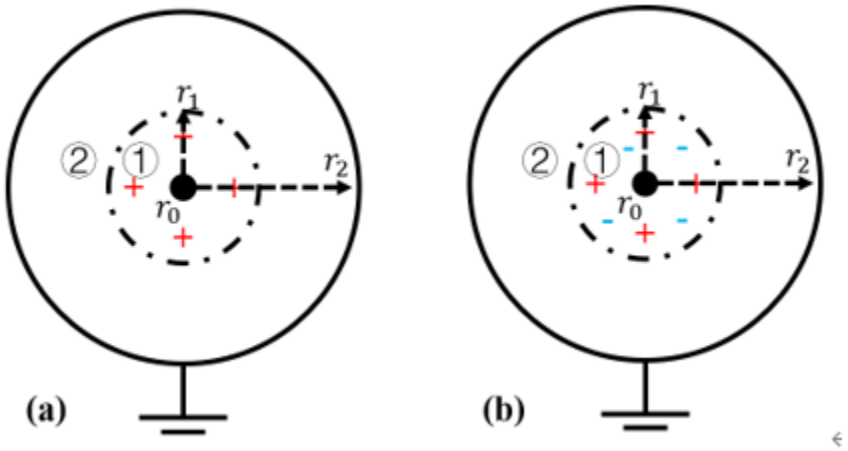

Figure 4-13. 1-D model for calculating the electric field distribution between the electrode. (a) model for PP discharge, and (b) model for PNP discharge. r0 is the radii of the copper wire, r1 is the radii of residual charges, and r2 is the radii of the inner pipe. Regions 1 and 2 denote the regions with and without the residual charge. The ion layer with a thickness of 3 mm.

To give a qualitative explanation, we have calculated the electric field strength for PP and PNP discharge. For simplicity, we assume discharge current only depends on the electric field strength, and the charge density is constant and evenly distributed. Thus, we can solve the Poisson Equation to calculate the electric field strength [50]. Figure 4-13 shows the 1-D cross-sectionals of the discharge load. Figure 4-13(a) shows the model of PP discharge, and Figure 4-13(b) shows the model of PNP discharge. r0 is the radius of the copper wire, r1 is the radius of residual charges, and r2 is the radius of the inner pipe. To represent the residual charges, we have added a layer of residual charge on the surface of the wire indicated as region ① in Figure 10, and the remaining volume between the gap is denoted as region ②. Reference our previous

publication, we have assumed that the ion layer with a thickness of 3 mm.

In the experiments, the number of positive ions and electrons is near the same in the discharge space, as indicated by the almost same current of the first and second pulse in Current 2 of Figure 4-8. Therefore, the number of positive ions can be estimated by evaluating the total charge obtained from the time integration of Current 2. Similarly, the total number of residual space charges can be estimated by considering the neutralization effect of positive ions and electrons obtained from the time integration of Current 3. The statement suggests that the total charge obtained from the time integration of Current 2 is ∼-67 nC/pulse, and the total charge obtained from the time integration of Current 3 is ∼-140 nC/pulse. By taking the neutralization effect into account, the total number of residual space charges in Figure 4-13(b) is estimated to be -73 nC/pulse.

Based on the previous discussion, we can calculate the electric field strength by the Poisson equation. The results are shown in Figure 4-14 where (a) and (b) are the electric field strength of the first pulse and the second positive pulse based on Figure 4-8(a) Voltage 1, (c) is the electric field strength of the second positive pulse based on Figure 4-8(a) Voltage 3. The calculation results shown in Figure 4-14 indicate that for positive pulse discharge, the positive residual charges around the inner electrode lead to a decrease in the electric field strength near the wire electrode compared with that obtained without the residual charge, resulting in the discharge current of the followed positive pulse increase. However, a negative pulse applied after the first positive pulse discharge can inject electrons into the discharge space, and the charge effect of positive ions can be neutralized by the electrons. In this case, it increases the electric field strength near the wire electrode, resulting in the discharge current of the following positive pulse rise.

In other words, pulse discharge is sensitive to the residual charge. For example, positive residual charges inhibit subsequent positive pulse discharges. Negative residual charges promote subsequent positive pulse discharges.

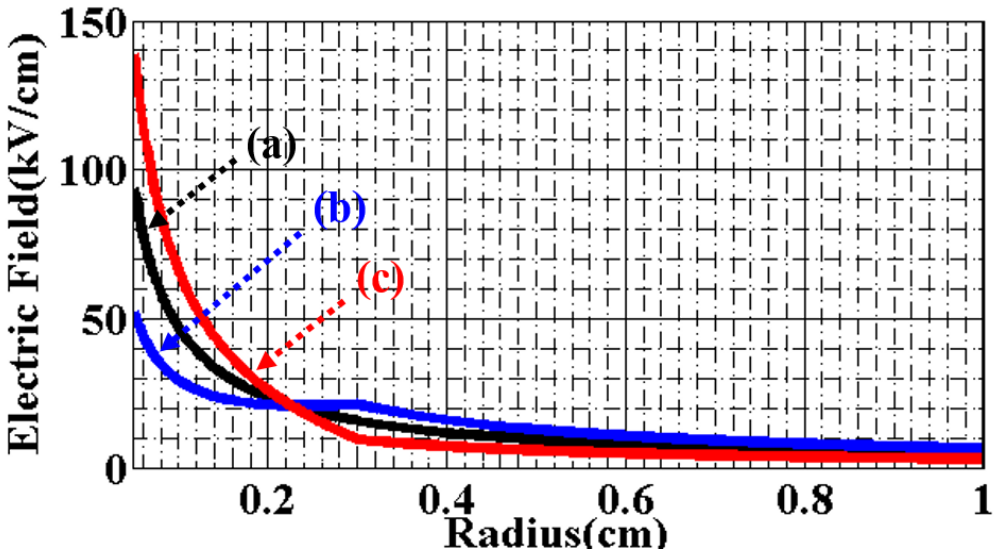

Figure 4-14. Calculation result of electric field strength based on Figure 6 and Figure 10: (a) the electric field strength for the first positive pulse, (b) for the second positive pulse of PP discharge where the residual charge is 67 nC, (c) for the second positive pulse of PNP discharge where the residual charge is -73 nC.

That is why the current of the second positive pulse is usually lower than that of the first pulse in PP pulse discharge. And this problem can be solved by applied to inject the electrons by the negative pulse to neutralize the positive residual charge.

Although this calculation cannot quantitatively explain the results of Figure 4-8, it offers a physical interpretation of the phenomena observed in the experiments.

Finally, suppose the neutralization of residual charges indeed causes the phenomenon. In that case, the experimental results shown in Figure 4-11 tell us that the effect of negative pulses on subsequent positive pulses is a step-like distribution with pulse interval increases. The first part is from 0 to 700 ns. The effect of negative pulses on subsequent positive pulses varies significantly. The second part is from 700 ns to 300 μs. The negative pulse gives the following

positive pulse a similar effect but the peak current of the second positive pulse is lower than that of the first part. Finally, after 300 μs, the peak currents of the first positive and second positive pulses pulse are almost the same. It means that the negative pulse effect on the subsequence positive pulse is over.

The step-like distribution phenomenon is not hard to understand. It indicated that the effect of the negative pulse on the subsequent positive pulse is not only caused by electrons but also by some negative particles.

Based on the pulse discharge process, a large number of electrons are created by negative pulse discharge. And the electrons may run away from the discharge space in a short time. However, some electrons collide with oxygen atoms in the air to form negative ions. Thus, the negative charge of the discharge space can be maintained in the discharge space for a long time. After 300 μs, the positive and negative ions disappeared through recombination and diffusion, resulting in the same currents by the first positive and the second positive pulse.

The phenomenon presented in the Figure 4-11 has indirectly provided experimental evidence for the existence of the positive residual charge in the positive pulse discharge and the negative residual charge in the negative pulse discharge.

4.6 Conclusion

In this chapter, we have studied pulsed gas discharge using a bipolar SSLTD scheme pulsed power generator and a coaxial discharge load. Our goal is to investigate the effect of residual charge on the discharge current amplitude, with a particular focus on the neutralizing effect of the residual charge.

Our experimental results have shown that residual charges left by the previous pulse often affect the subsequent pulse. For instance, the residual charges produced by a positive pulse can

cause a decrease in the current of the following positive pulse. Conversely, the residual charges created by a negative pulse can cause an increase in the current of the next positive pulse. Therefore, in a positive-positive pulse discharge, applying a negative pulse between the first and the second pulse can increase the current of the second positive pulse.

To provide a physical interpretation of this phenomenon, we investigated the influence of residual charges left by the previous pulse discharge. Positive pulse discharge leaves positive residual charges in the discharge space, while negative pulse discharge leaves negative residual charges. When positive and negative residual charges coexist in the discharge space, the charge effect of positive ions can be neutralized by electrons. Based on our findings, we built a 1-D field model to solve the electric field strength distribution. The calculation results indicate that positive residual charge causes a significant drop in the positive electric field strength, while negative residual charge causes a significant rise in the positive electric field strength. Furthermore, residual charges affecting the electric field strength can be reduced by injecting oppositely charged particles.

Thus, in principle, to minimize the influence of residual charge on the discharge electric field strength, we can neutralize the residual charge by injecting oppositely charged particles before pulse discharge. Our study has indirectly provided experimental evidence for the existence of positive residual charge in positive pulse discharge and negative residual charge in negative pulse discharge. Additionally, the study shows that residual charges can be neutralized by oppositely charged particles.

CHAPTER V: CONCLUSION AND FUTURE WORK

5.1 Conclusion

- Feedback control has been implemented in an SSLTD-type pulsed power generator.
- The impedance of an atmospheric pressure gas discharge tube has been controlled using SSLTD so that it remains nearly constant for about 100 ns.
- The residual charge effect generated by positive pulsed discharge has been resolved by the bipolar SSLTD pulsed power supply.
- The electrons generated by negative pulses exist in the discharge space for about a few hundred nanoseconds.
- Negative ions formed by the interaction of electrons generated by negative pulses with atoms in the air exist in the discharge space for about a few hundred microseconds.

5.2 Future Work

- Using SSLTD to research the problem of large-area uniform discharge in pulsed atmospheric pressure gas discharge.

ACHIEVEMENT

■ Publication

● Journal Papers

- **Junxiang Yang**, Longyu Zhuang, Yu Feng, Taichi Sugai, Weihua Jiang; Feedback control of pulsed-power generator based on solid-state linear transformer driver. *Rev Sci Instrum* 1 August 2021; 92 (8): 084704. https://doi.org/10.1063/5.0054555
- **Junxiang Yang**, Taichi Sugai, Akira Tokuchi and Weihua Jiang, "Pulsed Gas Discharge Driven by Bipolar Solid-State Linear Transformer Driver," in IEEE Transactions on Plasma Science, doi: 10.1109/TPS.2023.3272573.
- Longyu Zhuang, **Junxiang Yang**, Taichi Sugai, Akira Tokuchi and Weihua Jiang, "Solid-State Pulsed Power Generator Based on Blumlein PFN Using Saturable Pulse Transformer," in IEEE Transactions on Plasma Science, vol. 49, no. 10, pp. 3189-3192, Oct. 2021, doi: 10.1109/TPS.2021.3108562.
- Longyu Zhuang, **Junxiang Yang**, Taichi Sugai, Weihua Jiang, "Compact all-solid-state high frequency LC-Marx generator based on magnetic switch". High Power Laser and Particle Beams, 2021, 33: 065003. doi: 10.11884/HPLPB202133.210114

● Conference Paper

- **Junxiang Yang**, Taichi Sugai ,Weihua.Jiang, Feedback control of Pulsed-Power Generator Based on Solid-State LTD [C], 11th Asia-Pacific International Symposium on the Basics and Applications of Plasma Technology , Kanazawa, Japan, 2019.
- **Junxiang Yang**, Taichi Sugai,Weihua.Jiang, Smart Response Pulsed-Power Generator Based on Solid-State LTD [C], 47th IEEE International Conference on Plasma Science (ICOPS-2020) and 2nd ASIA Pacific Conference on Plasma and Terahertz Science

(APCOPTS-2020), Singapore, 2020.

- **Junxiang Yang**, Taichi Sugai, Akira Tokuchi, Weihua Jiang, Pulsed Gas Discharge Driven by Solid-State LTD [C], the 8th Euro-Asian Pulsed Power Conference (EAPPC 2020), Biarritz, France, 2021.
- **Junxiang Yang**, Taichi Sugai, Akira Tokuchi, Weihua Jiang, Pulsed Gas Discharge Studied by Bipolar Solid-State LTD [C], the 9th Euro-Asian Pulsed Power Conference (EAPPC 2020), Seoul, Korea, 2022.
- **Junxiang Yang**, Taichi Sugai, Weihua Jiang, Pulsed Gas Discharge Driven by Bipolar Solid-State LTD [C], 電気学会 放電・プラズマ・パルスパワ, 長岡, 日本, 2022.

Scholarship

- **JGC-S Scholarship Foundation**

Competition Award

- **The Third Prize of the "Huawei Cup" - the 17th China Postgraduate Mathematical Contest in Modeling, 2021.**

REFERENCE

[1] Bluhm, Hansjoachim. Power systems. Berlin: Springer, 2006.

[2] Zaiter, Joshua John. "An Overview of Pulsed Power System Design and Applications." (2021)..

[3] Marx, Erwin (1924). "Versuche über die Prüfung von Isolatoren mit Spanningsstößen" [Experiments on the Testing of Insulators using High Voltage Pulses]. Elektrotechnische Zeitschrift (in German). 25: 652–654. ISSN 0424-0200. OCLC 5797229.

[4] Liu Xisan. “High power pulse technology”.BeiJing：National Defense Industry Press，2007.

[5] Wang Yin, SunYuanzhang. “Pulsed power science and technology”.BeiJing ： Beihang University Press，2010.

[6] Yu Liang. " Research on Pulsed Power Generation Based on Inductive Energy Storage (IES)." Doctoral dissertation, NAGAOKA UNIVERSITY OF TECHNOLOGY, 2017.

[7] Schoenbach, Karl H., et al. "Bioelectrics-new applications for pulsed power technology." IEEE Transactions on Plasma science 30.1 (2002): 293-300.

[8] Akiyama, Hidenori, et al. "Environmental applications of repetitive pulsed power." IEEE Transactions on Dielectrics and Electrical Insulation 14.4 (2007): 825-833.

[9] Sugai, Taichi, Akira Tokuchi, and Weihua Jiang. "Effects of pulsed power control on plasma water treatment using LTD." IEEE Transactions on Plasma Science 46.10 (2018): 3566-3573.

[10] M. P. J. Gaudreau, J. Casey, T. Hawkey, J. M. Mulvaney and M. A. Kempkes, "Solid-state pulsed power systems," Conference Record of the Twenty-Third International Power Modulator Symposium (Cat. No. 98CH36133), Rancho Mirage, CA, USA, 1998, pp. 160-163, doi: 10.1109/MODSYM.1998.741216.

[11] Mesyats, Gennady A. Pulsed power. Springer Science & Business Media, 2007.

[12] Tokuchi, Akira, et al. "Repetitive pulsed-power generator" ETIGO-IV"." IEEE transactions on plasma science 30.5 (2002): 1637-1641.

[12] T. Sakugawa et al., "High repetition rate pulsed power generator using IGBTs and magnetic pulse compression circuit," 2009 IEEE Pulsed Power Conference, Washington, DC, USA, 2009, pp. 394-398, doi: 10.1109/PPC.2009.5386283.

[13] Kakizaki, Kouji, et al. "Ultrahigh-repetition-rate ArF excimer laser with long pulse duration for 193-nm lithography." Optical Microlithography XIV. Vol. 4346. SPIE, 2001.

[14] A. I. Bushlyakov et al., "Solid-State SOS-Based Generator Providing a Peak Power of 4 GW," in IEEE Transactions on Plasma Science, vol. 34, no. 5, pp. 1873-1878, Oct. 2006, doi: 10.1109/TPS.2006.881300.

[15] Jiang, Weihua, et al. "Development of repetitive pulsed power generators using power

semiconductor devices." 2005 IEEE Pulsed Power Conference. IEEE, 2005.

[16] Continetti, R. E., D. R. Cyr, and D. M. Neumark. "Fast 8 kV metal–oxide semiconductor field‐effect transistor switch." Review of scientific instruments 63.2 (1992): 1840-1841.

[17] L. M. Redondo, H. Canacsinh and J. F. Silva, "Generalized solid-state marx modulator topology," in IEEE Transactions on Dielectrics and Electrical Insulation, vol. 16, no. 4, pp. 1037-1042, August 2009, doi: 10.1109/TDEI.2009.5211851.

[18] W. Jiang, "Solid-State LTD Module Using Power MOSFETs," in IEEE Transactions on Plasma Science, vol. 38, no. 10, pp. 2730-2733, Oct. 2010, doi: 10.1109/TPS.2010.2051042.

[19] Liu H, Yao C, Zhao Y, Chen X, Dong S, Wang L, Davalos RV. In Vitro Experimental and Numerical Studies on the Preferential Ablation of Chemo-Resistant Tumor Cells Induced by High-Voltage Nanosecond Pulsed Electric Fields. IEEE Trans Biomed Eng. 2021 Aug;68(8):2400-2411. doi: 10.1109/TBME.2020.3040337. Epub 2021 Jul 16. PMID: 33232222.

[20] N. Shimomura et al., "Nanosecond pulsed power application to nitrogen oxides treatment with coaxial reactors," in IEEE Transactions on Dielectrics and Electrical Insulation, vol. 18, no. 4, pp. 1274-1280, August 2011, doi: 10.1109/TDEI.2011.5976127.

[21] S. R. Jang, H. J. Ryoo, Y. S. Jin, S. H. Ahn and G. H. Rim, "Application of pulsed power system for water treatment of the leachate," 2009 IEEE Pulsed Power Conference, Washington, DC, USA, 2009, pp. 980-983, doi: 10.1109/PPC.2009.5386150.

[22] Jiang, Weihua. "Review of solid-state linear transformer driver technology." Matter and Radiation at Extremes 3.4 (2018): 159-164.

[23] Wang, Douyan, and Takao Namihira. "Nanosecond pulsed streamer discharges: II. Physics, discharge characterization and plasma processing." Plasma Sources Science and Technology 29.2 (2020): 023001.

[24] Thomas, Ken J., et al. "Prototype IVA module." IEEE transactions on plasma science 30.5 (2002): 1642-1646.

[25] Ramirez, J. J., et al. The Hermes-III Program. No. SAND-87-0082C; CONF-870656-37. Sandia National Labs., Albuquerque, NM (USA), 1987.

[26] Kim, A. A., et al. "Development and tests of fast 1-MA linear transformer driver stages." Physical Review Special Topics-Accelerators and Beams 12.5 (2009): 050402.

[27] Jiang, Weihua, and Akira Tokuchi. "Repetitive linear transformer driver using power MOSFETs." IEEE Transactions on Plasma Science 40.10 (2012): 2625-2628.

[28] Feng, Yu, Taichi Sugai, and Weihua Jiang. "Solid-state bipolar linear transformer driver using inductive energy storage." IEEE Transactions on Plasma Science 49.9 (2021): 2887-2892.

[29] Jiang, Weihua, and Akira Tokuchi. "Repetitive linear transformer driver using power MOSFETs." IEEE Transactions on Plasma Science 40.10 (2012): 2625-2628.

[30] S. Jin, J. Chen, Z. Li, C. Zhang, Y. Zhao and Z. Fang, "Novel RDD Pulse Shaping Method for High-Power High-Voltage Pulse Current Power Supply in DBD Application," in IEEE Transactions on Industrial Electronics, vol. 69, no. 12, pp. 12653-12664, Dec. 2022, doi: 10.1109/TIE.2022.3140515.

[31] L. Collier, T. Kajiwara, J. Dickens, J. Mankowski and A. Neuber, "Fast SiC Switching Limits for Pulsed Power Applications," in IEEE Transactions on Plasma Science, vol. 47, no. 12, pp. 5306-5313, Dec. 2019, doi: 10.1109/TPS.2019.2928535.

[32] Fan, Zhe, et al. "One-step high-value conversion of heavy oil into H2, C2H2 and carbon nanomaterials by non-thermal plasma." Chemical Engineering Journal 461 (2023): 141860.

[33] X. Liu, C. Ye, X. Wang, S. Zhang, M. Zhu and A. Jiang, "Plasma Impedance Characteristics of Radio Frequency and Very High-Frequency Magnetron Discharges," in IEEE Transactions on Plasma Science, vol. 48, no. 1, pp. 99-103, Jan. 2020, doi: 10.1109/TPS.2019.2958317.

[34] Kazemi, M. Reza, et al. "Waveform control of pulsed-power generator based on solid-state LTD." IEEE Transactions on Plasma Science 45.2 (2016): 247-251.

[35]Liu, Si-Wei, et al. "Influence of plasma channel impedance model on electrohydraulic shockwave simulation." Physics of plasmas 26.2 (2019): 023522.

[36]Singh, Dheeraj K., et al. "Analysis of the discharge plasma impedance of copper vapor laser." Laser Physics 32.5 (2022): 055002.

[37]Wang, Douyan, Takao Namihira, and Hidenori Akiyama. "Pulsed discharge plasma for pollution control." Air Pollution. London, UK: InTech, 2010. 265-287.

[38] Liao, Yangfan, and Xing Jin. "The analysis of influence factors of impedance in inductively coupled plasma." 2017 IEEE 3rd Information Technology and Mechatronics Engineering Conference (ITOEC). IEEE, 2017.

[39] ADC-SOC FPGA manual.

[40] Rui, F. A. N., et al. "The regulation of memory effect and its influence on discharge properties of a dielectric barrier discharge driven by bipolar pulse at atmospheric-pressure nitrogen." Plasma Science and Technology 23.10 (2021): 105401.

[41] Van Brunt, Richard J. "Physics and chemistry of partial discharge and corona. Recent advances and future challenges." IEEE Transactions on dielectrics and Electrical Insulation 1.5 (1994): 761-784.

[42] Zhao, Zheng, and Jiangtao Li. "Repetitively pulsed gas discharges: memory effect and discharge mode transition." High Voltage 5.5 (2020): 569-582.

[43] Pai, David Z., Deanna A. Lacoste, and Christophe O. Laux. "Nanosecond repetitively pulsed discharges in air at atmospheric pressure—the spark regime." Plasma Sources Science and Technology 19.6 (2010): 065015.

[44] Pai, David Z., Deanna A. Lacoste, and Christophe O. Laux. "Transitions between corona, glow,

and spark regimes of nanosecond repetitively pulsed discharges in air at atmospheric pressure." Journal of Applied Physics 107.9 (2010): 093303.

[45] Xu, Da A., et al. "Experimental study of the hydrodynamic expansion following a nanosecond repetitively pulsed discharge in air." Applied Physics Letters 99.12 (2011): 121502.

[46] Rusterholtz, D. L., et al. "Ultrafast heating and oxygen dissociation in atmospheric pressure air by nanosecond repetitively pulsed discharges." Journal of Physics D: Applied Physics 46.46 (2013): 464010.

[47] M. R. Kazemi, T. Sugai, A. Tokuchi and W. Jiang, "Study of Pulsed Atmospheric Discharge Using Solid-State LTD," in IEEE Transactions on Plasma Science, vol. 45, no. 8, pp. 2323-2327, Aug. 2017, doi: 10.1109/TPS.2017.2707105.

[48] Stollenwerk, L., Sh Amiranashvili, and H. G. Purwins. "Forced random walks with memory in a glow mode dielectric barrier discharge." New Journal of Physics 8.9 (2006): 217.

[49] Gomer, Robert, and R. Gomer. Field emission and field ionization. Vol. 34. Cambridge: Harvard University Press, 1961.

[50] Kozhevnikov, V. Yu, Andrey V. Kozyrev, and Natalia S. Semeniuk. "1D simulation of runaway electrons generation in pulsed high-pressure gas discharge." Europhysics Letters 112.1 (2015): 15001.

ACKNOWLEDGMENT

First and foremost, the author would like to express gratitude to his father, Yang Wenfeng, and his mother, Zeng Jiefeng, who dedicated their final energies in life to support the author's pursuit of education. The memory of his mother handing over her hard-earned savings of 30,000 RMB, saying, "Ah, this money was originally meant for you to start a business and get married. Now you need it for your studies, so I'm giving it to you. It will take a long, long time to save up that much money again," brings tears to the author's eyes. The author also deeply resonates with his father's words, "Our family hasn't produced a talent in a long time. Your parents are already old and can only help you until this point. You have to walk the rest of the road on your own, as far as you can go."

Now, the author lives up to their parents' expectations. As a returning son, the author yearns to show filial piety, yet the author’s parents are no longer here to witness the author’s success. However, the unwavering support from his parents will remain as invisible wings, guiding the author as they overcome obstacles and forge ahead on their journey towards the future.

Since arriving at Nagaoka University of Technology, Japan in 2018, the author had the privilege of joining the Extreme Energy-Density Research Institute and the Pulsed Power Laboratory. The achievements presented in this thesis are inseparable from the invaluable contributions of the professors and fellow students.

This thesis was completed under the patient and dedicated guidance of Professor Jiang Weihua. Professor Jiang's profound knowledge, noble character, rigorous work ethic, and relentless pursuit of scientific research have left a deep impression on the author. In Professor Jiang's laboratory, the relaxed and comfortable research environment allowed the author to maximize their own potential. Looking back, the decision to join Professor Jiang's laboratory

five years ago was the most important and successful decision the author has made. There is a Chinese saying that goes: "One day as a teacher, lifelong as a father." Although the author only had a short five years of study in Professor Jiang's laboratory, his manner of conducting himself has already had a profound impact on the author's life.

Additionally, the completion of this thesis would not have been possible without the support of Assistant Professor Taichi Sugai. Assistant Professor Taichi Sugai, with his kind-hearted nature, has provided invaluable guidance and advice in the author's research work.

Special thanks to Professors Yushi Miura, Takashi Kikuchi, and Toru Sasaki from Nagaoka University of Technology, as well as Professor Nobuaki Oshima from Sanyo-Onoda City University, for their valuable insights during the author's doctoral defense. In particular, heartfelt appreciation goes to Professor Kikuchi and Professor Sasaki for their involvement in every defense the author has had since the master's level, providing essential advice.

Furthermore, gratitude is extended to Assistant Watanabe from the Extreme Energy-Density Research Institute for assisting in the procurement of experimental equipment, which greatly facilitated the smooth progress of the related experimental research.

Special thanks are given to the Academic Affairs Department and the International Office of the Nagaoka University of Technology for their unwavering administrative support.

The author would like to express appreciation to Professor Shao Tao from the Institute of Electrical Engineering, Chinese Academy of Sciences. Although the author had the opportunity to meet Professor Shao only once, studying Professor Shao's research work on industrial applications of pulsed power technology was enlightening and highly beneficial.

Gratitude is also extended to Li Xiaohua from the University of South China. The author holds a deep memory of the phrase "Never let honest people suffer" spoken by Li, and the author

will continue to adhere to this principle on their life's path.

The author would like to express gratitude to Qin Qianqian and thank her for her presence, support, and companionship.

The author wishes to thank Dr. Ren Xiaojing, Dr. Zhuang Longyu, and Wen Juan. Thank you for the support and companionship provided when the author needed it most.

The author expresses gratitude to the Nagaoka City Government in Japan for providing affordable housing, which was instrumental in supporting the completion of their studies.

The author is grateful for the JGC-S Scholarship, which provided financial support to continue the author’s education.

At this moment, the author extends heartfelt thanks to all the teachers, classmates, and friends who have supported and helped them.

There is an ancient Chinese saying, "There are often exceptional horses in a thousand miles race, but not always exceptional judges." The author would like to thank their exceptional judge, Ms. Sun Qiqin. The author appreciates Ms. Sun's recognition of their work and acknowledges her tireless efforts for their education. The cooperation and support provided by Ms. Sun have been crucial to the author's completion of their studies. At the same time, Ms. Sun has guided the author's path at critical junctures in life, leaving an unforgettable impact.

Finally, I want to express my gratitude to Dr. Yijin, who, despite our unexpected encounter, shares a deep connection with me and stands by my side through thick and thin. From Western Europe to East Asia, from Switzerland to Japan, spanning across the Eurasian continent, we are separated by seven time zones. We express our admiration and unwavering support for each other in the purest of ways. It pains me deeply that despite the vast distance that separates us, I cannot be there by your side when you need me the most. I can only hope to make up for the love that

is lacking by doubling it in the future. In this lifetime, I vow to be like lovebirds, never failing to cherish you. Together, let us compose a radiant chapter in the history of our nation, leaving our mark amidst the five thousand years of Chinese civilization. Even when we both turn grey and old, we will still look at each other with infinite fondness. As for our story, let it be sung and passed down by future generations. Lastly, Dr. Yijin, would you be willing to don a pristine white wedding gown for me and say those magical words, "YES I do," in the grand halls of our wedding ceremony?